SOLUTION PROCESSING OF SILVER-BASED KESTERITE: FROM NANOPARTICLES TO THIN FILM SOLAR CELLS

by

Xianyi Hu

A Dissertation

Submitted to the Faculty of Purdue University

In Partial Fulfillment of the Requirements for the degree of

Doctor of Philosophy

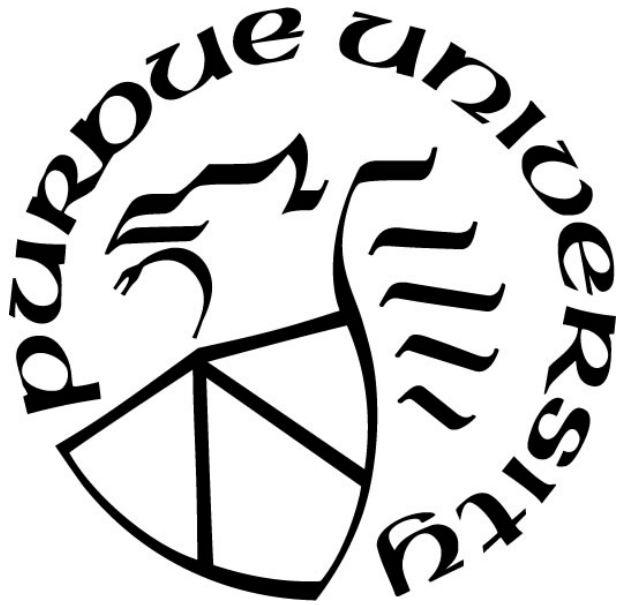

School of Materials Engineering

West Lafayette, Indiana

August 2019

THE PURDUE UNIVERSITY GRADUATE SCHOOL
STATEMENT OF COMMITTEE APPROVAL

Dr. Carol A Handwerker, Co-chair
School of Materials Engineering
Dr. Rakesh Agrawal, Co-chair
Davidson School of Chemical Engineering
Dr. Eric Kvam
School of Materials Engineering
Dr. John Blendell
School of Materials Engineering

Approved by:

Dr. David Bahr
Head of the Graduate Program

For my families

ACKNOWLEDGMENTS

First of all, I would like to thank both of my advisors: Dr. Carol Handwerker and Dr. Rakesh Agrawal. Dr. Carol Handwerker is not only my advisor for my professional career, but also such a role model for my future life. I am so impressed by her enthusiasm in encouraging women's participation in science and engineering, her concern for the sustainability issues in developing countries and her appreciation for each small achievement accomplished by everyone in the group. For Dr. Agrawal, I learnt so much from his hardworking, generosity and humble attitude towards every single piece of new knowledge, which shaped my view of value and life after working with him for almost 5 years. I will never forget his sincere suggestion when I was facing the choices, his open mind when I started my research on different subjects and his understanding and caring for me as an international student. I am so grateful and couldn't imagine I would find a better combination of advisors. I would like to thank Dr. John Blendell and Dr. Eric Kvam as my committee members. They are so generous to share their advice on graduate research, presentation skills and time management throughout my whole PhD. Besides, I appreciate Ms. Vicki Cline, Ms. Rosemary Son and Ms. Stacey Coar for their assistance in all the miscellaneous things within the department.

I appreciate the help and suggestions I received throughout my 5 years at Purdue. I am thankful to the solar group members: Dr. David Wei-Chang Yang, Dr. Ruihong Zhang, Dr. Brian Graeser, Dr. Caleb Miskin, Dr. Xin Zhao, Dr. Mark Koeper, Robert Boyne, Scott McClary, Swapnil Deshmukh, Joseph Andler, Essam AlRuqobah, Ryan Ellis, David Rokke, Kyle Weideman, Susannah Pritchett-Montavon, Preston Fernandez, Anna Murray, Jonathan Turnley and Apurva Pradhan, as well as the Blend-werker group members: Dr. Thomas Reeves, Dr. John Holaday, Dr. David Lowing,

Matthew Michie, Xi Chen, Keisuke Yazawa, Congying Wang, Yaohui Fan, Ruwen Zheng and Alyssa Yaeger. I also received tremendous help from Prof. Wolfgang Rheinheimer, Dr. Christopher Gilpin, Dr. Rosa Diaz and Ms. Laurie Mueller for their useful discussions. I also appreciate the collaboration with Brookhaven National Laboratory and opportunity to work with and get help from Dr. Eric Stach, Dr. Dong Su, Dr. Sooyeon Hwang, Dr. Huolin Xin and Kim Kisslinger.

I want to express my sincere appreciation to my friends I met at Purdue for the sorrow and joy, for the pressure and love we have shared together. I want to thank my parents from the deepest of my heart. I spent only a few tens of days with them as the only child of the family since I came to Purdue, however they never complained a single word but always comfort me with endless love and support. At last, I would like to thank my husband, Dr. Xiaochen Ren. Without his unconditional trust, patience and encouragement, I would not have been focused on my research confidently for this five-year-long journey.

TABLE OF CONTENTS

LIST OF TABLES

LIST OF FIGURES

ABSTRACT

Author: Hu, Xianyi. PhD
Institution: Purdue University
Degree Received: August 2019
Title: Solution Processing of Silver-based Kesterite: from Nanoparticles to Thin Film Solar Cells
Committee Chair: Carol Handwerker and Rakesh Agrawal

Because of the limited reserve of fossil fuels and issues brought up by their combustion, the demand on renewable energy is considerably increasing. Solar energy is one of the most promising renewable energy sources considering the large amount of solar irradiation received by Earth and solar cell is such a device that allows us to directly convert sunlight directly into electricity. In this thesis, kesterite (I_2-II-IV-IV_4) system is the main focus as the light absorber material in thin film solar cells.

$Cu_2ZnSn(S,Se)_4$ (CZTSSe) has been first studied intensively. However, due to the band tailing resulting from Cu-Zn anti-site defects, further improvement on power conversion efficiency of this material has been hindered. Substituting Cu with Ag is expected to solve this problem by decreasing this defect density as a result of the high formation energy of Ag-Zn antisite defects. Herein, different concentrations of Ag are used to substitute Cu in the kesterite system through a nanoparticle-ink route for the fabrication of light absorber thin films. For Ag-alloying concentration less than 50%, it suggests that the Ag can induce inhomogeneity as well as secondary phase formation during nanoparticle formation. Moreover, Ag alloying is shown to enlarge the grain size and reduce film roughness after selenization, which are beneficial for the optoelectronic properties and device performance.

Additionally, the synthesis process for kesterite Ag_2ZnSnS_4 nanoparticles is explored. AZTS nanoparticles are achieved by solvent-thermal reaction. The reaction pathway during reaction is investigated by different material characterization methods to shed light on the Ag-based nanoparticle synthesis. The final nanoparticles obtained have high crystallinity and homogeneous composition, demonstrating great potential as light absorber materials. Also, the sulfide nanoparticles are converted into selenide thin films in Se vapor at elevated temperature (selenization). The selenization conditions, including temperature, heating ramp and selenization time, are optimized for the pure phase kesterite AZTSe thin films with large and dense grains. The optoelectronic properties are explored on these films and an initial research already demonstrates a 0.35% power conversion efficiency as the first solution processed AZTSe device.

In summary, multiple material characterization techniques are utilized to understand the microstructure evolution, phase transformation, and composition change for solution-processed nanoparticles and their resulting thin films. The material characteristics, process methods and film optoelectronic properties are associated for the future analysis and development of kesterite thin films for photovoltaic applications.

1. INTRODUCTION

1.1 Demand for development of solar energy

The world energy consumption is considered to increase about 25% by 2040, based on a report in 2018 [1], mostly because of the increased industry and building consumption, as well as the huge potential of demand for improvement in living standards in developing countries. Up to then (2018), fossil fuels (oil, gas and coal) still accounted for more than 80% of energy generation. The combustion of these fossil fuels produces different species of flue gases, including sulfur oxides, nitrogen oxides as air pollutants and a large amount of carbon dioxide (CO_2), which significantly contributes to global warming as a greenhouse gas. For the sake of reducing carbon emissions, the organization for economic co-operation and development (OECD) requests closure of all the coal-fired power stations by the year of 2030. In order to fill the energy gap of such magnitude, as well as meet the increased energy need, how to produce sufficient clean energy is one of the most urgent problems in front of human society.

By 2017, about 15% of the total power supply in the world was generated by non-combusted energy plant, such as nuclear, hydro, solar, wind and geothermal. Among all of them, hydroelectric powers contributed for about half of the clean electricity as shown in Figure 1.1. However, limited reservoir, huge fiscal cost and the uncertain environmental impacts are all concerns for construction of new hydroelectric power plants. For example, the Three Gorges Dam on the Yangtze River, as the largest hydroelectric dam on the planet, has been questioned seriously regarding climate change and drought in the downstream area. Nuclear power is another option, with great potential and relatively low costs as well as high energy output. While after the nuclear plant accidents happened in Chernobyl and Fukushima, theses catastrophes not only left inerasable

radiation pollution in local places, but also gave rise to the public concern or even panic on the risk of failure of nuclear power plants. Numbers of anti-nuclear protests happened all around the world, especially after Fukushima disaster.

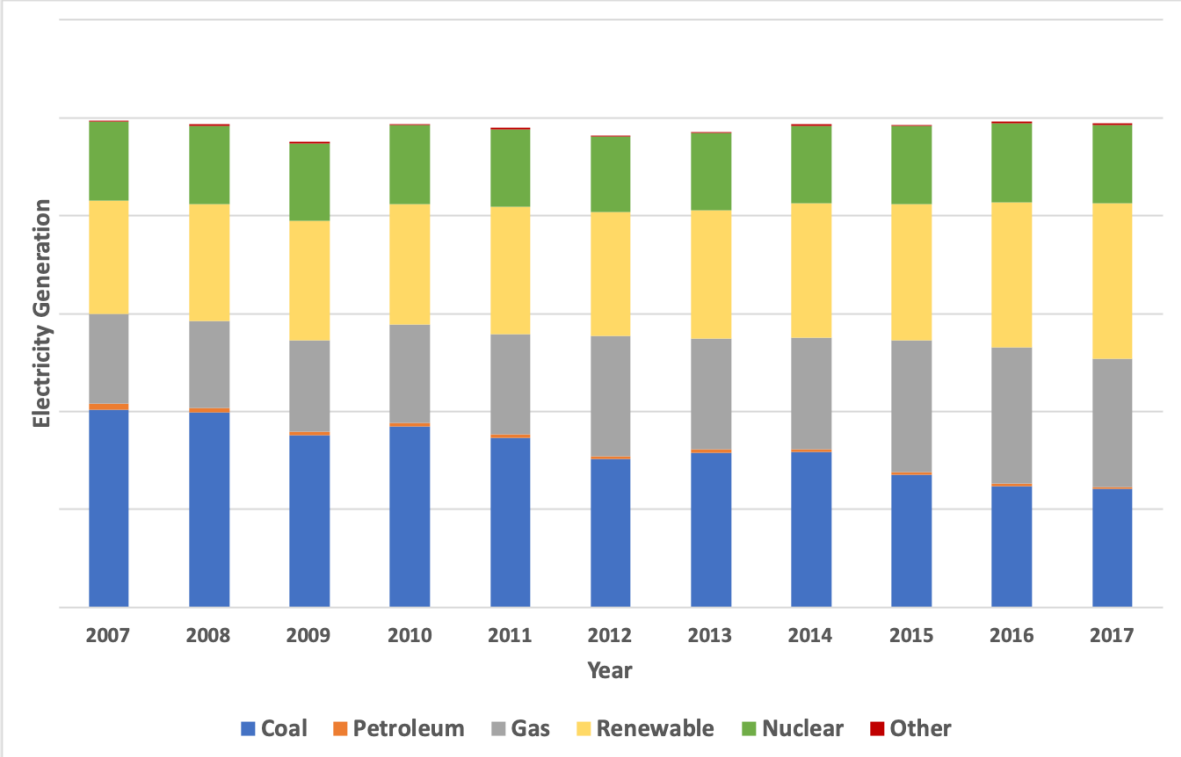

Figure 1.1 Electricity net generation by energy source in U.S. Petroleum includes petroleum liquids and petroleum coke; gas includes natural gas, blast furnace gas and other manufactured as well as waste gases derived from fossil fuels; renewable sources include hydroelectric, wind, solar, biomass and geothermal. Figure is drawn based on the data from EIA electric power annual report (2017) [2].

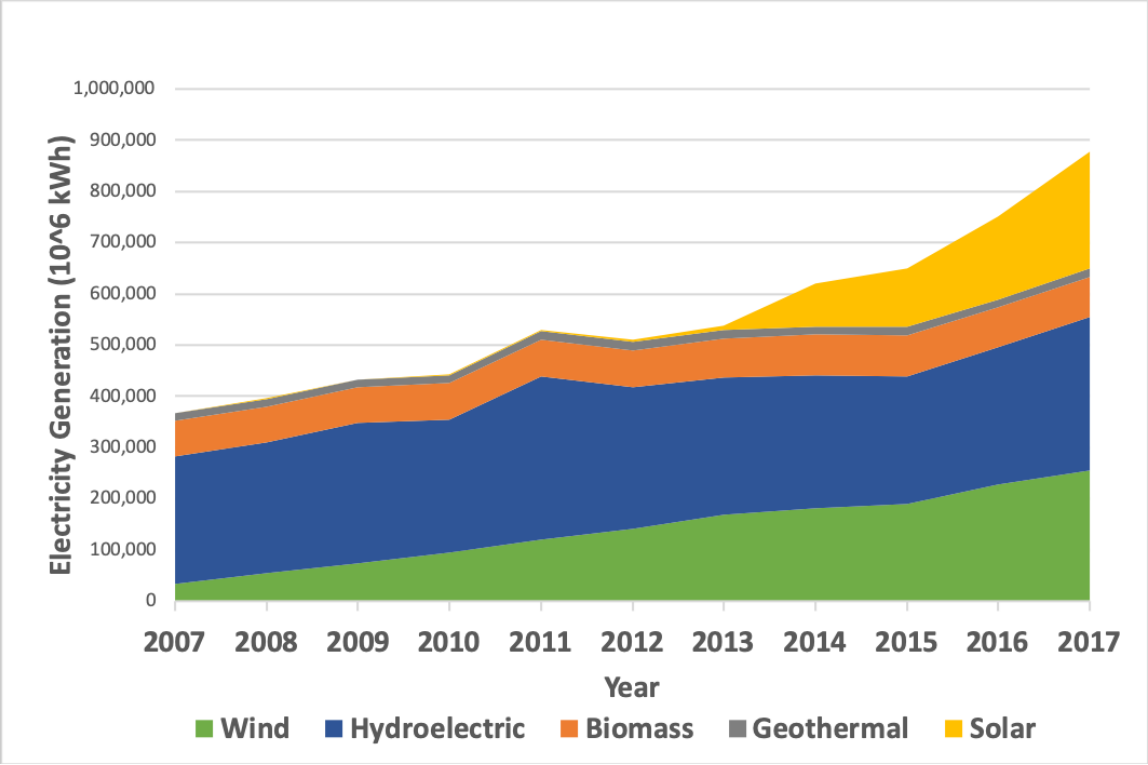

Figure 1.2 Electricity net generation from renewable sources in recent 10 years. Figure is drawn based on the data from EIA electric power annual report (2017) [2].

Comprehensively considering the cost, availability and safety, solar energy can be one of the solutions and shares an increaseing portion among all the renewable energy sources in recent years (as shown in Figure 1.2). Generally, there are two ways to utilize the solar energy: solar thermal or photovoltaics. Solar thermal directly uses the heat from the sun for water heating, house ventilation or cooking. For example, solar water heating is extensively used in China, supplying about 10% of Chinese household water usage. In this thesis, we are focusing on another way to use solar: converting solar energy into electricity, or photovoltaics. Theoretically, the energy density received from sun is more than 1000 W/m^2 on the earth. Even after the absorption and scattering of clouds, the average energy flux received by the surface of the earth is as high as 170 W/m^2. Based on the survey data from EIA (U.S. Energy Information Administration), the average

annual electricity consumption in a U.S. house is about 10,000 kWh. That means a 60 m^2 solar panel can meet a U.S families daily electricity need, with only 10% total solar-to-electricity conversion efficiency. For 2018, as shown in Figure 1.3, the total residential energy consumption was 2511 trillion Btu in the U.S., while only 224 trillion Btu of it came from solar [3], demonstrating a great potential for the development of family-scale solar panels, let alone the utility-scale electricity generated from solar farm for commercial or industrial usage.

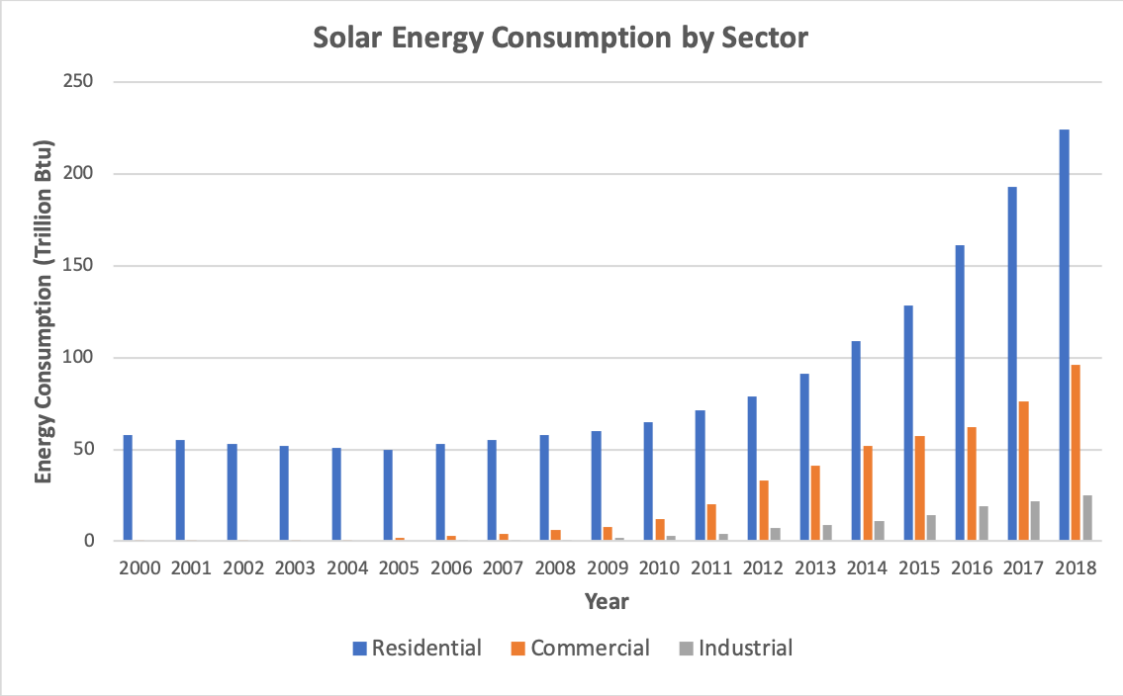

Figure 1.3 Solar energy consumption by sector based on EIA Monthly Energy Review May 2019 [4].

1.2 Photovoltaic device physics

The conversion of solar energy into electricity relies on photovoltaic devices, or solar cells. After photons are absorbed by a photovoltaic device, the energy from photons excites the electrons to higher energy states and these electrons can be collected out of these materials and generate current flow due to a built-in potential inside the devices.

1.2.1 Photovoltaic materials

As the core of solar cells, photovoltaic materials are where the current generation happens, which means one of the most important criteria for photovoltaic materials is that sunlight is able to excite electrons to a higher energy state in these materials. As a result, band gap of about 1.1-1.4 eV is required, since it makes the best utilization of visible light. Also, a high absorption coefficient ($\sim 10^5$ cm^{-1}) is preferred to absorb light within a minimum thickness.

The band gap of the absorber materials defines them as semiconductors. Either intrinsic or extrinsic semiconductors can be used as light absorber materials. One of the most common photovoltaic materials, silicon, is an extrinsic semiconductor. The free electrons or holes in silicon are coming from dopants. For example, doping silicon with group V atoms creates available electrons, therefore makes it n-type, while doping with group III atoms creates holes and makes it p-type. Intrinsic semiconductors are like undoped cadmium sulfide (CdS), gallium arsenide (GaAs) or copper indium gallium selenide (CIGSe). The semiconducting properties are not induced by foreign atoms, but by the intrinsic defects. For example, Cu vacancies in CIGSe generate holes and make it a p-type semiconductor. Enough free electrons or holes (so called charge carriers) are essential for photovoltaic materials to produce a significant amount of current. However, the doping density cannot be too high to maintain the electron field potential in the devices.

Other than band gap width, absorption coefficient and carrier density, it is also important to have preferred defects for good absorber materials. For example, p-type semiconductors should avoid defect states close to conduction band and n-type semiconductors should avoid defects creating states close to valence band. Mid-band defect states should be minimized in both cases. These

defect states can act as recombination sites for electrons and holes, and the absorbed solar energy will emit as either heat or light emission instead of electricity.

1.2.2 P-N junction in photovoltaic devices

When a p-type semiconductor and an n-type semiconductor touch each other, a p-n junction is formed. When two materials are in touch, the Fermi level of them has to be at the same level. Since a p-type semiconductor has a Fermi level close to valence band and an n-type semiconductor has a Fermi level close to conduction band, an electric field is created at the interface once they are in contact as shown in Figure 1.4. When photons are absorbed by either material, numbers of electron-hole pairs are generated. Under this electric field, the minority carriers, e.g. electrons in p-type material and holes in n-type material, drift to the other side on the p-n junction. They become the majority carriers once they are in the other side and be able to generate a current flow through the external circuit.

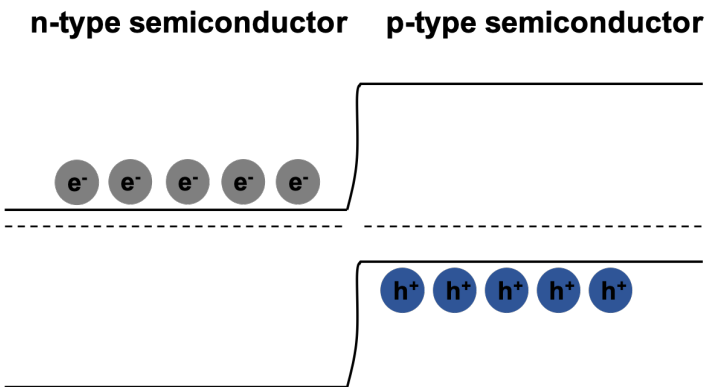

Figure 1.4 Schematic for a p-n junction

1.2.3 Device measurement and analysis

To determine the efficiency of a solar cell, its current response is measured both in dark and under light with swept voltage, i.e. an I-V curve. An I-V curve example is shown in Figure 1.5, and the power conversion efficiency is defined as:

$$\eta = \frac{P_{max}}{P_{in}} \tag{1.1}$$

Typically, solar cells are measured under AM 1.5, corresponding to an incident power density (P_{in}) of 0.1W/cm^2 and the output power density can be obtained from the light I-V curve:

$$P_{max} = \frac{V_{oc}\, I_{sc}\, FF}{A} \tag{1.2}$$

where V_{oc} is open circuit voltage corresponding to the interception between I-V curve and x-axis, I_{sc} is short circuit voltage corresponding to the interception between I-V curve and y-axis, A is the area of the solar cell, and FF is called fill factor. Mathematically, P_{max} is the maximum value of I*V on the light I-V curve; or it also can be seen as the area of the largest rectangle that fits in the I-V curve in the first quadrant.

$$\mathrm{FF} = \frac{V_{mp}\, I_{mp}}{V_{oc}\, I_{sc}} \tag{1.3}$$

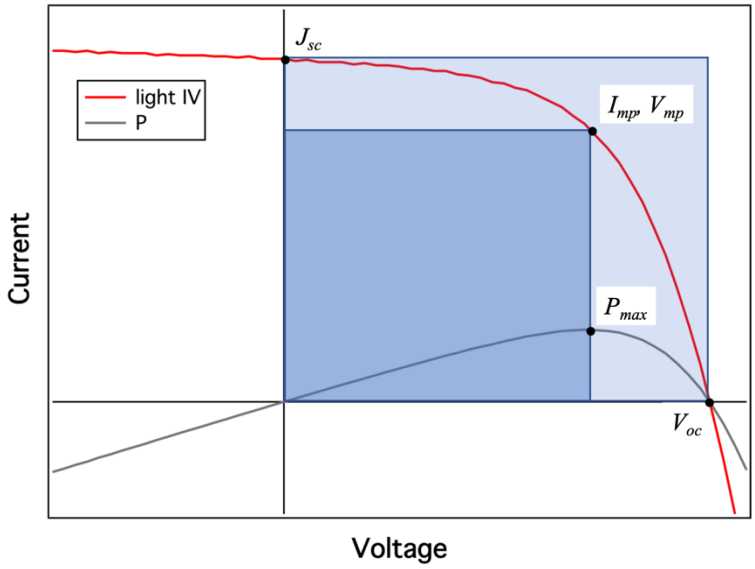

Figure 1.5 Illustration of the fill factor in an I-V curve example

Other than efficiency, V_{oc}, I_{sc}, and fill factor, to better understand the loss mechanism of a solar cell and associate the I-V performance with the electric properties of a photovoltaic device, a single diode circuit diagram in Figure 1.6 can be used to describe the photovoltaic device. In this model, solar cell is equivalent to a parallel connected current generator, a diode, and a shunting resistor as well as a tandem connected resistor.

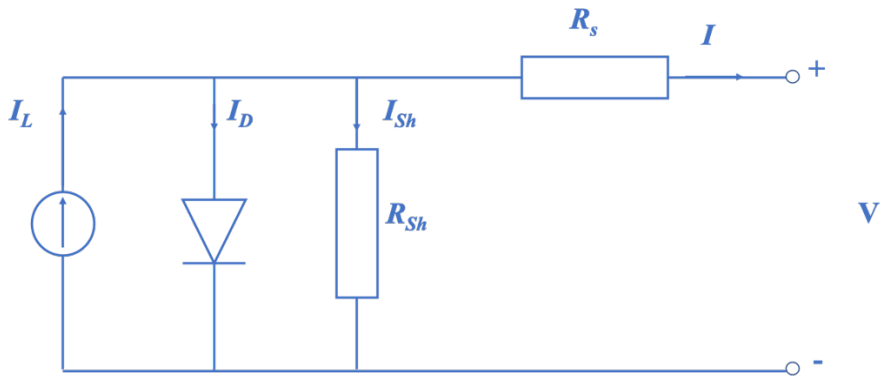

Figure 1.6 Equivalent circuit model for solar cell

The final output current (I) can be expressed as

$$\mathrm{I} = I_L - I_D - I_{Sh} \tag{1.4}$$

in which I_L is the current generated under illumination, I_D is recombination induced current lost at diode, and I_{Sh} is shunting induced current lost. Based on Shockley equation, the diode current is

$$I_D = I_0 \left[exp\left(\frac{q(V + IR_s)}{nkT} \right) - 1 \right] \tag{1.5}$$

where I_0 is the saturated dark current, q is elementary charge, n is the diode ideality factor, k is the Boltzmann constant and T is temperature. The shunt current is:

$$I_{Sh} = \frac{V + IR_S}{R_{Sh}} \tag{1.6}$$

Combining all the equations above, the output current is:

$$\mathrm{I} = I_L - I_0 \left[exp\left(\frac{q(V + IR_s)}{nkT} \right) - 1 \right] - \frac{V + IR_S}{R_{Sh}} \tag{1.7}$$

For series resistance, when shunt resistance is big enough, the relationship with power/ current output can be approximately described as:

$$P'_{MP} \approx V_{MP} I_{MP} - I_{MP}^2 R_s = V_{MP} I_{MP} (1 - \frac{I_{sc}}{V_{oc}} R_s) \tag{1.8}$$

$$I' \approx I_L - I_0 \left[exp\left(\frac{q(V + IR_s)}{nkT} \right) \right] \tag{1.9}$$

With the increase of series resistance, the I-V curve is bent towards the current axis and the fill factor is decreased. Shunt resistance, when series resistance is negligible, similar to the series resistance case, it can be expressed as:

$$P'_{MP} \approx V_{MP} I_{MP} - \frac{V_{MP}^2}{R_{Sh}} = V_{MP} I_{MP} (1 - \frac{I_{sc}}{V_{oc}} \frac{1}{R_{Sh}}) \tag{1.10}$$

When shunt resistance decreases, the I-V curve is bent towards the x-axis and the fill factor is decreased at the same time.

$$I' \approx I_L - I_0 \left[exp\left(\frac{qV}{nkT}\right)\right] - \frac{V}{R_{Sh}} \quad 1.11$$

To maximize output power, R_S should be minimized and R_{Sh} should be maximized, which is related to the design and processing of the solar cell. Series resistance has multiple sources, including:

- Resistance in the absorber. For example, some of the grain boundaries in the direction of current flow may generate resistance in the absorber layer in polycrystalline materials.
- Resistance at the interface(s). For instance, different band alignments between different contact materials and the absorber layer result in different series resistance [5].
- the resistance in the front and back metal contacts, which usually can be reduced by changing the geometry of the contacts.

For low shunt resistance, there are two kinds of origins for shunting paths: process-induced shunting and material-induced shunting [6]. Process-induced shunting is due to defective fabrication, such as edge effects, cracks and holes in the semiconductors *etc.*, while material-induced shunting is about the material itself. For example, the semiconductor may have different defect states that allows significant Shockley-Read-Hall recombination inside the material, or grain boundaries that are highly conductive, and can also serve as current paths in the semiconductor.

In conclusion, the PCE of a solar cell is closely related to the material properties and the fabrication process. For the absorber material, 1.1-1.4 eV band gap semiconductors with a high light

absorption coefficient and proper defect chemistry are desired. Other layers in the device, such as buffer material, window material and contact materials should be chosen and designed accordingly, to achieve optimal band alignment. For the processing, crack/ pin-hole-free films with high crystallinity are desired for the absorber layer. In the following chapters, the characterization of the material(s) and optimization of the processing methods will be discussed regarding how to meet these criteria for the kesterite material(s).

1.3 Solution processing for kesterite thin film solar cells

1.3.1 Thin film solar cells and the deposition methods for absorber materials

Up to 2018, the majority of the global solar market was occupied by silicon based photovoltaic modules. However, due to the indirect band gap of Si, the absorber layer has to be at the scale of a few hundred micrometers to allow enough light absorption. This makes it almost impossible to fabricate c-Si solar cells on a flexible substrate for light weight, wearable devices. Besides, with the extremely high requirement regarding the purity (impurity level ~1ppm) [7], crystallinity (Single crystal) and low defect density for semiconductor usage, the preparation and purification process for Si depends upon high temperature as well as high vacuum, which is quite energy consuming. Actually, for silicon solar cells, more than 85% of the film cost came from the feedstock and ingot /crystal preparation of Si (up to 2016) [8].

In contrast, direct band gap materials with high absorption coefficient, such as CdTe, CIGSe and CZTSSe (the crystal structures are shown in Figure 1.7), are able to absorb most of the incident light within a few micrometers. This not only makes flexible devices possible, but also dramatically reduces the cost of the light absorber layer. In commercialized thin film solar cells,

such as CdTe, the absorber material cost is less than 60% of the total module cost [8]. Despite all these advantages of CIGSe or CdTe as light absorbing thin film materials, both of them have elements that may limit terawatt scale power generation from those solar panels. For CdTe, tellurium concentration is only about ~0.001ppm in earth crust, while for CIGSe, the limiting issue is from indium. Although the ~0.05ppm concentration in earth crust seems to be adequate [9], most of refined indium is used to in ITO for transparent conducting thin films in liquid crystal displays (LCDs), and only 5% is shared for the solar market, accounting for 1.5 gigawatts power generation as of 2016 [10].

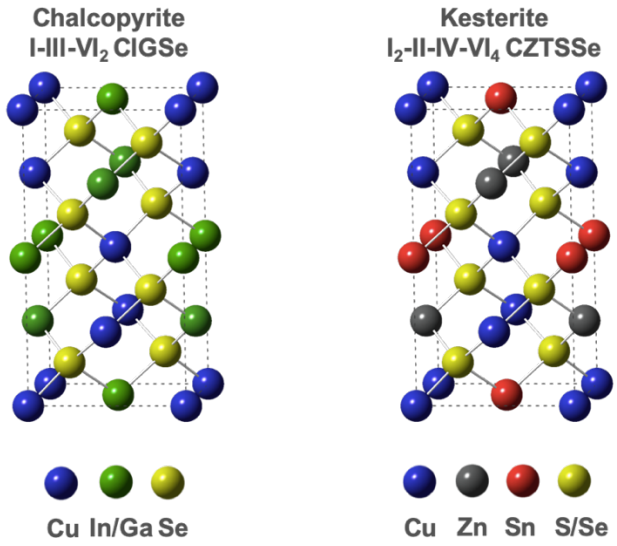

Figure 1.7 Crystal structure comparison between chalcopyrite and kesterite

1.3.2 Solution processing for kesterite thin films

Considering the factors above, a series of kesterite materials (based on $Cu_2ZnSn(S,Se)_4$ or CZTSSe) have started to draw research attention because of their high light absorption coefficient, tunable band gap (1.1-1.4 eV with different S/Se ratio), earth-abundant element composition, and low toxicity. In the current early stage of the development of this material, the fabrication of these thin

films is mostly done by sputtering [11], [12] or (co-)evaporation [13], [14]. Although these vacuum-based deposition methods allow precise control of the film composition as well as minimum extrinsic impurities, they are not energy efficient and the material utilization is relatively low.

To further bring down the cost for film manufacturing, a solution-processing approach was brought up for kesterite thin film materials. Other than electroplating [15], chemical bath deposition [16] and spray pyrolysis [17], ink-based solution deposition is one of the most widespread and robust methods for solution processed thin films. The ink can be either a uniform solution or a mixture of particles and solvent. The architecture of a lab-scale thin film solar cell is shown in Figure 1.8. Based on the different ink content, there are generally two categories of "ink": nanoparticle-based (NP) ink and molecular precursor (MP). Table 1-1 lists some of the high-efficiency kesterite solar cells with absorber layer deposited from different methods as lab-scale research cells.

Table 1-1 Comparison of solar cell performance with different deposition methods

Method	Material	V_{oc} (mV)	J_{sc} (mA/cm^2)	Fill Factor (%)	P.C.E (%)	Total area (cm^2)
Sputtering [11]	CZTSe	416	37.27	73.8	11.4	0.52
Evaporation [18]	CZTS	661	19.5	65.8	8.4	N/A
Hydrazine slurry [19]	CZTSSe	513	35.2	69.8	12.6	0.42
DMSO based MP [20]	CZTSSe	443	31.2	60.2	8.32	0.43
NP-based ink [21]	CZTSSe	404	35.1	63.7	9.0	0.48

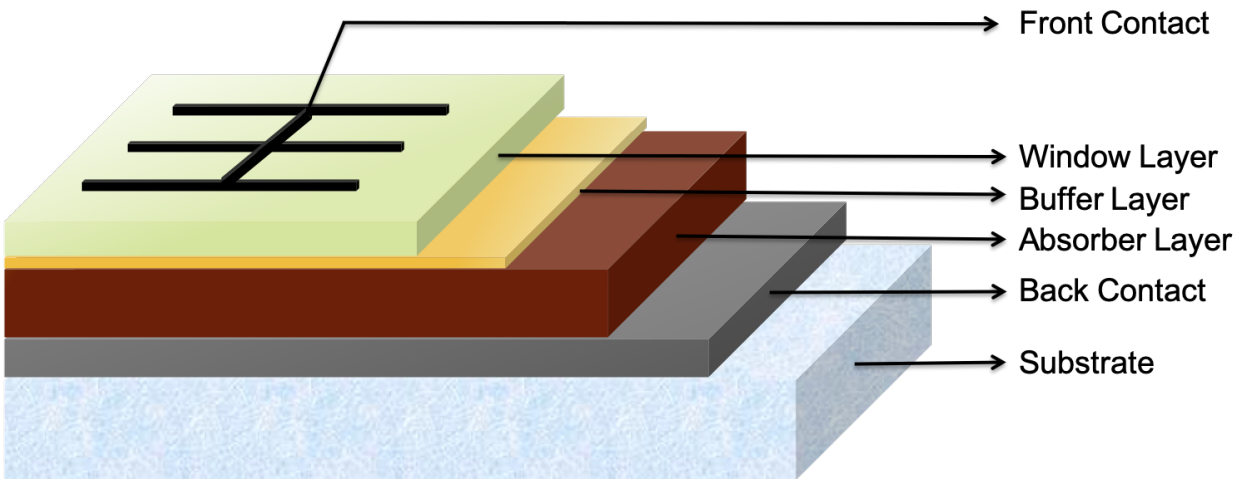

Figure 1.8 Schematic of a lab-scale thin film solar cell

For the sake of the high-tolerance nature of metal chalcogenide thin films in composition [22], [23], solution processed CZTSSe absorbers have compatible performance compared with the films deposited from vacuum-based techniques. Up to the end of 2018, the record efficiency is still hold by hydrazine based solution-processed CZTSSe thin films as absorber material. In this process, metal or metal chalcogens (Cu_2S, SnSe and Zn) were added as cation source and extra chalcogens were added as anion source. The mixture was spin coated on substrate and baked at high temperature (540 °C) with no further chalcogen treatment. The obtained film showed very high compositional homogeneity and phase purity and similar morphology as the films made from vacuum-based deposition techniques [11], [24], [25]. However, hydrazine is highly toxic and unstable, which increases the difficulty of its large-scale usage.

1.3.2.1 Kesterite thin films from molecular precursor route

Instead, more benign solvent systems came up as substitutions. An amine-thiol system has been explored extensively and intensively as the “alkahest” solvent for elemental metal, chalcogens, metal chalcogenide, as well as for metal salts [26]-[29]. For example, Zhang *et al.* used metal

chloride as the cation source in propanethiol-hexylamine system and achieved 7.86% efficiency on CZTSSe solar cells in 2014 [27]. On this basis, Zhang and Wu *et al.* found that optimized annealing conditions led to an improved efficiency from 5.1% to 9.4%. In this case, elemental metals or chalcogens (Cu, Zn, Sn and Se) were dissolved in ethylenediamine-ethanedithiol mixture[30]as the molecular precursor. Also, using oxides (Cu_2O, ZnO, SnO, and SeO_2) as the cation and anion sources, Fu *et al.* also successfully improved the efficiency to 9.7% with a mixture solvent of ethanol, butylamine and thioglycolic acid [31]. Another widely-used solvent is dimethyl sulfoxide (DMSO). DMSO is relatively less toxic and more environmentally friendly compared with the amine-thiol mixture or hydrazin mentioned above. In 2011, Ki *et al.* dissolved metal salts ($Cu(CH_3OO)_2$, $ZnCl_2$ and $SnCl_2$) and thiourea in DMSO. The solution was spin coated and annealed as a CZTS precursor film, resulting in 4.1% efficiency [32]. Revised from this work, Xin *et al.* noticed that by adding Sn^{2+} after Cu salt was fully dissolved, instead of adding all the salts at the same time, could avoid the residual of Cu^{2+} in solution, and helped the efficiency to improve to 8.3% [20].

1.3.2.2 Kesterite thin films from colloidal nanoparticle route

The colloidal nanoparticle route offers another versatile solution processing for CZTS precursor film. In this method, CZTS nanoparticles are formed in an aqueous or organic solution in the beginning. These nanoparticles are washed and collected, then dispersed in a solvent to form a colloidal ink for deposition of thin films, followed by an annealing process. Different from the baking process in molecular precursor that CZTS nanoparticles start to form in this step (as shown in Figure 1.9), the main purpose for annealing here is to remove the solvent used for dispersion and achieve densely packed large grains. Similar to the precursor film after molecular precursor

deposition, the nanoparticle films also need to be treated under sulfur or selenium vapor at elevated temperature to convert the nanoparticle film into thin films with large grains for light absorption.

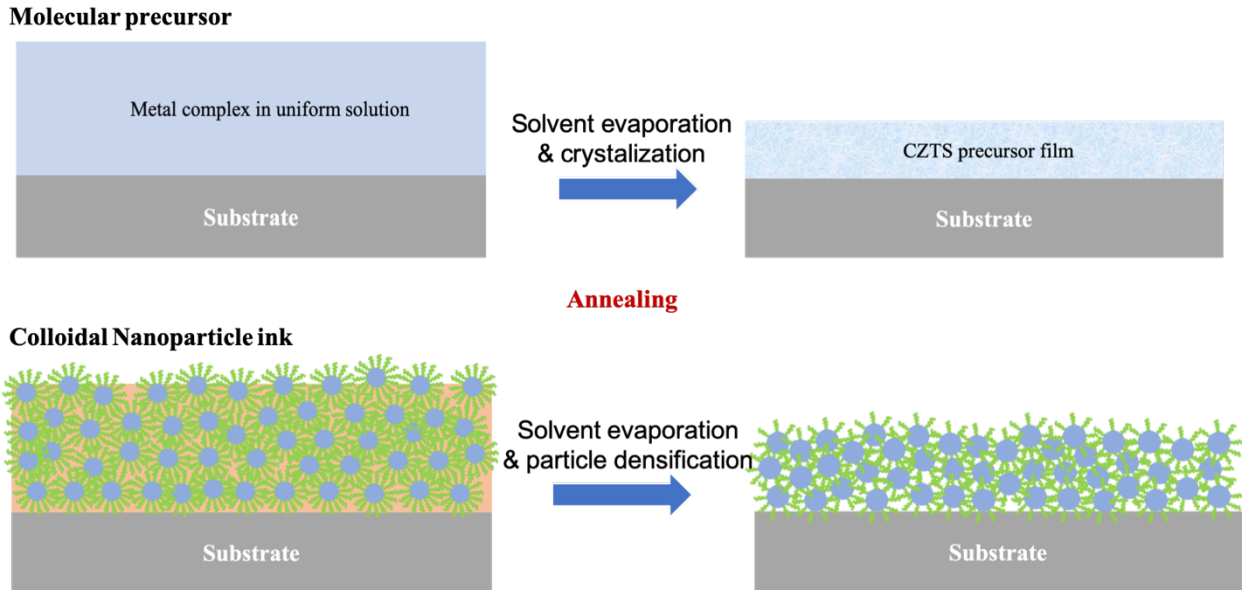

Figure 1.9 Schematic of solution processing through molecular precursor route and colloidal nanoparticle ink route.

As early as 2009, Guo *et al.* reported that CZTS nanoparticles were successfully synthetized from an oleylamine-based solvent-thermal reaction, which can be used for photovoltaic application [33], and 7.2% efficiency was reported with a modified elemental ratio between Cu/Sn and Zn/Sn [34]. With optimization of the nanoparticle synthesis, washing procedure, annealing, and selenization conditions, the efficiency was brought up to 9.0% without an anti-reflective layer from the same group [21]. Further improvements have been made by alloying the nanoparticles with different other elements, such as Ge or Ag [35], [36].

Compared with other deposition techniques, there are so many advantages of the colloidal nanoparticle-ink route. Large scale areas of CZTS nanoparticle can be synthesized within a

relatively wide temperature range in multiple different solvent systems, such as oleylamine (OLA), oleicacid (OA), octadecene (ODE), dodecanethiol (DDT) or even in an aqueous environment [34], [37]-[40]. The nanoparticle ink can be printed with high throughput and minimum material loss. Additionally, the CZTS quaternary phase is already formed in the nanoparticle before film casting, which lowers the possibility of secondary phase(s) formation during the following heat treatment.

Despite the benefits of the nanoparticle ink route, CZTSSe thin film solar cells fabricated from this method seemed to meet a bottleneck after a few years of rapid development. Other than the intrinsic material problem, which we will discuss in later chapters, the process itself has a few limitations.

First of all, CZTS crystals, occupy only a very small region in the quaternary phase diagram [37]. Once the nanoparticles are formed, the composition is fixed. Even if different concentration of precursors could be used before the reaction, the impact to the final nanoparticle composition is very limited. When CZTS nanoparticles get to their preferred composition, the extra cations may end up with being washed away during the particle washing procedure.

Secondly, as shown in Figure 1.9, when synthesized in an organic solvent, such as oleylamine, the nanoparticle surface is covered with ligands. Although these ligands prevent the particles from agglomeration in the liquid phase, oxidation when they are dry, they also leave residual after heat treatment. If the carbon species cannot be evaporated rapidly during selenization, there is a big chance that they can combine with Se and form complexes in the “fine grain” layer. The fine grain layer is characteristic for non-hydrazine processed kesterite thin films. This C-Se rich layer may

not only affect the electronic properties of the final device in vertical direction, but also rule out the possibility of making this film absorb light from both side due to its porous nature, which scatters most of light.

In the following chapters, the advantages and disadvantages of the nanoparticle ink based solution route to kesterite thin films will both be discussed. The whole process of the kesterite thin film formation is generally broken down into 3 steps: 1. nanoparticle synthesis; 2. nanoparticle film coating and baking; 3. Selenization. In chapter 2, Ag-alloyed (less than 50%) CZTSSe, including the nanoparticle synthesis and film fabrication with different stoichiometric ratios are discussed. Chapter 3 focuses on the synthesis of AZTS nanoparticles and Chapter 4 demonstrates the process of selenization for AZTSe films. Chapter 5 is a side project working on the buffer layer for nanoparticle ink based metal chalcogenide thin films.

2. SILVER-ALLOYED CZTSSE THIN FILM PHOTOVOTAICS THROUGH NANOPARTICLE ROUTE

2.1 Introduction of $Cu_2ZnSn(S,Se)_4$ and its limitation as light absorber material

Due to the terrawatt-scale energy need, thin film solar cells fabricated with earth-abundant materials have become the hotspot of photovoltaic research. Among all kinds of new materials that are under investigation, $Cu_2ZnSn(S_xSe_{1-x})_4$ (CZTSSe) draws significant attention. Similar to CIGSe, this material has a tunable band gap (with different S:Se ratio), high absorption coefficient (10^4 in visible light range), as well as being low-toxicity to both human beings and the environment. The record efficiency of solar cells using CZTSSe as an absorber layer dramatically increased from about 2.67% to 12.6% in about 12 years [19], [38], and more than 9% efficiencies are achieved by various of deposition techniques, including co-evaporation, sputtering, molecular precursor spin coating, and nanoparticle doctor blading[21], [24], [39], [40].

However, they stagnated at 12.6%, and no further improvement has been made towards higher efficiency for CZTSSe thin film solar cells as of today (February 2019). Researchers from different groups pointed out that the major loss in CZTSSe solar cells is from open circuit voltage (V_{oc}). The difference between the optical band gap (Eg) and the measured open circuit voltage (V_{oc}) can be described as:

$$V_{def} = \frac{Eg}{q} - V_{oc} \tag{2.1}$$

where q is the electron charge. For all the solar cells with ~20% efficiencies, such as GaAs, c-Si, methyl-ammonium lead iodide based perovskite, and CIGSe, their V_{def} are under ~40% Eg; while even for CZTSSe solar cells with record efficiency, V_{def} is about 62% of its optical band gap [41].

Gokmen *et al.* from IBM are among the pioneers suggesting that band tailing is the fundamental bottleneck of this material [42]. They demonstrated a significant disagreement between the band gap energy interpreted from internal quantum efficiency (IQE) and photoluminescence spectra (PL) by comparing CZTSSe (10.7 % PCE) and CIGSe solar cells (10.7 % PCE). The band gap energy of CZTSSe films determined from PL is about 100 meV higher than that in IQE. They proposed that this difference is coming from the band gap fluctuation or electrostatic potential fluctuation as shown in Figure 2.1.

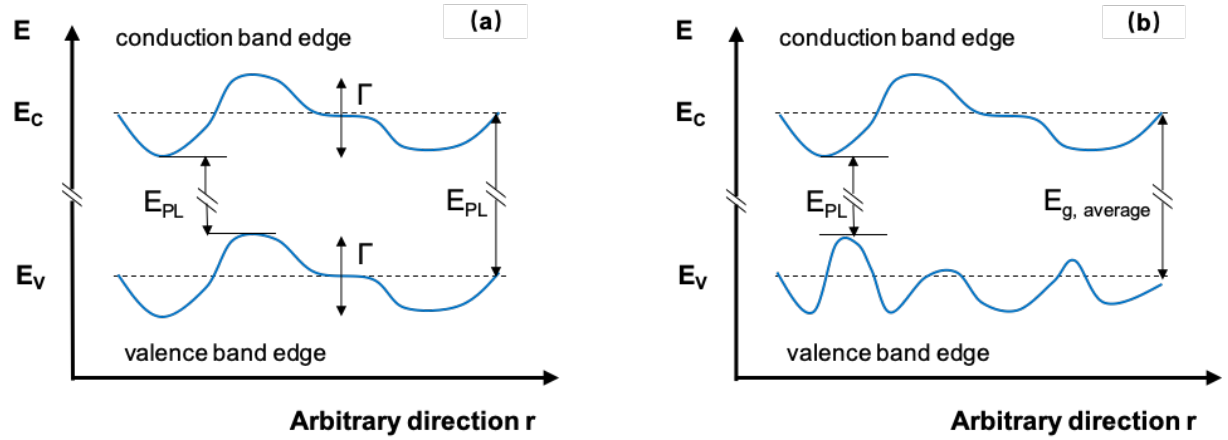

Figure 2.1 The schematic of (a) electrostatic potential fluctuation, and (b) band gap fluctuation

The Eg extracted from IQE reflects the absorption from the highest point of valence band to the lowest point of the conduction band after the fluctuation, while the peak in PL spectra contains all the conduction-to-valence band emissions, and the peak position corresponds to an average distance between the conduction band minimum and valence band maximum. It also explains why the PL peak in CZTSSe thin film is broadened, with a full-width at half-maximum (FWHM) of 110 nm, while that value of CIGSe thin film is only 60 nm, due to fewer defect states in contrast with CZTSSe.

For the origin of the defects in CZTSSe [43], [44], Chen *et al.* concluded that the intrinsic defects/ defect clusters generate trap states for electrons, which is detrimental to the PCE of CZTSSe solar cells. Generally, the CZTSSe that are used for absorber materials are in a kesterite structure (I_2-II-IV-VI_4, space group $I\bar{4}$) as shown in Figure 2.2. S or Se atoms occupy the center of alternating tetragons, which are located at z=1/8, 3/8, 5/8 and 7/8 planes of the lattice. For the cations, Cu and Sn atoms are located at z=0 and z=1/2 planes with alternating arrangement; so do Cu and Zn atoms, which are located at z=1/4 and z=3/4 plane.

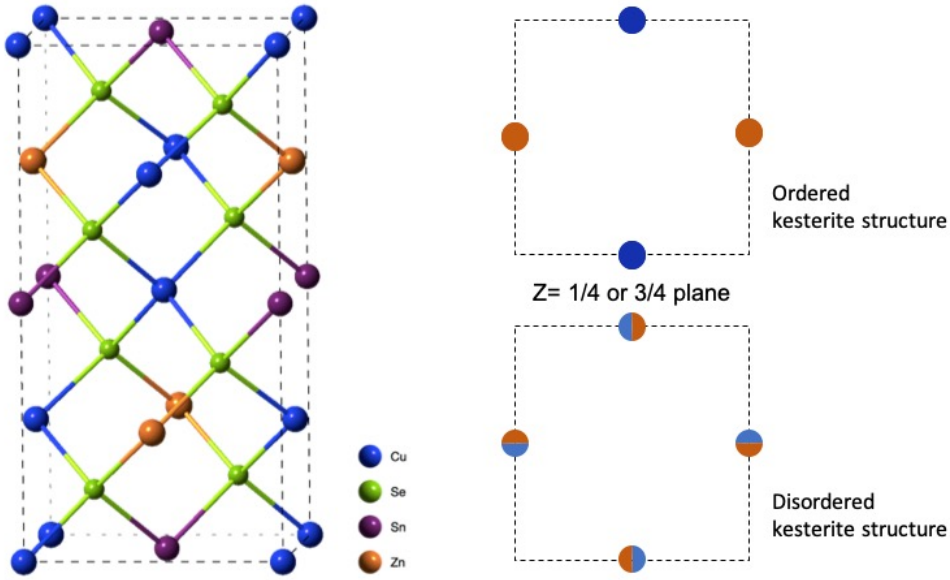

Figure 2.2 Crystal structure of kesterite CZTSe and the ordered and disordered z=¼ or ¾ plane

According to the lattice structure, the stoichiometric ratio should be Cu:Zn:Sn:S or Se = 2:1:1:4. However, almost all of the reported CZTSSe solar cells has a significant off-stoichiomety composition, normally Cu-poor and Zn-rich. Other than the possibility of secondary phase(s) ($Cu_{2-x}S$, ZnS, SnS, SnS_2 or Cu_2ZnS_3) formation, the non-stoichiometric composition can also be a product of intrinsic point defects. Compared with binary CdTe or ternary CISe, while also adapted from diamond cubic or zinc blend structure, the CZTSSe lattice contains more elements and more

species of intrinsic point defects, including vacancies, interstitials as well as anti-site defects, such as Cu_{Zn}, Zn_{Cu} Sn_{Zn} Cu_{Sn} *etc*.. A high population of those point defects will generate defect or trap states in between the band gap, which will strongly affect the carrier concentration, recombination and the open circuit voltage CZTSSe solar cells. Among all different species of point defects, V_{Cu} gives very shallow acceptor defects and is mainly responsible for the p-type behavior of CZTSSe, and [Cu_{Zn} +Zn_{Cu}], as an acceptor-donor pair, has the lowest formation energy, since Cu and Zn have similar size and chemical valence [43]. Giving the high population of Cu-Zn bonding in CZTSSe, if we assume the density of such anti-site defects can be calculated by an Arrhenius equation associated with the density of Cu-Zn bonds:

$$N_{defect} = 2N_{bond}\exp\left(-\frac{Ea}{k_B T}\right) \qquad 2.1$$

in which *Ea* is the activation energy for these anti-site defects, the defect density can be as high as ~10^{29} cm^{-3} even at room temperature, giving the calculated activation energy of only 0.2 eV [42]. Even for deep defects such as Sn_{Cu}, the concentration can be as high as 10^{16} cm^{-3} at 800 K, which is commonly a CZTSSe synthesis temperature, which is almost comparable with the carrier concentration in this semiconducting material[45].

For different kinds of defects or defect clusters, there are different opinions regarding how they affect the final performance of the solar cell. Some work has demonstrated that these defect clusters might be benign. Based on a First Principle Calculation, Wei *et al.* concluded that [Cu_{Zn} +Zn_{Cu}] only results in a very slight valence band edge shift. Furthermore, the ionization of Cu_{Zn} can even help with the generation of holes and improve the carrier conductivity [43]. Instead, the donor defects, such as Sn_{Cu}, Sn_{Zn}, offers defect states for the recombination of electrons and holes. Experimentally, Hempel and Unold *et al.* also showed that by using time-resolved terahertz

spectroscopy to determine that the carrier lifetime, that the characteristic of the trap defect density, was not relevant to the Cu-Zn disorder [46]. On the contrary, Scragg *et al.* experimentally confirm that the density of Cu-Zn anti-site defects is significantly correlated to the degree of band edge fluctuation [47]. Zawadzki and Lany *et al.* combined those different results and show that, because of the disorder of Cu and Zn, charged cation clusters/ other cation disordered defects were formed, which dramatically changed the electrostatic potential fluctuation, therefore leading to severe band tailing [48].

Despite the dispute of which defect(s) should be responsible for the *Voc* deficit, all the evidence pointed out that, CZTSSe does not have preferred defect properties compared with traditional metal chalcogenide light absorbing materials, such as CIGSe or CdTe. To improve the defect behavior, different elements were added into this quaternary system as doping or alloying, including lithium [40], germanium [49],[36] [50] cadmium [51] and silver [52] [35], [53], [54]. Among all those substitutions (partially or fully), Ag achieved remarkable performance regarding the power conversion efficiency. By either introducing a silver-graded absorber layer or by using a small doping level of Ag, Wu *et al.* achieved more than 10% PCE with enhanced open circuit voltage compared with CZTSSe solar cells [53], [55]. However, most of this work was based on molecular precursor route for the ACZTSSe thin film. As another competitive solution processing method, how the silver incorporation will influence the AZTSSe thin films will be discussed from the nanoparticle ink route from following methods:

a. How does Ag/ Ag compound coated on top of the nanoparticle film changes the selenization behavior, as well as the resulting photovoltaic performance?

b. If Ag is added during the nanoparticle synthesis, how would the original kesterite system takes different amount of Ag during nanoparticle synthesis as well as large grain formation?

c. How are the film morphology and optoelectronic properties are affected by different level of Ag-alloying?

2.2 CZTS nanoparticles with different Ag concentration

2.2.1 Experiment

The nanoparticle synthesis was following the recipe of previous work [21], [35]. Silver was added into the system as silver acetylacetonate (Ag(AcAc), 98 % Sigma-Aldrich) along with all the other cation sources. In this section, ACZTS nanoparticles with [Ag]: [Ag+Cu] ratio of 10%, 20%, 30%, 40% and 50% are prepared according to the precursor concentration. All the nanoparticles were synthesized with the composition of [Cu+Ag]: [Sn]=1.74 and [Zn]: [Sn]=1.05, which are Cu-poor and Zn-rich, as demonstrated by most high efficiency kesterite absorbers. To prepare the (scanning) transmission electron microscopy samples, the nanoparticles were dispersed in hexanethiol (HT) at the concentration of 250 mg/mL, and then diluted in toluene by 1000 times. This diluted nanoparticle ink was ultra-sonicated for 15 min and then immediately drop cast (30-50 μl) on a silicon nitride (SiN) grid (5 nm thick SiN film, SiMPore Inc.).

2.2.2 Characterization on the ACZTS nanoparticles

The X-ray diffraction patterns for CZTS nanoparticles with different concentration are shown in Figure 2.3. From 0% to 20% Ag alloyed CZTS nanoparticles, the XRD patterns of ACZTS nanoparticles matches the standard CZTS (space group I-4) perfectly, except for the left shoulder on the (112) peak, which may correspond to stacking faults in the nanoparticles. Since the stacking fault in kesterite CZTS may result in a local wurtzite structure, the (100) peak of wurtzite CZTS

presents as a small shoulder at the (112) peak of kesterite CZTS. For nanoparticles that contain more than 30% [Ag]/[Cu+Ag], peaks from secondary phases show up; most of them are for ZnS and SnS_2. However, based on the calculations from Gong *et al.*, we should see a lattice parameter change from pure CZTS towards AZTS [56]. If Vegard's law is applied, a 0.35° peak shift to the low angle side is expected of (112) peak from 0% and 50% Ag-alloyed CZTS. This implies two possibilities: either the Ag-alloyed CZTS nanoparticles are highly strained to compensate to the large size Ag atoms, or Ag does not fully incorporate into the lattice during this nanoparticle synthesis.

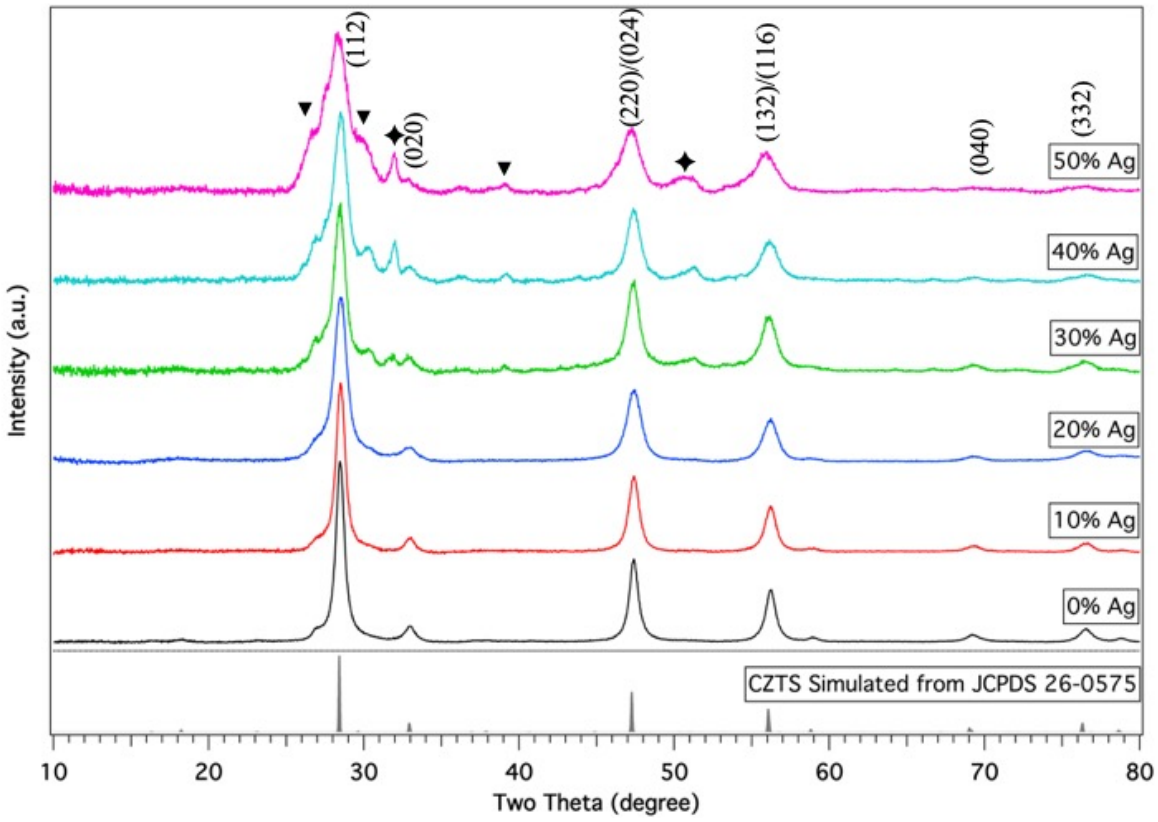

Figure 2.3 XRD of CZTS nanoparticles with 0%, 10%, 20%, 30%, 40% and 50% of [Ag]/ [Ag+Cu] ratio as a comparison to the standard CZTS. The triangle marks are for the diffraction peaks from ZnS and the star markers are for the diffraction peaks from SnS2.

To further explore the form of Ag exists in nanoparticles, high resolution STEM equipped with EDS detector was employed. 20% and 50% Ag-alloyed nanoparticles were used as examples. For the 20% Ag-alloyed CZTS, the STEM image is shown in Figure 2.4 (a). Most of the particles have irregular shapes with an average size around 30-40 nm, which are different from CZTS nanoparticles [57]. The few bright spots, representing high atom number elements, are confirmed to be silver-rich points. This also explains why there is no peak shifting in XRD of these nanoparticles. A considerable amount of silver did not exist as ACZTS nanocrystals. If these tiny spots of silver or silver sulfide were amorphous, XRD was not able to pick up any signals from them. Another notable difference from CZTS nanoparticles is there is a significant composition non-uniformity, especially for Zn. A few particles show higher Zn, as well as lower Cu and Sn concentration, compared with other surrounding particles. However, these Zn-rich particles do not share a common shape or size.

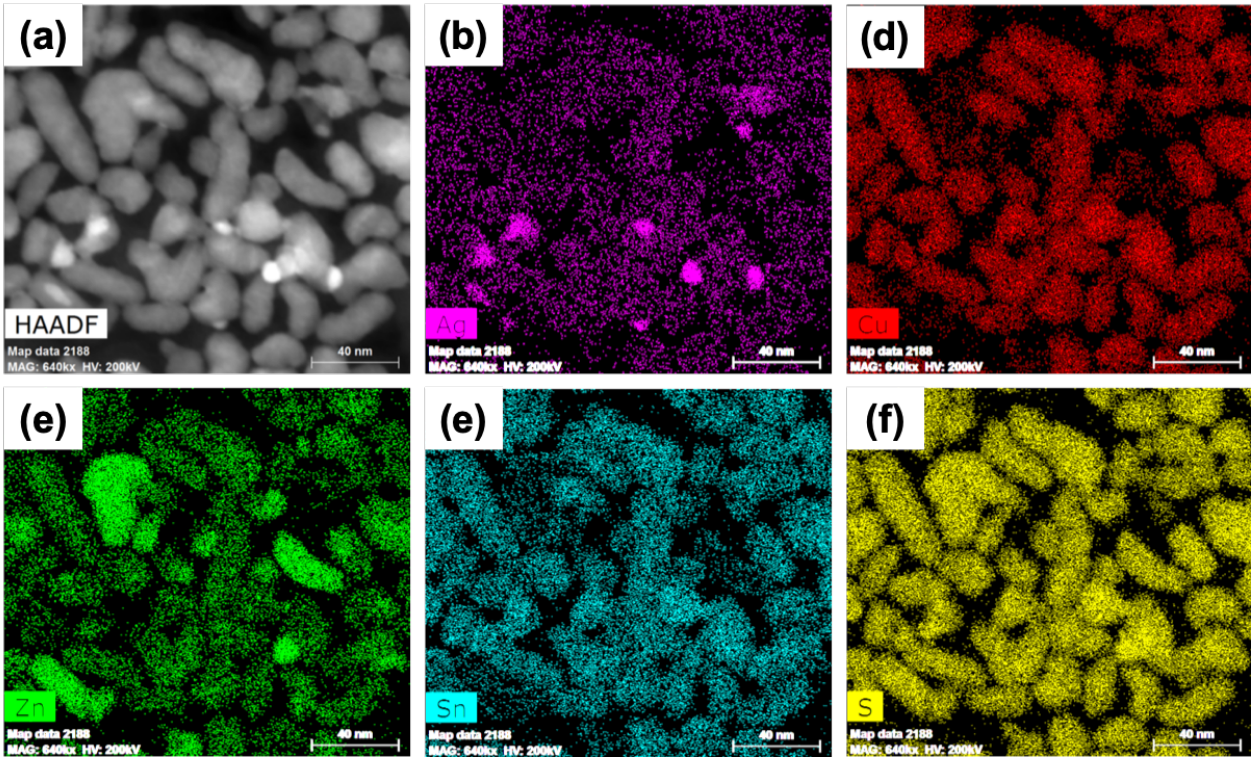

Figure 2.4 (a) STEM image of 20% Ag-alloyed CZTS nanoparticles and the corresponding elemental distribution of (b) Ag, (c) Cu, (d) Sn, (e) Zn and (f) S

For 50% Ag-alloyed CZTS, from the low-mag TEM view, there were two distinct microstructures as shown in the TEM image of the particles (Figure 2.5 (a)). One species is thin slice or nanosheet with diameters as big as a few micrometers, which are SnS_2 confirmed with EDS. The others are nanoparticles with a very wide size distribution. Different from the 20% Ag-alloyed case, the big particles are hundreds of nanometers and the small particles are less than 10 nm. This agrees with the XRD peaks from 50% Ag-alloyed CZTS having been broader than 10% or 20% ACZTS.

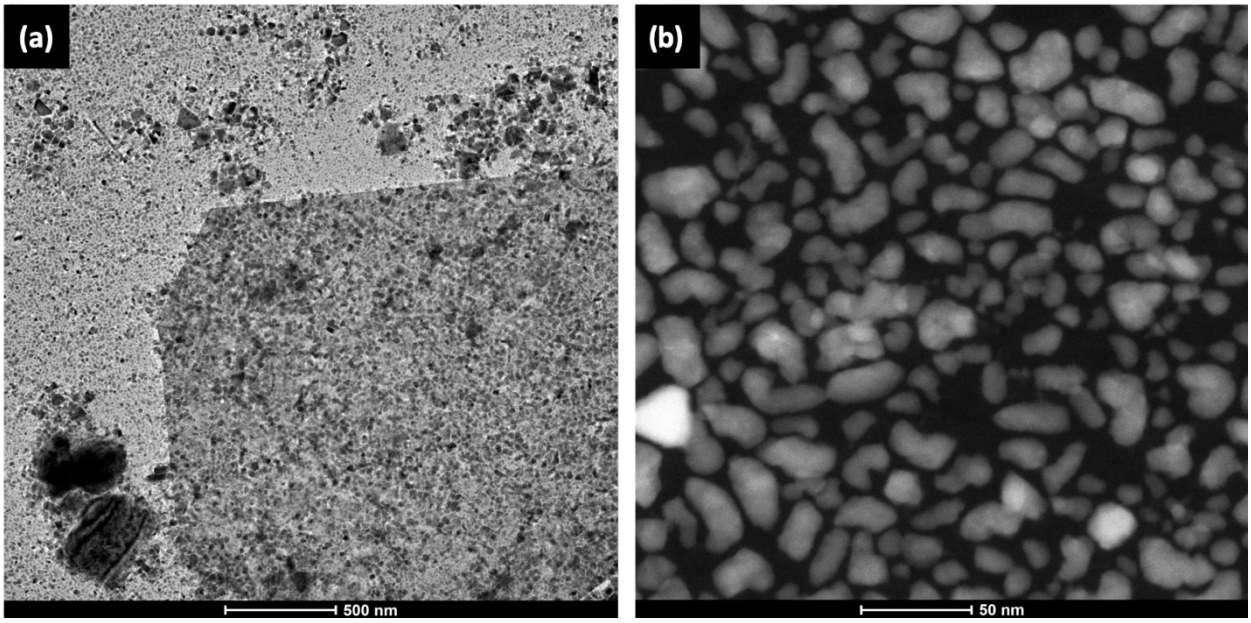

Figure 2.5 (a) TEM and (b) STEM image for 50% Ag-alloyed CZTS nanoparticles along with ZnS and SnS2 secondary phases.

2.3 CZTSSe thin films with different Ag concentration

2.3.1 Experiment

The nanoparticles we describe previously were dispersed in hexane-thiol at the concentration of 250 mg/ml. 15mL nanoparticle ink was drop cast on one edge of a 5 cm* 2.5 cm molybdenum coated (800 nm) soda lime glass and then doctor bladed into thin films in ambient atmosphere. The as-coated film was drying in the fume hood for 4 min before it was annealed on a hotplate at 300°C for 1min.This process was repeated for the second time to obtain a total film thickness around 800 nm. For the pure CZTS nanoparticle film, two Ag coating methods were applied here: I. 10nm-thick layer of Ag was thermally evaporated onto it before selenization. II. Molecular precursor with [Ag]: [Zn]: [Sn]= 1.7 :1.2 :1 was spin-coated on top of the CZTS nanoparticle film. For the molecular precursor, 1, 2-Ethanedithiol (>98%, Sigma-Aldrich) and hexylamine (99%,

Sigma-Aldrich) with 1:1 volume ratio was used as solvent. Silver acetylacetonate ($Ag(C_5H_7O_2)$ 98%, Sigma-Aldrich), zinc acetylacetonate hydrate ($Zn(C_5H_7O_2)_2 \cdot xH_2O$, 99.995% trace metals basis, Sigma-Aldrich) and tin(IV) bis(acetylacetonate) dichloride ($Sn(C_5H_7O_2)_2Cl_2$, 98%, Sigma-Aldrich) are used as the cation source or solute at the [Sn]=0.02 M.

These surface-coated CZTS nanoparticle film as well as Ag-alloyed CZTS nanoparticle film were enclosed with ~260-280 mg of Se pellets (>99.99% trace metals basis, Sigma-Aldrich) in a graphite box. The graphite box was inserted into a tube furnace after the tube was purged with Ar for 3 times and preheated to 500°C. After 40 min of selenization, the furnace was opened and the tube was cooled in air, which took about 80 min from 500°C to less than 50°C. Right after selenization, a 50 nm cadmium sulfide (CdS) was deposited on the selenized film by chemical bath deposition, followed by ZnO (80 nm, sputtering)/ ITO (220 nm, sputtering)/Ni (100 nm, e-beam)/ Al (2.5 μm, e-beam) to finish the photovoltaic devices.

2.3.2 CZTSe films with Ag-containing top coating

A silver/ silver-contained compound coating on top of the nanoparticle film is used to enhance the grain growth during selenization [35]. It also has been confirmed that higher concentration of Ag at the p-n junction will be helpful to create favorable defect formation and retard the Fermi level pinning[53], [58]. Figure 2.6 shows the microstructures of the selenide films with different surface treatment as a comparison to the pure CZTSSe case from the top view in SEM. The ratios between different cations in these three samples are also compared based on SEM-EDS, as is listed in Table 2-1.

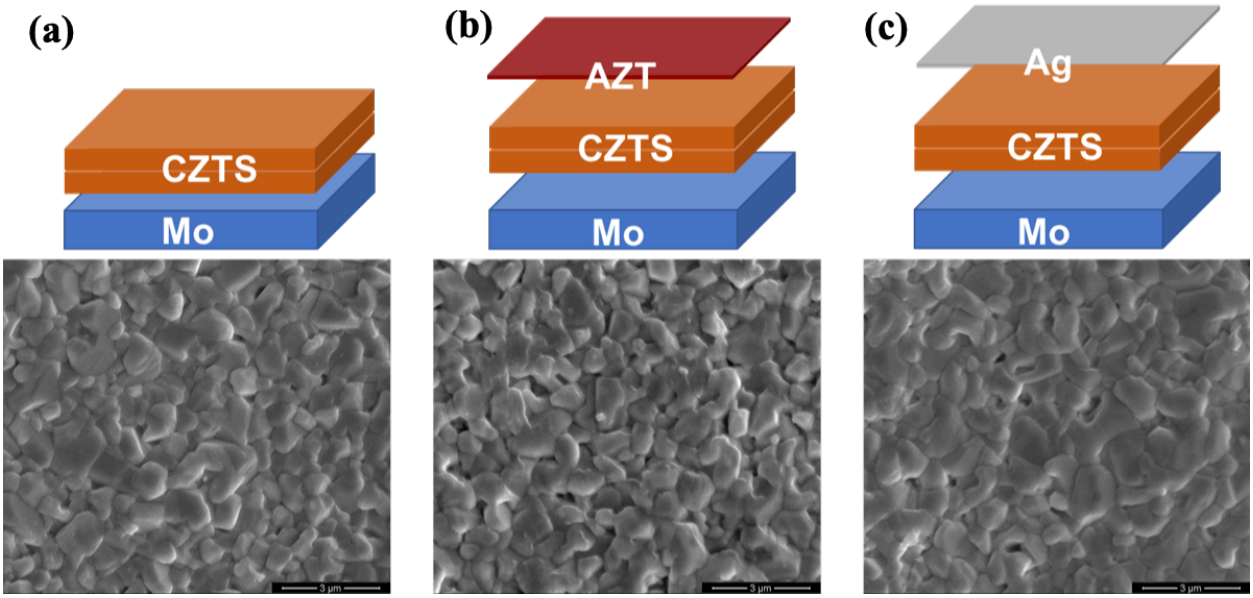

Figure 2.6 The architectures (before selenization) and SEM top-view images of (a) reference CZTSSe, (b) CZTSSe with AZT precursor coating and (c) CZTSSe with elemental Ag coating. All the scale bar in the SEM images are 3μm.

Table 2-1 Atomic composition and efficiency comparison among different surface treatment

Sample	[Cu+Ag]/[Sn]	[Zn]/[Sn]	Efficiency
CZTSSe	1.81	1.02	6.37%
AZT-CZTSSe	1.80	1.07	6.56%
Ag-CZTSSe	1.97	1.03	4.06%

The top views of the selenized films look very similar to the normal CZTSSe films. Only the film with Ag coating on top has bigger grains as well as less faceted surface features, which was probably because of higher concentration of Ag at the top [35]. However, this film had the lowest efficiency among the three. Associated with the composition, after elemental Ag coating, it broke the stoichiometry of the nanoparticles by adding more +1 cations. As a result, the [I]/ [IV] was almost 2. However, high-Cu or near-stoichiometry Cu concentration is not favorable for the acceptor defect formation, as we demonstrated before. This problem may be resolved by starting

with nanoparticles with even poorer Cu condition with more detailed study. By contrast, when Zn and Sn are coated along with Ag, the original cation ratio is reserved and has improved PCE compared with the original CZTSSe solar cell.

For the cell with best performance from AZT-coated CZTSSe solar cells, a thin slice of the cross-section of this device was cut and lifted out for STEM. It is noticeable that the fine grain layer is about 500 nm thick. This is significantly thicker than the champion nanoparticle ink processed CZTSSe films, which may have a negative impact on the solar cell performance regarding increased series resistance [21]. This probably comes from the organic complexes we introduced through the molecular precursor. The amine-thiol combination made more complexes that cannot be removed during selenization. The silver distribution after selenization is also studied in STEM equipped with EDS. EDS signals were collected from the area indicated by the yellow rectangle, shown in Figure 2.7, and the elemental atomic percentages are listed in Table 2.1.

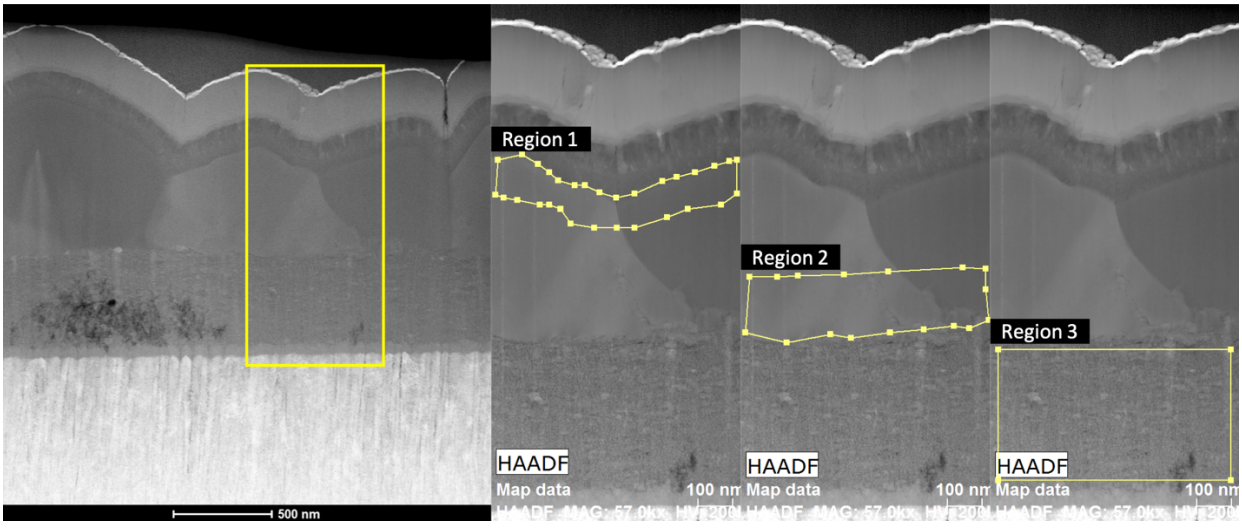

Figure 2.7 Indication of different regions for quantitative EDS analysis

Table 2-2 Composition of different regions in AZT-coated CZTSSe film after selenization

Region	Ag/ at. %	Cu/ at. %	Zn/ at. %	Sn/ at. %	S/ at. %	Se/ at. %	C/ at. %	[Ag]/[Ag+Cu]
Region 1	1.26	24.49	14.53	11.97	6.95	40.80	0	0.049
Region 2	0.18	24.46	12.64	12.45	10.17	40.11	0	0.007
Region 3	0.77	49.87	2.82	2.26	8.57	29.23	6.48	0.015

Since the silver concentration is quite low, the vertical line scan was not able to distinguish the concentration difference. As a result, integration of signals from different areas along the thickness were used to determine the elemental concentration. Comparing the composition between the top region (region 1) and the bottom region (region 2) of the large grain area, silver is found to have mostly stayed at the top region, since the amount of silver on the top is about 7 times of that in the bottom of the large grain. This result agrees with the previous research that shows the selenization is a process from top down [59]-[61]. Other than a small amount of silver in the molecular precursor might infiltrate into the nanoparticles layer before selenization, it would be very difficult for Ag atoms to diffuse to the bottom. Because once the top layer of (A)CZTSe grains are formed, Ag atoms can only get to the bottom through solid phase diffusion, which is much slower than the diffusion in liquid selenium, the material transport method in nanoparticles during selenization. The composition in the fine grain layer (region 3) is very different from that in large grains. It is significantly Cu rich. This is partially because of the artifact during TEM sample preparation because Cu is very mobile under the ion beam flush. Other than Cu, Se, S and carbon are left in the fine grain layers as they are the leftover of the reaction product from selenium and oleylamine based organics [62]-[64].

2.3.3 ACZTSSe thin films with Ag-alloyed nanoparticles

2.3.3.1 Crystallographic change with Ag-alloying

The Ag-CZTS nanoparticle films with different Ag concentrations were selenized in a tube furnace. The crystallographic information was checked in XRD and is shown in Figure 2.8. For the CZTSe film with no Ag alloying, all the peaks match with standards but are slightly shifted to the high angle direction. This is because of the sulfur residual in the film, making the lattice slightly smaller than that of pure selenide. No peaks from secondary phase(s) were detected from the XRD patterns. When increasing amount of silver was added into the system, all the XRD peaks shifted to the low-angle side, corresponding to the Ag-induced lattice expansion. Furthermore, (220) and (204) peaks started to split due to a different c/a ratio in CZTSe and AZTSe system, which was also the case for peak (132) and (116). The d-spacing between (112) planes is calculated from the (112) peak position in XRD patterns as a function of different Ag content. As a comparison, the theoretical values for (112) d-spacing were calculated assuming a linear relationship of the lattice parameter between standard CZTSe and AZTSe as shown in Figure 2.9. All the experimental data are smaller than the calculated d-spacings because of the residual sulfur. The d-spacing gradually increased from 0% to 50% [Ag]/[Ag+Cu] (the line between point does not imply an linear relationship between different compositions.). It is noticeable that when [Ag]/[Ag+Cu] is at 40% or 50%, the distance between the theoretical value and experimental value is decreased significantly, demonstrating more completed selenium substitution for sulfur.

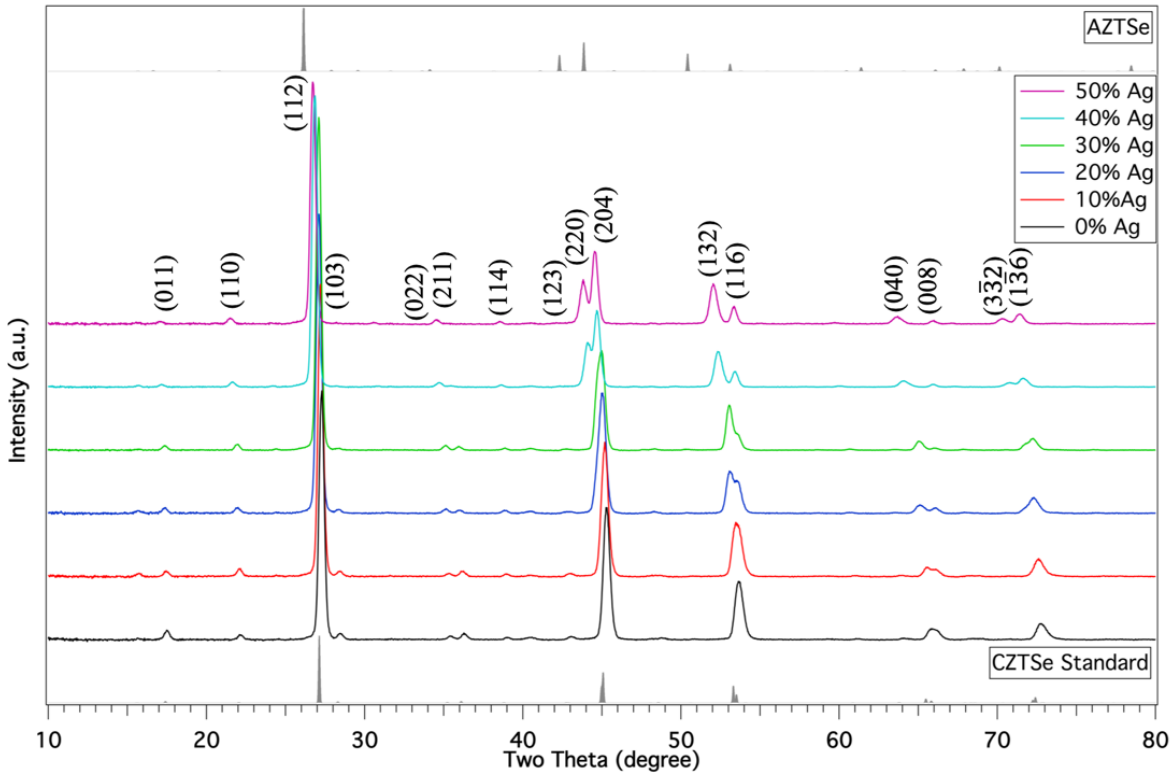

Figure 2.8 XRD patterns of Ag-alloyed CZTSSe thin films with different Ag concentration as a comparison to CZTSe (JCPDS 01-070-8904) and AZTSe (Simulated pattern based on the crystallography information provided from Gong et al. [65]) standard

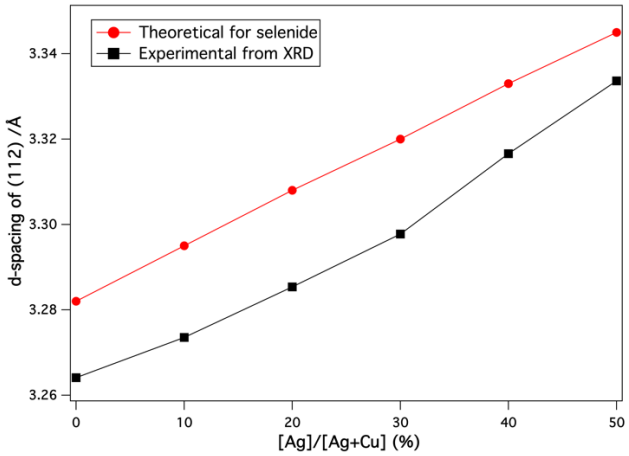

Figure 2.9 Comparison between calculated and XRD measured d-spacing of (112) plane

Raman spectra were measured for these selenized thin films with an incidence laser wavelength of 633 nm, as shown in Figure 2.10. Other than the 4 peaks coming from CZTSSe, there is an additional peak at ~330 cm^{-1}, which is from the residual sulfide nanoparticles. With the increase of the Ag concentration in the lattice, the peak from sulfide nanoparticles became less significant, suggesting that Ag-alloying helps with the processing of converting sulfide nanoparticles to selenide thin films, which agrees well with lattice parameter calculated from the XRD pattern.

The peaks located at 175 cm^{-1} and 197 cm^{-1} correspond to the A mode vibration in CZTSSe. The anions are involved in the A-mode vibration. For example, the peak 197 cm^{-1} is from the stretching of Sn-S bonding. The sharpness of this peak represents anion ordering between S and Se. From 0% to 30% Ag-alloying CZTSSe, the sharpness of this peak increased, showing a more sulfur depleted situation with increased Ag content. While when Ag concentration increases further to 40% or 50%, there is no significant change in the sharpness of this peak. Although only anion stretching is involved in the A mode here, when the crystallography environment of S or Se changes, such as by Cu-Zn disordering, the stretching frequency of will change as a result [66]. The asymmetry and widening of the A peak in pure CZTSSe Raman spectra is such a case. The order-disorder can also be identified by the intensity of A mode to B mode (248 cm^{-1}) and E mode (233 cm^{-1}), demonstrated by Scragg *et al.* [67], but it is not significantly applied in our situation. An incident laser with close to resonant wavelength may be needed to reveal more detailed changes in the crystal structure.

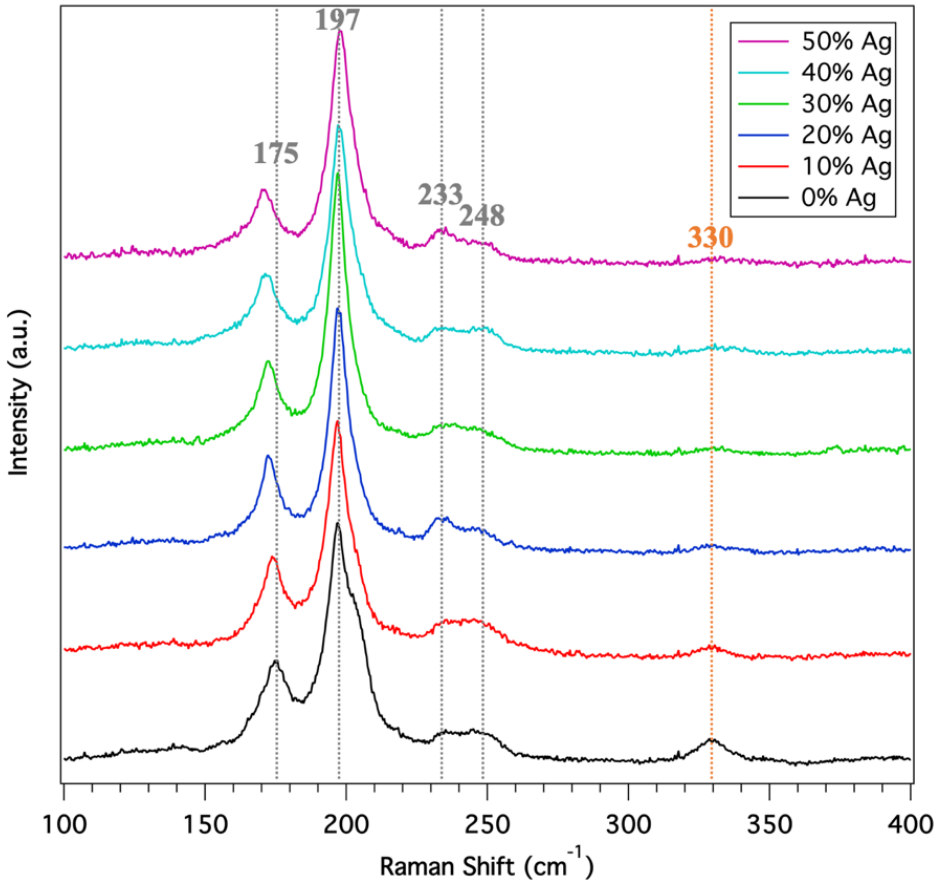

Figure 2.10 Raman spectra of the selenized films with different Ag concentration. The grey lines correspond for the standard CZTSSe and the orange one corresponds for standard CZTS

2.3.3.2 Microstructure change with Ag-alloying

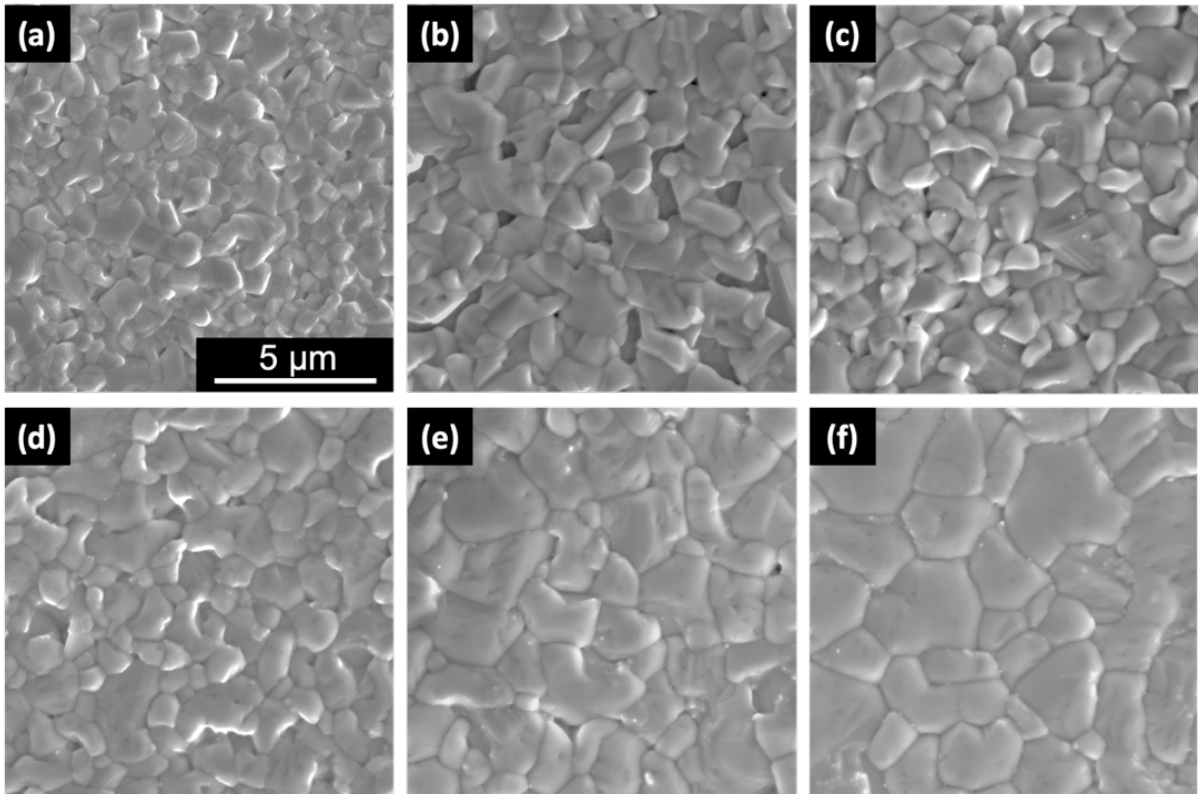

Figure 2.11 Top view of the ACZTSSe films with [Ag]/[Ag+Cu] ratio at (a) 0%, (b) 10%, (c) 20%, (d) 30%, (e) 40% and (f) 50%.

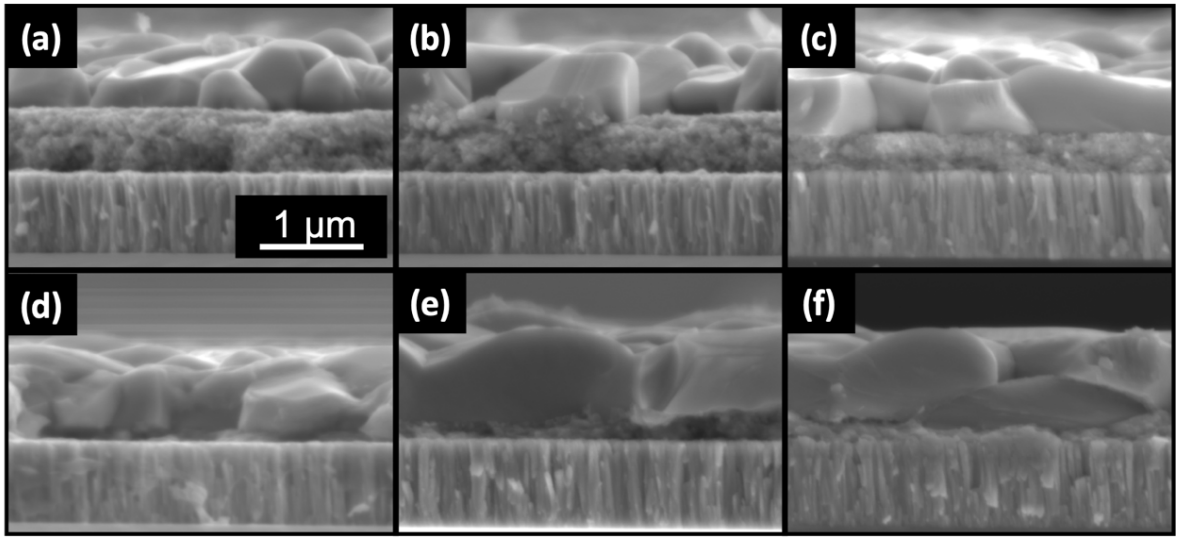

Figure 2.12 Side view of the ACZTSSe films with [Ag]/[Ag+Cu] ratio at (a) 0%, (b) 10%, (c) 20%, (d) 30%, (e) 40% and (f) 50%.

Table 2-3 Grain Size changes with composition

Ag concentration in precursor	0%	10%	20%	30%	40%	50%
grain size(μm)	0.98	1.4	1.84	1.94	2.99	7.38
[Cu+Ag]/Sn	1.74	1.79	1.84	1.89	1.93	1.92
[Ag]/[Cu+Ag]	0	0.10	0.21	0.28	0.46	0.52
[Zn]/[Sn]	1.02	1.04	1.05	1.08	1.11	1.07
[S]/[S+Se]	0.20	0.12	0.11	0.09	0.07	0.05

The top and side views of these selenide films are shown in Figure 2.11 and Figure 2.12. The corresponding ratios of different cations are also listed as obtained from EDS. For the [Ag]/[Ag+Cu] ratios, the measured values agree with the chemical ratios added into the reaction. [Zn]/[Sn] also keeps relatively the same. The sulfur composition is significantly reduced with enhanced Ag alloying level, which is consistent with the Raman or XRD conclusion. At the same time, the [Ag+Cu]/[Sn] or [I]/[IV] ratio increases with the increase of Ag concentration, although they were the same in the starting precursor. Based on first principle calculations, the V_{Cu} is one of the primary defects formed in CZTSSe due to its low formation energy[43], so Cu-poor CZTSSe is thermal dynamically favorable. When Ag is incorporated into the system, these defects have higher formation energy because Ag lowers the valence band position. As a result, the I cation vacancy is decreased and [I]/[IV] increases accordingly [58].

From the SEM top view images, it can be clearly seen that the grain size is increasing with the Ag concentration and the average grain size of each film is listed. The average grain size is estimated by counting more than 100 grains in a certain area. The grain diameter d is expressed as:

$$d = \frac{1}{(N_a)^{1/2}} \quad 2.2$$

in which Na is number of grains per unit area. The composition of the films as well as the average grain sizes of different Ag alloying levels are shown in Table 2-3. These were different from the sulfide case. Both experimental and simulation results show that Ag incorporation made CZTS grains smaller [51], [68]. Besides, from the side-view SEM images, it also showed that the fine grain layer was significantly reduced. The reduced fine grain layer may come from the two reasons:

a. The Ag-alloyed CZTS nanoparticles have bigger grain size, which means the surface-to-volume ratio is smaller than that of the pure CZTS case compared with previous studies [21], [69]. As a result, the density of ligands attached to the surface of the nanoparticles is reduced. Since most of the fine grain layer is a reaction product of selenium and carbon species from the ligands, the bigger nanoparticles will give less carbon-selenium complexes.
b. There are also some unreacted nanoparticles left in the fine grain layer. Since Ag accelerates the selenization, the reaction at a higher Ag alloying level is more completed compared with pure CZTSSe. Fewer unreacted nanoparticles are left in the fine grain layer as a result.

Other than the grain size and fine grain layer thickness, the grain top is getting flatter with increased Ag concentration in the film. The flat surface of the light absorber layer is also preferred for the photovoltaic performance. With a flat surface, the sequential layer deposited on it will be more uniform. Less light scattering and lower series resistance is expected with a flat interface. To examine if the all the elements were uniformly distributed after selenization, a 20% Ag-alloyed CZTSSe device was cut using FIB to look at the cross-section.

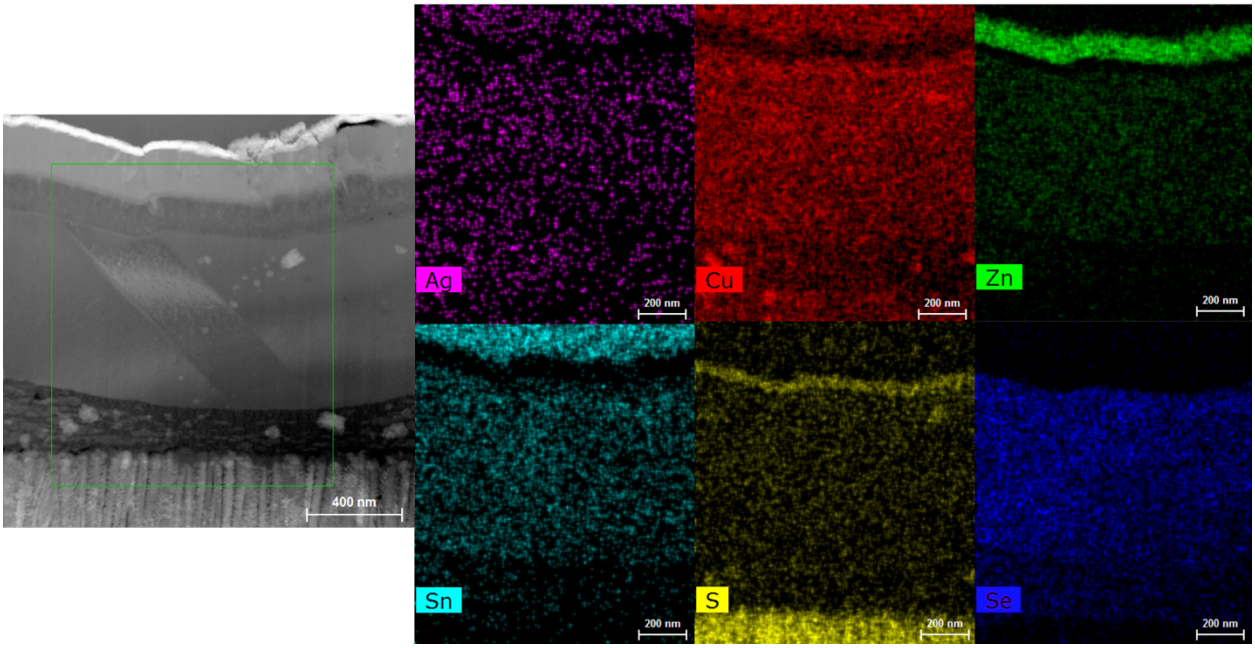

Figure 2.13 STEM-EDS mapping of Cu, Ag, Zn, Sn, S and Se in a 20% Ag-alloyed CZTSSe devices. From top-down, the layers are corresponding to Pt-capping layer/ Au conducting layer/ ITO/ ZnO/ CdS/ ACZTSSe/ fine grains layer/ Mo. The bright spots on surface of the large grains are oxides introduced by surface oxidation.

From Figure 2.13, it can be seen that although no secondary phase(s) were shown in XRD or Raman, the absorber large grains still have some Ag-rich spots. These fluctuation of composition across the large grain may results in trap states, increase the recombination rate and reduce the efficiency compared with the pure CZTSSe case.

The high concentration of Ag does not necessarily correlate with high PCE of the solar cell. Instead, the highest efficiency came from relatively low Ag-alloying level, such as 3% or 5% [35], [53], [55]. More detailed study on the optoelectronic properties of ACZTSSe thin films need to be studied.

2.4 5% Ag-alloyed CZTSSe thin films with different [I]/[IV] ratio

In this section, [Ag]/[Ag+Cu] ratio is fixed at 5%, which was shown to achieve relatively high efficiencies in previous work[35]. However, the [I]/[IV] was set to be the same as pure CZTSSe case. Based on the previous discussion, it is concluded that [Ag+Cu]/[Sn] also plays an important role in the defect chemistry. Here, the focus is on how the [I]/[IV] ratio will affect the optoelectronic properties of the absorber thin film.

2.4.1 Nanoparticle synthesis with different [I]/[IV] ratio

All the nanoparticles are synthesized with the same method as described before. The only difference is [Ag+Cu]/[Sn] ratio was set to be 2.0, 1.9, 1.8, 1.7, 1.6 and 1.5, separately, by controlling the amount of Ag(acac), Cu(acac) and $Sn(acac)_2 \bullet Cl_2$ dissolved in OLA before the injection.

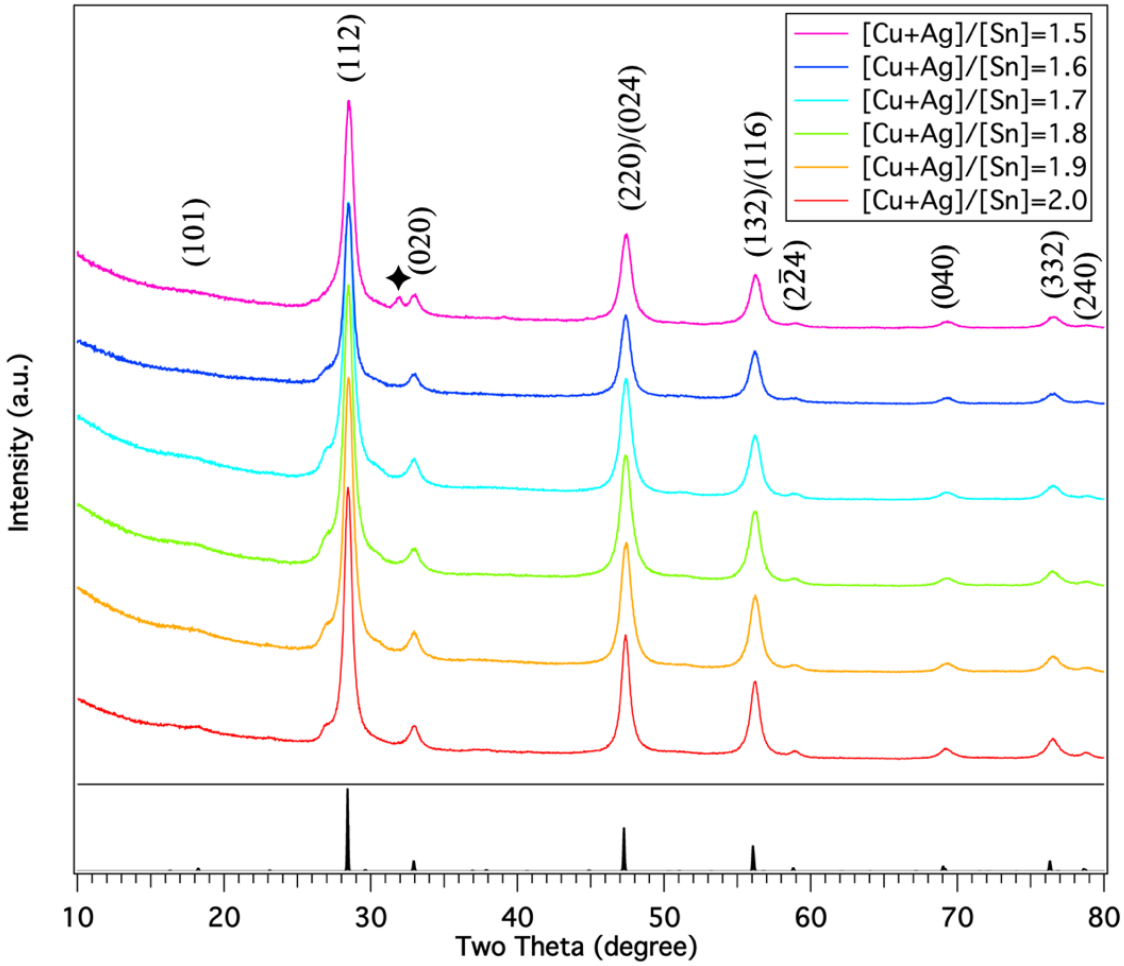

Figure 2.14 XRD of 5% Ag-alloyed CZTS nanoparticles with different [Ag+Cu]/[Sn] ratio compared with standard kesterite CZTS (JCPDS 26-0275)

Although the ratio between I and IV cations was changed from stoichiometry (2.0) to 1.5, the XRD of as-synthesized nanoparticles was the same except for the one with [Cu+Ag]/[Sn]=1.5, as shown in Figure 2.14. When the [Cu+Ag]/[Sn]=1.5, an extra peak at ~32° exists, which does not belong to CZTS. This peak probably corresponding to the (002) peak from $Cu_{1.8}S$ (Space group $Fm\bar{3}m$, ICSD-57213). However, due to the Cu-poor condition, if $Cu_{1.8}S$ exists as one of the secondary phases, there had to be a Zn or Sn related compound to balance the mass.

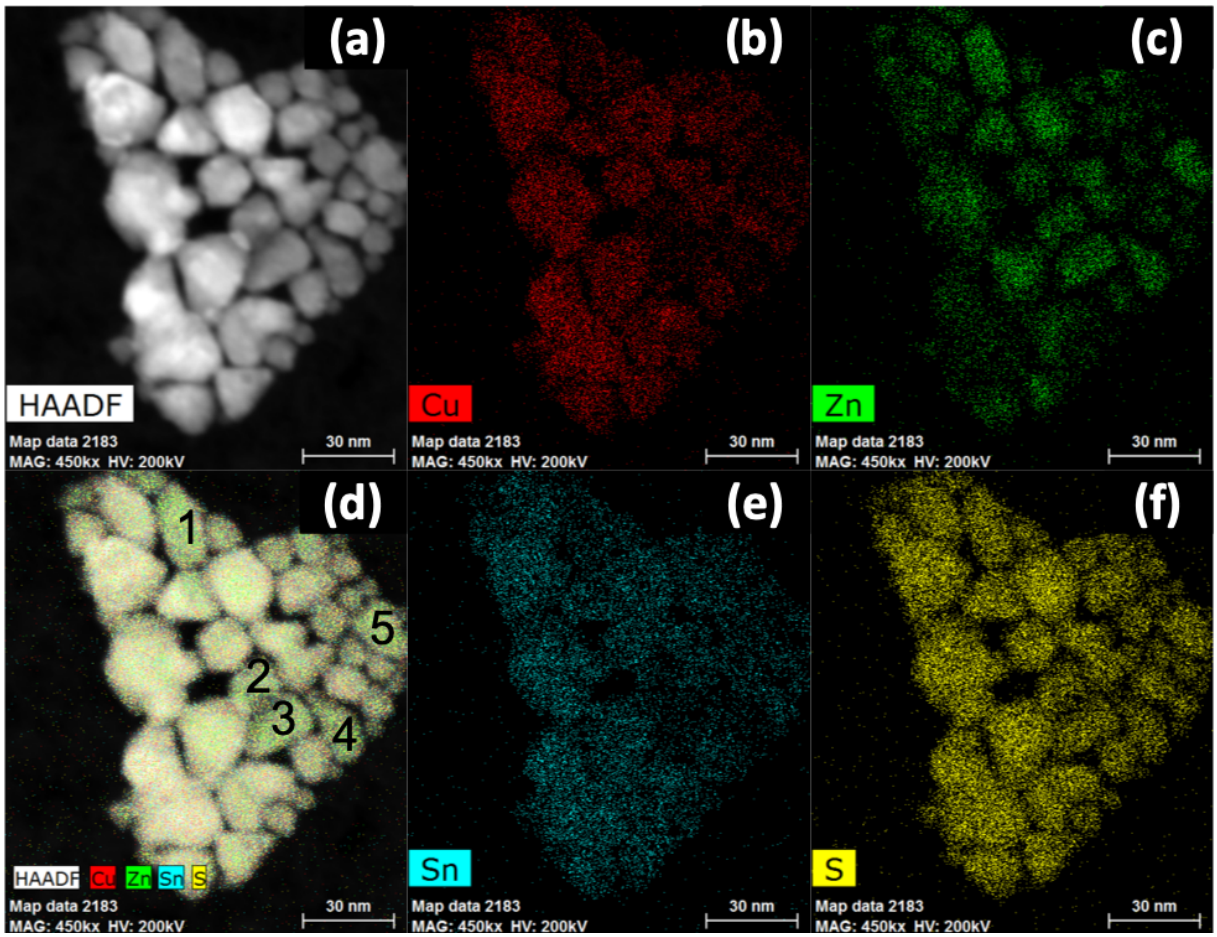

Figure 2.15 (a) STEM image of $(Cu_{0.95}Ag_{0.05})_{1.5}Zn_{1.05}SnS_4$ nanoparticles and elemental distribution of (b) Cu, (c) Zn, (e) Sn, (f) S and the (d) overlapped elemental distribution

To examine secondary phase(s) other than $Cu_{1.8}S$, STEM-EDS were conducted on those nanoparticles, as shown in Figure 2.15. From the elemental distribution, besides the intra-particle inhomogeneity, there was a significant difference between Cu and Zn from particle to particle. For example, as labelled in Figure 2.15(d), grain 1-5 had higher Zn and S mostly, while Cu and Sn signals were relatively weak. This indicated that there were ZnS along with CZTS nanoparticles. However, because of the overlap of XRD patterns between zinc-blend ZnS (ISCD-77090) and CZTS, the XRD pattern was not able to identify the existence of ZnS. Thus, it can be concluded that when [Cu+Ag]/[Sn]=1.5, ZnS and $Cu_{1.8}S$ co-existed along with CZTS nanoparticles.

2.4.2 ACZTSSe thin films with different [Cu+Ag]/[Sn] ratio

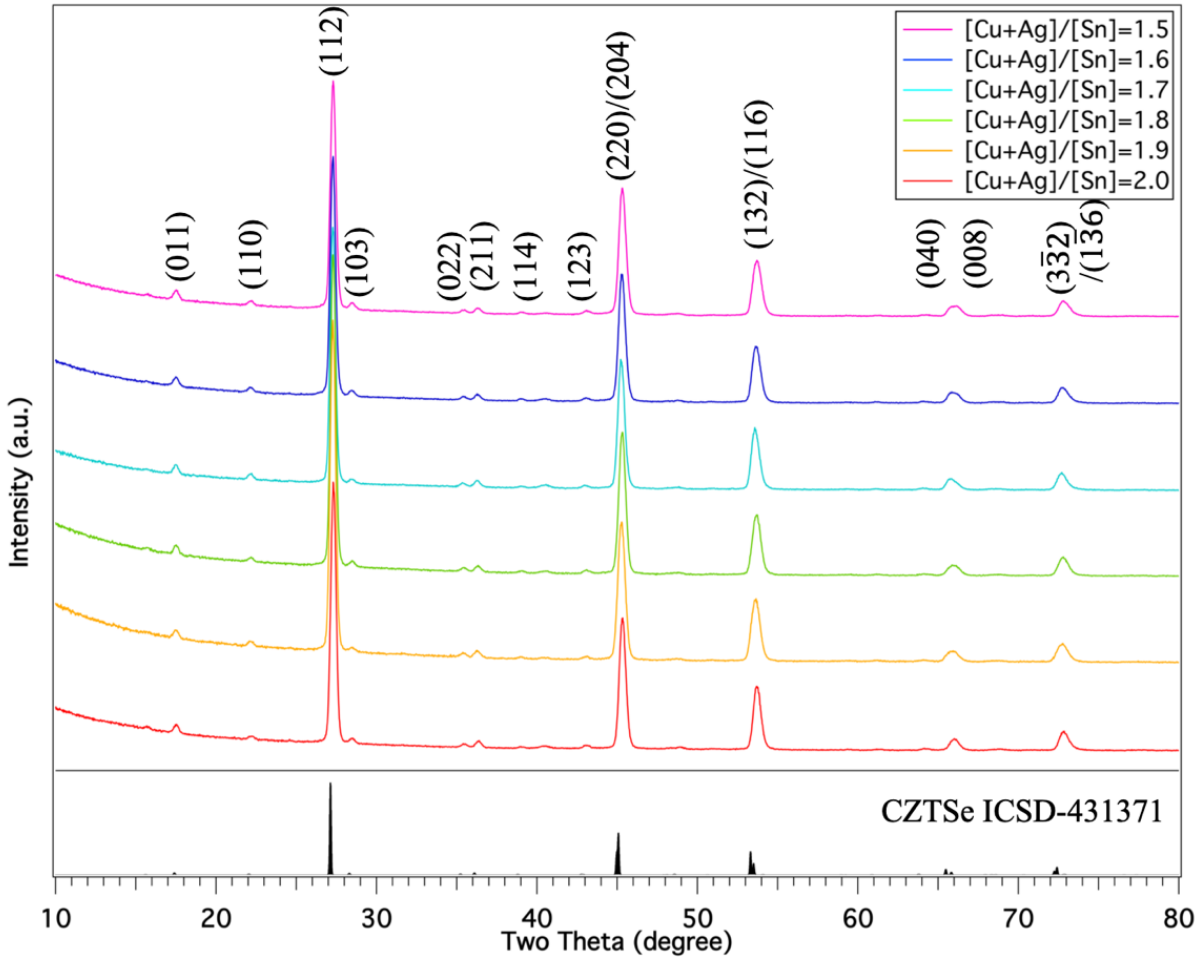

Figure 2.16 XRD patterns of 5% Ag-alloyed CZTSSe thin films with different [Cu+Ag]/[Sn] ratio

Since ZnSe has a slightly right-shifted XRD pattern from CZTSe, it is possible to distinguish ZnSe from CZTSe. Based on the XRD patters of the 5% Ag-alloyed CZTSSe films, there were no secondary phase(s), such as $Cu_{1.8}Se$ or ZnSe, that came from the impurities in the nanoparticles. This is conceivable considering the top-down process during the selenization. Different cations dissolved in selenium and precipitated out as CZTSe grains. Although there were $Cu_{1.8}S$ and ZnS nanoparticles in the precursor film, they would have been dissolved during selenization and acted as just cation sources. However, the different starting cation ratio still played a role in the final

film. First of all, although $Cu_{1.8}S$ and ZnS were dissolved, it still left local composition non-uniformity, resulting in local band gap fluctuation. Secondly, the different starting concentrations of cations created different chemical potentials for the cations. Although CZTSe precipitated from the selenium solution, these different chemical potentials resulted in different defect formation and changed the optoelectronic properties of the final film. The composition in the selenide film is plotted as a function of the precursor composition as shown in Figure 2.17.

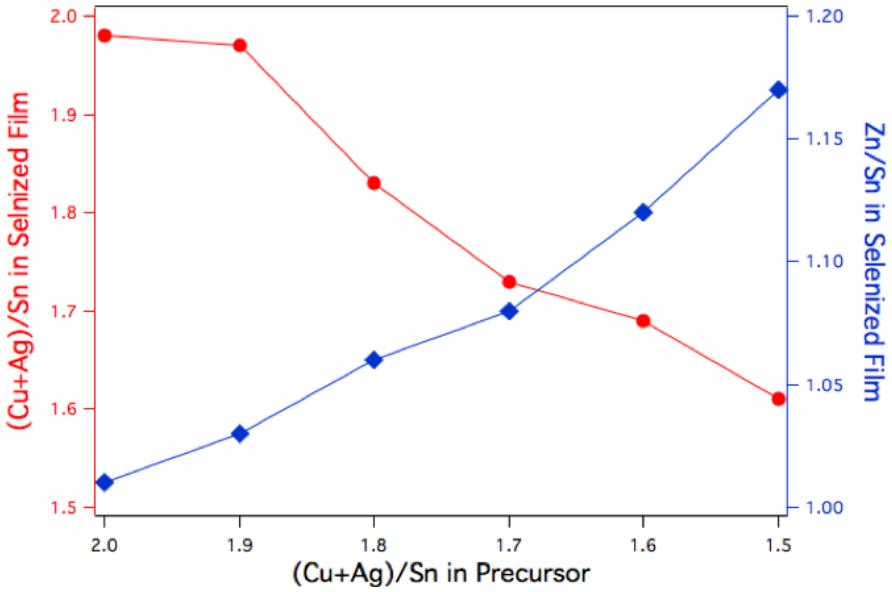

Figure 2.17 Cation ratio in the selenide films as a function of [Cu+Ag]/[Sn] in precursor

The [Cu+Ag]/[Sn] ratio in the selenized films had a positive correlation to that in the precursor. Interestingly, although the [Zn]/[Sn] ratio was the same for all the precursors, the final films showed different [Zn]/[Sn], with a significant correlation to the ratio between [Cu+Ag] and [Sn]. When [Cu+Ag] started low, it ended up with high [Zn]. This agrees with the defect formation in CZTSSe [43], where V_{Cu} and Zn_{Cu} always form together as defect pairs. When Cu is deficient, it lowers the formation energy of V_{Cu}. As a result, Zn_{Cu} forms along with V_{Cu} and gives higher Zn concentration. This also demonstrates that CZTSSe is a very forgiving material. Due to the similar

size of all the cations, when one of them is deficient, the relatively small strain in the lattice always allows other cations to sit in those positions, especially for Cu and Zn. However, the sequential defect formation may change the carrier behavior significantly, which affects the final photovoltaic device performance.

2.4.3 Carrier lifetime for ACZTSSe thin films solar cells with different [Cu+Ag]/[Sn] ratio

The carrier lifetime was measured by time-resolved photoluminescence (TRPL) and a single exponential decay model is used to fit the characteristic lifetime of minority carriers:

$$I = A_0 + B_0 \exp\left(-\frac{t}{\tau}\right) \qquad 2.3$$

where I is the measured photon intensity, A_0 is the baseline intensity, B_0 is the pre-exponential constant, t is the time and τ is the minority carrier life time. The TRPL spectrum is shown in Figure 2.18.

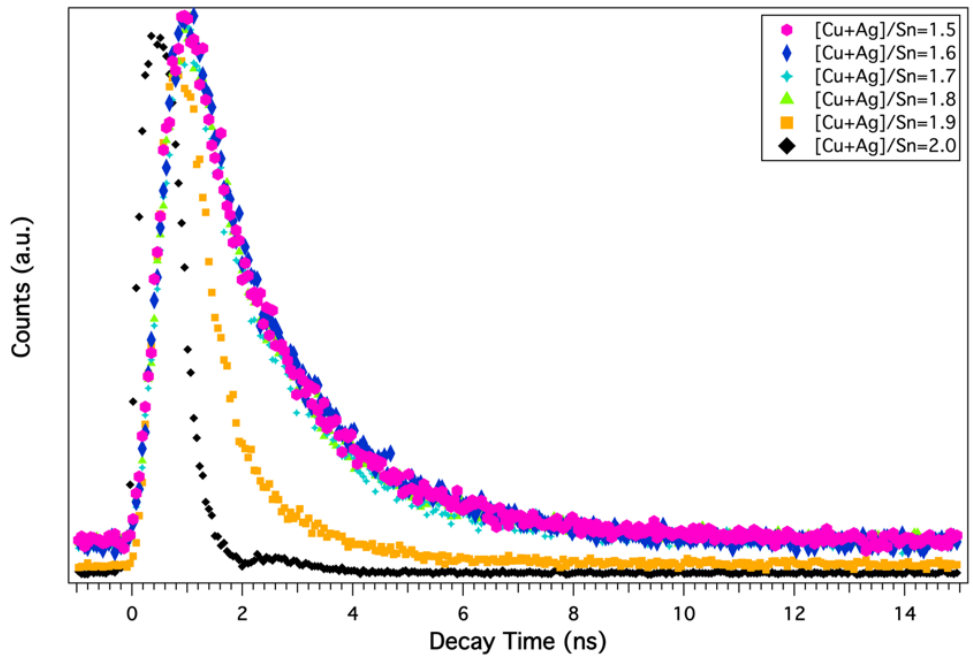

Figure 2.18 TRPL data for ACZTSSe films with different stoichiometry

From the plot, when [Cu+Ag]/[Sn]=2.0 or 1.9, the carrier lifetime was significantly shorter than the other cases, especially for [Cu+Ag]/[Sn]=2.0. However, for 1.5<$\frac{[Cu+Ag]}{[Sn]}$<1.9, the decay curves almost overlapped with each other. The fitted carrier lifetime, as well as the photovoltaic performance of these thin film solar cells, are list in Table 2-4.

Table 2-4 PCE performance as a function of [I]/[IV]

Precursor composition	[I]/[IV]=2.0	[I]/[IV]=1.9	[I]/[IV]=1.8	[I]/[IV]=1.7	[I]/[IV]=1.6
Carrier lifetime (ns)	<0.1	0.9	2.1	2.2	2.2
PCE (%)	0.03	5.8	6.3	7.2	4.8
V_{oc} (V)	0.03	0.38	0.36	0.4	0.37
J_{sc} (mA)	3.9	27.3	31.4	30	27
Fill factor (%)	22	57.5	56.8	60.7	48.5

When [I]/[IV] was 1.7, the solar cell had its highest efficiency, which is close to the optimized [I]/[IV] ratio CZTSSe without Ag doping or alloying [21], [60]. The J-V curve of [I]/[IV]=1.9 and [I]/[IV]=1.6 (shown in Figure 2.19) are used as examples to analyze their loss mechanism. When [I]/[IV]=1.9, the *Voc* is comparable with the champion nanoparticle ink based CZTSSe devices, and *Jsc* is about ~15% less, partially because of the lack of anti-reflective layer. The major difference is from the fill factor. This low fill factor was mostly due to the low shunting resistance. For high-performance thin film solar cells, the shunting resistance should be at the scale of k-ohm/cm^2, while for this one, it is only 420 ohm/cm^2. In the case of high [I]/[IV] ratio, the shunting of the device is expected. Tanaka *et al.* pointed out that, when [I]/[IV+II]>0.9, Cu_2Se is formed

[70]. Cu_2Se is a semi-metallic material with very high hole concentration and mobility, creating a shunting path in the absorber layer. Combined with the short carrier life time of this film, the existence of Cu_2Se embedded in CZTSSe grains is highly possible. When [I]/[IV]=1.6, the fill factor was even lower. There are two major losses in the fill factor: high series resistance and high ideality factor. With low [I]/[IV], ZnS, which is almost an insulator, may form locally and increase the series resistance [71], [72] in the absorber layer. The ideality factor here is significantly larger than 2, implying high density defect states at the interface of p-n junction [73].

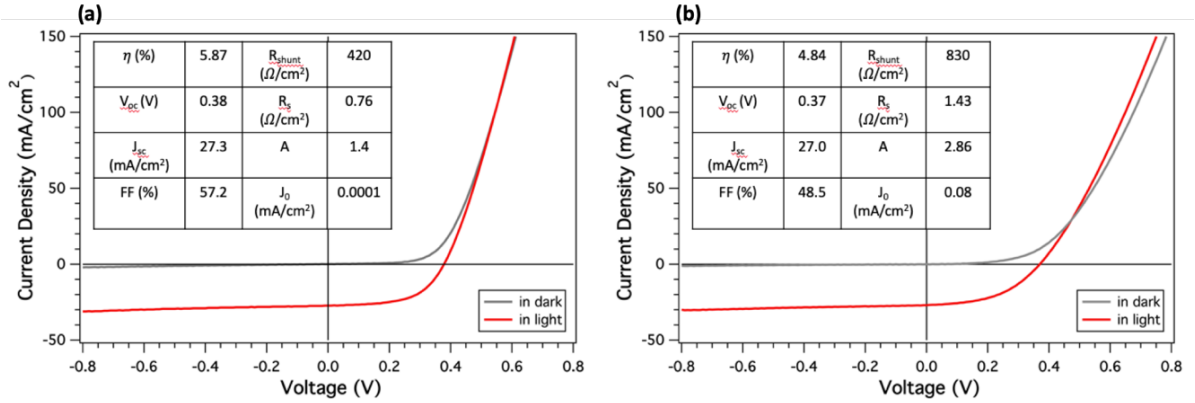

Figure 2.19 J-V performance of thin film solar cells with absorber composition of (a) [I]/[IV]=1.9 and (b) [I]/[IV]=1.6

In conclusion, due to the dissolution-precipitation process during selenization, it is very difficult to make sure that the precipitated large grain layer has the same composition as the starting nanoparticles. However, with the off-stoichiometry composition, secondary phase(s) may form to balance the mass, although the amount is too small to be picked up in XRD or Raman. These secondary phase(s) play an important role in the I-V performance of the solar cell, affecting the shunt resistance, series resistance, and the defect states of the absorber material. An optimized

composition of $1.7 < \frac{[I]}{[IV]} < 1.8$ is desired for 5% Ag-alloyed CZTSSe thin films to minimize the formation of this secondary phase(s) and achieve high efficiencies.

2.5 Conclusion

This chapter describes Ag-alloyed CZTSSe thin film deposition through nanoparticle ink route. CZTS nanoparticles with different Ag concentrations have been synthesized. There are two distinguishing characteristics for the nanoparticles after Ag-alloying: (1) Ag-rich particles are attached to CZTS nanoparticles, which may correspond to amorphous Ag or AgS. (2) When more than 30% Ag is added into the system, the nanoparticles start to show phase separation. ZnS nanocrystals and SnS_2 sheets are formed along with CZTS nanoparticles.

However, all these secondary phases can be digested after selenization. After selenization, no secondary phase(s) was detected from either XRD or Raman. Ag was incorporated into the large CZTSSe grains, confirmed by the expansion of lattice parameter with increased Ag concentration. Besides, Ag-alloying helps to form large and flat grains as well as more thorough sulfur depletion, both of which are preferable for high performance thin film photovoltaic devices.

Finally, the optimization of [I]/[IV] ratio for 5% Ag-alloyed CZTSSe thin films was explored. With the [I]/[IV] ratio changed from 1.5 to 2.0, no detectable secondary phase(s) were found for the sulfide nanoparticles. The optoelectronic properties were severely affected by the stoichiometry, as well as the I-V performance. The [I]/[IV] ratio of 1.7-1.8 is preferred to avoid the formation of ZnS or Cu_2Se, which changed the resistance as well as the recombination behavior significantly in the absorber layer.

3. SYNTHESIS OF SILVER ZINC TIN SULFIDE NANOPARTICLES AND EXPLORATION FOR THEIR FORMATION PATHWAY

3.1 Introduction and background

As demonstrated in the previous chapter, silver zinc tin sulfide (Ag_2ZnSnS_4, AZTS) has preffered defect chemistry compared with CZTS, due to the high formation energy of I-II anti-site defects [51], [58]. AZTS is also a semiconducting material with high light absorption coefficient with a band gap width of about 2 eV.

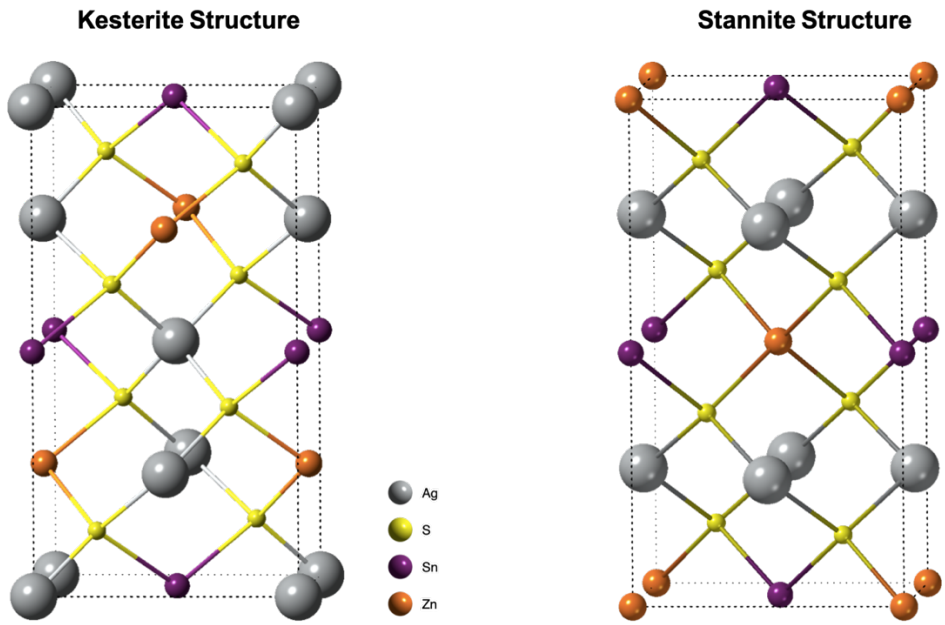

Figure 3.1 Kesterite and Stannite AZTS crystal structure

There are two crystal structures of AZTS. One is kesterite and the other is stannite. These two structures are quite similar that the Sn and S atoms are almost at the same locations. In kesterite ($I\bar{4}$), they are slightly less ordered than stannite ($I\bar{4}2m$), since in stannite, the z=1/4 and z=3/4 plane are occupied by only Ag atoms, while in kesterite structure, Ag and Zn are in the same plane

alternately. Due to the similarity in crystal structure, the x-ray diffraction patterns of these two are similar with each other, especially the main peak positions, as shown in Figure 3.2. Only a few relatively weak peaks have different intensity or a minor peak shift. Limited by the resolution and intensity of the X-ray diffractometer, we are unable to tell the difference between kesterite and stannite structure of AZTS at this point. Based on the calculation, most researchers concluded that kesterite AZTS has lower formation energy than stannite AZTS [51], [65]. As a result, in this chapter, only the crystallography information from kesterite structure will be used as a future reference.

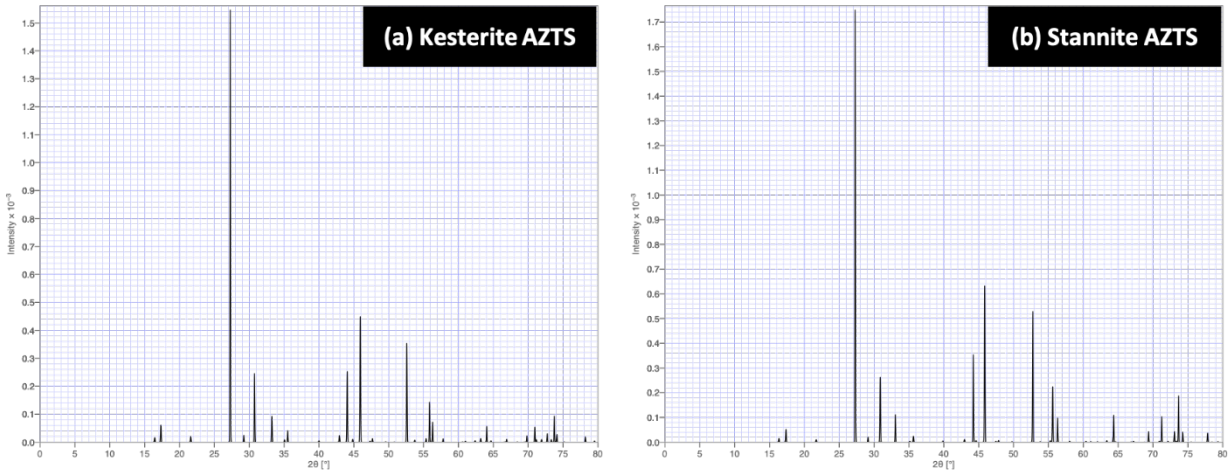

Figure 3.2 Standard XRD for AZTS (a) Kesterite, simulated from Crystal Maker based on the lattice parameter from Gong *et al.* [65]; (b) Stannite, ICSD #605734

Since 2010, attention has been paid to AZTS as a novel semiconducting materials [74]. It has been used for H_2 production in the form of either particles or thin films [75]. Li *et al.* have synthesized AZTS particles from aqueous phase with diameter of 100-200 nm [76]. The as-annealed AZTS particles had a H_2 production rate of 580 μmol/h with 1% Pt loading. Cheng *et al.* deposited AZTS films by sulfurization of co-sputtered Ag-Zn-Sn precursors [77]. The sample resistivity was tuned by changing the cation ratios and 0.31mA/cm^2 photoelectrochemical current density was achieved

at the optimized composition. The possibility of photovoltaic application of this material has been explored as well. For example, AZTS films were deposited by sputtering and followed sulfurization in H_2S. By different sputtering sequence and thickness, either n-type or p-type AZTS thin films were obtained. These films were assembled into a photovoltaic device and 0.87% and 1.38% efficiencies were achieved as homojunction and heterojunction solar cells , separately [78], [79].

Despite all these application of AZTS, the particle they synthesized or the film they deposited always have binary or ternary phases as impurities, such as ZnS, SnS_2 or Ag_8SnS_6 [74], [77], [79]. As semiconductors, the impurities not only behave as fluctuation spots on the optoelectronic properties of AZTS, but also have a negative influence on the characterization of this material. Here, an oleylamine based AZTS nanoparticle synthesis route is demonstrated. Also, how the particle phase(s), size, morphology are evolved in the solution with reaction time is presented to reveal the evolution path for AZTS nanoparticles.

3.2 Experiment

3.2.1 Materials

Silver acetylacetonate (98%, Sigma-Aldrich) was stored at 4°C under N_2 atmosphere when not in use. Zinc acetylacetonate hydrate (99.995% trace metals basis, Sigma-Aldrich) and tin (IV) bis-(acetylacetonate) dichloride (98%, Sigma-Aldrich) were stored at room temperature in a N_2 atmosphere. Oleylamine (OLA) (>98%, Sigma-Aldrich) was degassed by three freeze-pump-thaw cycles prior to use. Methanol (99.9%, Fisher), 2-isopropanol (>99.9%, Fisher) and hexane (99% pure, mixture of isomers, Fisher) were used as received to wash nanoparticles. Potassium sulfate

(K_2SO_4, >99.0%, Sigma Aldrich) was used as the electrolyte in aqueous solution for photoelectrochemical measurements.

3.2.2 Nanoparticle synthesis and washing

Typically, 0.6 mmol silver acetylacetonate, 0.33 mmol zinc acetylacetonate hydrate and 0.33 mmol tin (IV) bis-(acetylacetonate) dichloride were dissolved in 8mL OLA under N_2 atmosphere at 65°C (m-OLA). In addition, 6 mmol S was dissolved separately in 6 ml OLA under N_2 at 65°C (s-OLA). To start the reaction, 12 mL OLA was added into a 100-mL three-neck flask and stirred at 300 rpm. The OLA was heated to 35°C and purged with argon 3 times. The solution was then heated to 135°C for a second 3-cycle purging to remove the gases and light impurities. The OLA was then heated to 250°C. When OLA reached 250°C, 4.5 mL s-OLA solution was injected through a syringe quickly. After 10 s, 6 mL m-OLA was quickly injected into the system. The reaction was kept at 250°C with continuous stirring under argon atmosphere.

Aliquots (2 mL) were taken at 10 min, 15 min and 60 min of reaction time and quenched into 10 mL of IPA. These aliquots were centrifuged at 14000 rpm to extract the nanoparticles. Three hours after injection, the reactant flask was removed from the heating mantle and cooled to 50°C with blowing N_2 outside the reaction flask. When the reactant reached room temperature, it was then pipetted out into a Teflon coated centrifuge tube and mixed with equal volume of IPA. The mixture was centrifuged at 14000 rpm for 5min. After the first centrifuging, the precipitant pellet was recovered and dispersed in 3mL hexane. After the precipitant was fully dispersed in hexane, ~18 mL mixture of 70% IPA and 30% methanol is added into the centrifuge tube and centrifuged at 1000 rpm for 5 min. The precipitant was discarded and the supernatant is saved. The nanoparticle containing supernatant was then centrifuged at 16000 rpm for 5min to collect the nanoparticles as

a precipitate. These nanoparticles were re-dispersed in 3mL hexane with subsequent addition of 18mL of IPA and methanol mixture (with 7:3 volume ratio). The nanoparticles were recollected as precipitant pellet by centrifuging at 16000rpm for 5min and discarding the upper layer liquid. This procedure of hexane-dispersion followed with alcohol washing was repeated 3 times in total, as is typically done for CZTS nanoparticle. The final precipitant was dried under Ar flow at ~2 lpm for about 25 min and then sealed in a container under N_2 atmosphere.

3.2.3 Film deposition

The synthesized nanoparticles (3-hour reaction time) were dispersed into hexanethiol at the concentration of 300 mg/mL to form a nanoparticle ink. This ink was doctor bladed onto molybdenum-coated (800nm) soda-lime glass or fluorine-doped tin oxide (**FTO**) coated glass (~13Ω/sq surface resistivity). The as-purchased FTO glass was rinsed by IPA, methanol, and then ultrasonically cleaned in Alconox detergent solution followed by ultrapure water wash prior to usage. Each time, 15 µl ink was pipetted out for ~2.5x5 cm^2 coating area. The coated film was dried for 4 minutes at room temperature and then annealed at 300°C for 1 min in air. Each substrate was coated and annealed twice.

3.2.4 Characterization

For characterization by X-ray diffraction (XRD, Rigaku SmartLab diffractometer), the nanoparticle films were prepared by drop casting nanoparticle ink on soda-lime glass. The morphologies and crystal structures of the sulfide nanoparticles were measured using transmission electron microscopy (TEM, FEI Talos) with a 200kV electron beam. For TEM sample preparation, the nanoparticle inks were diluted with toluene at about 1:1000 volume ratio and ultra-sonicated for 15min prior to deposition. The suspension was drop cast onto an ultrathin carbon-on-carbon lacey support film (gold grid, 400 mesh, Ted Pella) for (HR)TEM, or on a silicon nitride 5 nm

thick TEM window (9 small windows, SIMPore Inc.) for STEM/EDS. The absorbance of AZTS nanoparticles was measured by a PerkinElmer Lambda 950 spectrophotometer through an AZTS nanoparticle ink coated FTO glass sample. Surface-enhanced Raman Spectra (**SERS**) were acquired by HORIBA Jobin Yvon LabRam HR800 with an excitation laser wavelength of 633nm. The nanoparticle samples for SERS measurement were drop cast on Au substrates (50 nm thick, thermally evaporated on Mo glass) at the concentration of 4 mg/ml in hexane dispersion.

3.3 Result and Discussion

X-ray powder diffraction (as shown in Figure 3.3) and TEM were used to characterize the phase purity of the as-fabricated AZTS nanoparticles as a function of reaction time. For reaction times shorter than 180 minutes, ZnS was detected by both XRD and as rod-shaped particles distinctly different from the AZTS nanoparticles. It was not possible to determine whether the AZTS nanoparticles were stannite AZTS phase (space group $I\bar{4}3m$, ICSD #605734) or kesterite (space group $I\bar{4}$, as simulated using CrystalMaker using the lattice parameters reported by Gong *et al*). The diffraction peak positions and intensities are similar for the two phases. Note than Gong *et al.* [65] and Gautam *et al*. [51] have separately proposed that kesterite structure (space group $I\bar{4}$) is more stable for AZTS than stannite. In previous studies, ZnS and Ag_8SnS_6 were commonly found as secondary phases in as-fabricated AZTS nanoparticles or thin films. [75], [77], [80] No significant peaks corresponding to these secondary phases were observed by XRD or TEM for reactions times greater than or equal to 180 minutes. This situation is in contrast with characterization of phase content in CZTS nanoparticle synthesis, where some of the major peaks of CZTS overlap with Cu_2SnS_3 or ZnS. The peaks from AZTS nanoparticles were clearly distinguishable from zincblende zinc sulfide (space group $F\bar{4}3m$, ICSD #77090) and Ag_8SnS_6 (space group $F\bar{4}3m$, ICSD #605727).

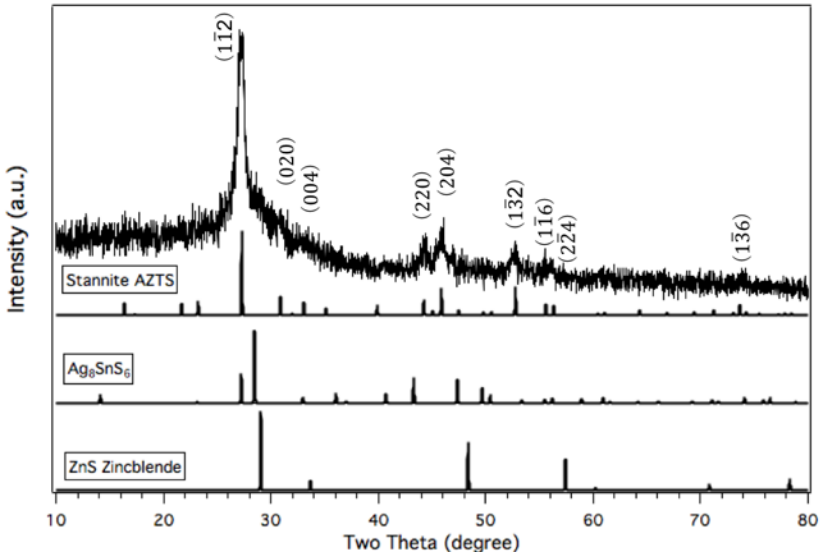

Figure 3.3 X-ray diffraction pattern of nanoparticles collected from a 180-minute reaction time and compared with standard stannite Ag_2ZnSnS_4 (ICSD #605734), zincblend ZnS (ICSD #77090) and Ag_8SnS_6 (ICSD #605727)

Hot-injection of S-OLA and M-OLA solutions at 250 °C was used to bypass temperatures that were favorable for the formation of binary and ternary phases. Compared to the precursor concentrations used in the reported synthesis of CZTS nanoparticles [21], [34], precursor concentrations for AZTS synthesis were reduced to about 1/3 for two reasons: 1) at 65°C, the solubility of Ag, Zn and Sn precursors in OLA is lower than that of Cu, Zn and Sn precursors, and 2) at higher concentrations, Ag, Zn and Sn precursors provided a much more viscous solution, leading to poor mixing upon hot injection in the reaction medium and resulting in the formation of secondary phases. If secondary phases formed and grew, it became more difficult for the rest of free ions to form AZTS with the correct stoichiometric ratio. This is especially true for SnS_2, which tends to grow to a few hundreds of nanometers, or even micron-sized disks, quickly [81]. The starting precursor concentration is one of the key variables to suppress the nucleation and grain growth of the secondary phases.

To study the phase and composition evolution of the nanoparticles, TEM images were taken for nanoparticles collected at reaction time periods of 10 min, 15 min, 60 min and 180 min and are shown in Figure 3.4 (a-d) with corresponding size distributions in Figure 3.4 (e-h). Most of the 10-min nanoparticles were small, round nanoparticles with a diameter about 7 nm. After 15 min, two different shapes of nanostructures were observed: round particles and nanowires. STEM-EDS mapping (Figure 3.5) revealed that the round particles primarily contained Ag, Zn, Sn and S, whereas the nanowires were ZnS. After 60 min of reaction, nanowires were no longer observed, and the AZTS nanoparticles had grown to an average size of 19.2 nm and remained equiaxed. For the 180-min sample, the size of the AZTS nanoparticles had increased to about 23 nm and no ZnS particles were observed in STEM-EDS.

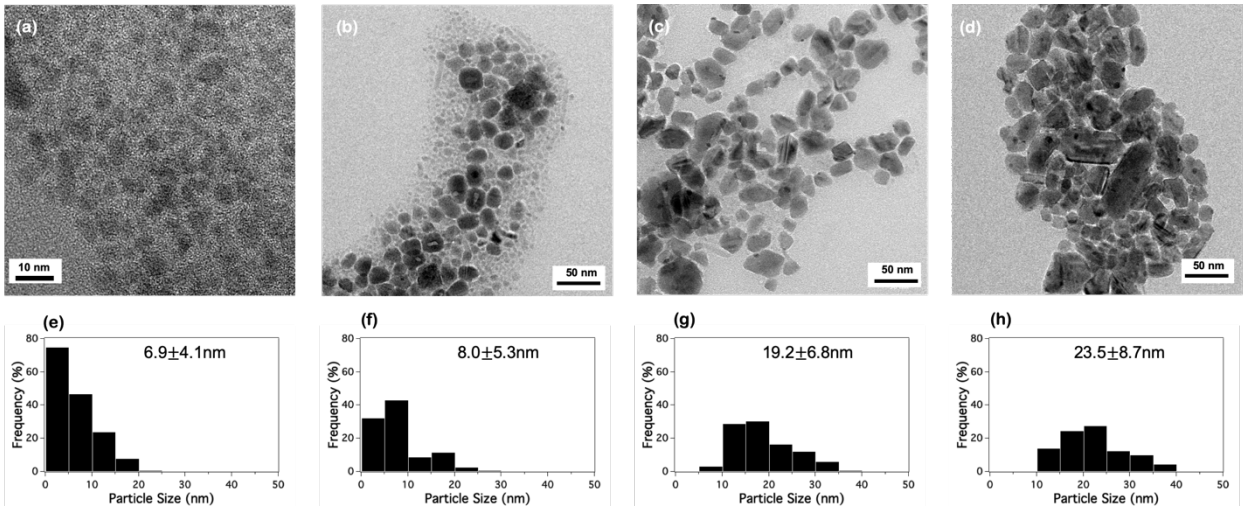

Figure 3.4 TEM images showing typical particle shapes, sizes and the corresponding size distributions for the collected AZTS nanoparticles at various reaction time periods: (a)& (e) 10 min, (b)& (f) 15 min, (c)& (g) 60 min and (d)& (h)180 min.

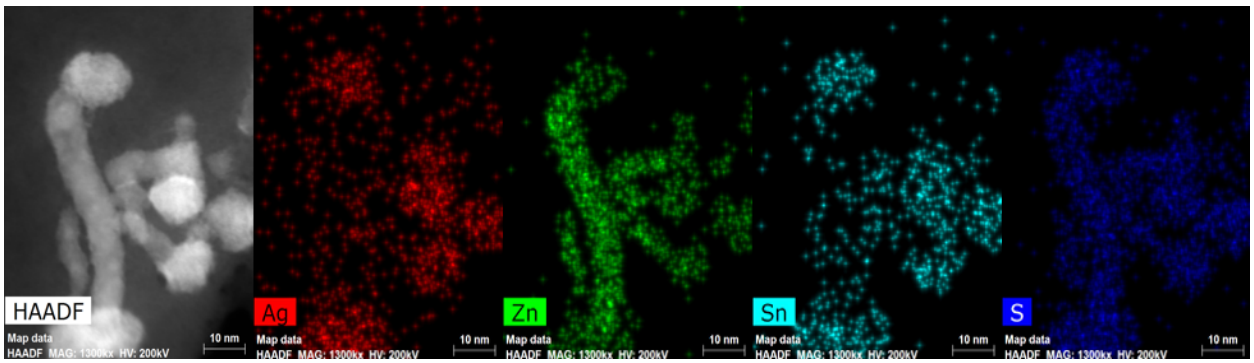

Figure 3.5 Energy dispersive x-ray spectroscopy elemental mapping from scanning transmission electron microscopy for 15min nanoparticles

The microstructure and composition profiles of the individual 180-min AZTS nanoparticles were examined by HRTEM/STEM-EDS. The HRTEM image in Figure 3.6 (a) shows a single crystal AZTS nanoparticle with a d-spacing = 0.32nm, corresponding to the (112) plane. The distributions of Ag, Zn, Sn and S within an individual nanoparticle are presented in Figure 3.6 (c). The EDS line scan across the nanoparticle shows that Ag, Sn and S profiles were uniform inside the particle while Zn was more variable. This is likely because Zn is incorporated into the particle at a later stage as the ZnS nanowires disappeared.

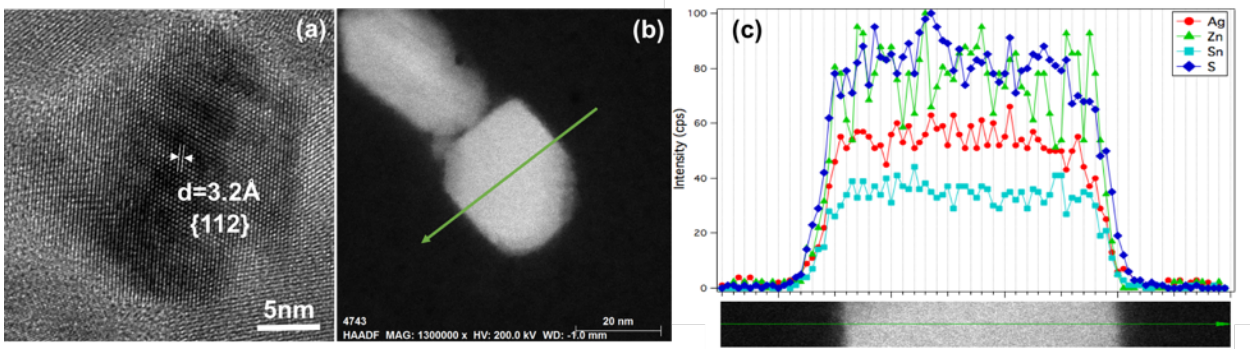

Figure 3.6 HRTEM image of an AZTS nanoparticle; (b) STEM high angle annular dark-filed image of AZTS nanoparticle; (c) STEM-EDS line-scans for nanoparticles showing the intensity profiles of Ag, Zn, Sn and S

When the nanoparticles are at an initial stage of formation, i.e., the diameters of the nanoparticles were less than 10 nm, it was very difficult to determine the phases and composition in STEM due to spatial resolution and signal intensity limitations. To explore the AZTS nanoparticle growth stages, Surface-Enhanced Raman Spectroscopy (**SERS**) was applied for the early stage synthesis as SERS shows stronger intensity and more details compared with conventional Raman spectroscopy [82]. Aliquots were withdrawn at 2 min, 5 min, 10 min, 60 min and 180 min, and their Raman spectra are shown in Figure 3.7, respectively. After 2 min of reaction, three major peaks were observed in SERS. The broad peak near 237cm^{-1} corresponds to silver tin sulfide (ATS) compounds, primarily Ag_8SnS_6 and $Ag_4Sn_3S_8$ [83]. Another small peak at 295 cm^{-1} corresponds to the AZTS phase. The strongest peak for 2 min, located at 353 cm^{-1}, corresponds to ZnS. After 5min, another AZTS peak appears at 382cm^{-1}. After 10 min of reaction, four peaks are observed corresponding to AZTS (270 cm^{-1}, 292 cm^{-1}, 348 cm^{-1} and 383 cm^{-1}), while the ZnS peak (354 cm^{-1}) and the ATS peak (235 cm^{-1}) remained significant. After 60 min reaction, the peak from AZTS phase (347 cm^{-1}) is further enhanced denoting higher crystallinity of AZTS. At the same time, the ATS peak (~236 cm^{-1}) disappears and the ZnS peak (354 cm^{-1}) is reduced to a small shoulder. Finally, after reaction for 180 min, the Raman peak for ZnS has disappeared and only AZTS peaks are observed, which indicates the phase purity of AZTS, in agreement with the TEM results.

SERS showed that the formation mechanism for the AZTS nanoparticles was quite different from that of CZTS reported in the prior studies [82]. In the CZTS case, $Cu_{2-x}S$ nucleates first, then Sn^{4+} and Zn^{2+} diffuse into $Cu_{2-x}S$ nanoparticles successively to form CZTS [82], [84]-[86]. There was a three-step-growth from $Cu_{2-x}S$ to Cu_3SnS_4 (CTS) then CZTS. However, in our case, no Ag_2S was observed from the SERS study of the early stage reaction. It was because the formation energy

for Ag_2S is much higher than $Cu_{2-x}S$ [87], so ZnS formation is the preferred precipitation reaction when cations are firstly injected and the temperature drops to a lower level (~205°C). According to the SERS analysis, when s-OLA and m-OLA are first injected, ZnS, ATS and AZTS all started to nucleate. As the temperature resumed back to 250 °C, AZTS nanoparticles were more thermodynamically preferred and grow larger with good crystallinity, while ZnS and ATS nanoparticles begin to decrease in size as reaction proceeds beyond 10 minutes and eventually disappeared completely.

Compared with previous research on AZTS nanoparticle synthesis [80], we eliminated the secondary phases: ZnS or Ag_8SnS_6. There are two major differences between previous work and our reaction. First, the sulfur sources were different. Sasamura et al. used ammonium N, N-diethyldithiocarbamate as the sulfur source, producing AZTS along with impurity phases [80]. Dodecanethiol (DDT) was previously used in some Ag-based semiconductor nanoparticles syntheses as both a solvent and a sulfur source, but elemental Ag formed instead of AZTS because of the strong reducibility by DDT [83]. This is very different from the CZTS case, in which only wurtzite CZTS nanoparticles are produced in the presence of DDT, the difference being probably due to the stronger oxidizability of Ag^+ compared with Cu^+ at elevated temperatures. [23], [57] In our work, elemental S dissolved in OLA was used, releasing high reactive H_2S during injection [88] and resulting in AZTS nanoparticles instead of elemental Ag [89], [90]. Second, the metal salts used previously are acetates which have weaker bonds between cations and anions compared with acetylacetonate salts used in our study. With zinc acetate, Zn^{2+} will be released more easily leading to the formation of ZnS [82], [90].

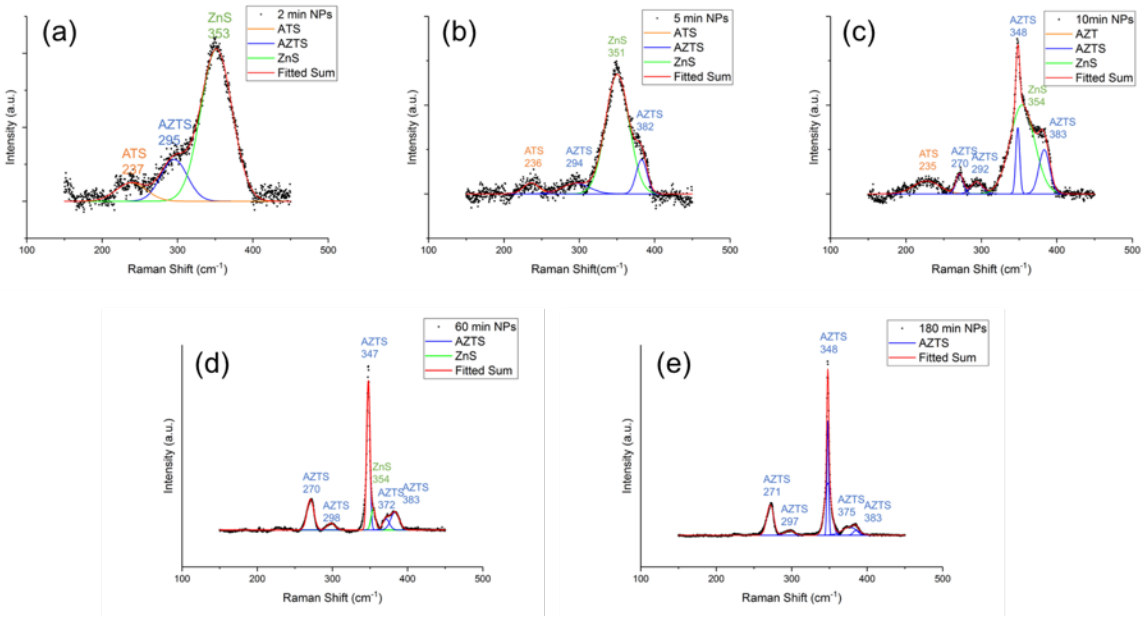

Figure 3.7 SERS spectra of nanoparticles extracted at (a)2 min, (b)5 min. (c)10 min, (d) 60 min and (e) 180 min

Optical properties of these AZTS nanoparticles were examined using UV-vis measurements. The optical band gap value is extracted from Tauc plot, assuming:

$$\alpha \propto (E - E_g)^n$$

in which α is the absorbance, E is the incident photo energy and E_g is the band gap. For a direct band gap material, n=1/2. As shown in Figure 3.8, the observed band gap was 2.16 eV, higher than the band gap (2.0 eV) of AZTS bulk material [75].

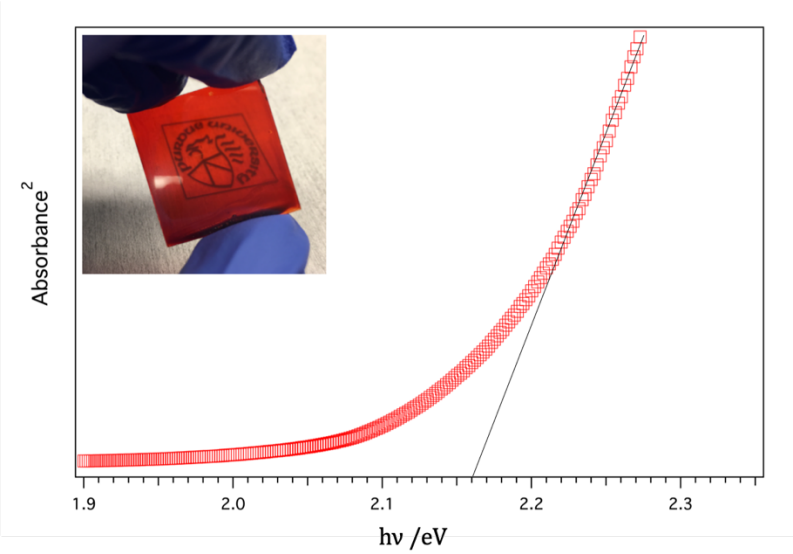

Figure 3.8 UV-vis spectroscopy of as annealed AZTS thin film. The picture on the upper left corner is the coated film on Purdue logo.

Considering the wide band gap of AZTS, researchers are working to realize the potential of AZTS as a photocatalyst for H_2 production. [76], [77] Photoelectrochemical (**PEC**) measurements were conducted to investigate the potential of AZTS nanoparticle films for photocurrent generation in 0.1M K_2SO_4 aqueous solution. A three-electrode system was used to measure the photon response of nanoparticle films over a range of -0.2 V~ 1.0 V versus the Ag/AgCl reference electrode (Fig. 3.9) with manual chopping every 0.05V. The photocurrent density increases with applied voltage up to ~100μA/cm^2, demonstrating that the AZTS nanoparticles were n-type semiconductors [80], [91]. Compared with the previous AZTS thin films made by PVD [77], the limited current density may have resulted from the surface states of the nano-sized particles and the grain boundaries. Some kinetic instability of the photocurrent was observed in the first second when the light was switched on. Better performance of AZTS film is expected due to its desirable band gap and high crystallinity, that can be achieved by optimization of back-contact material and the grain size in the film.

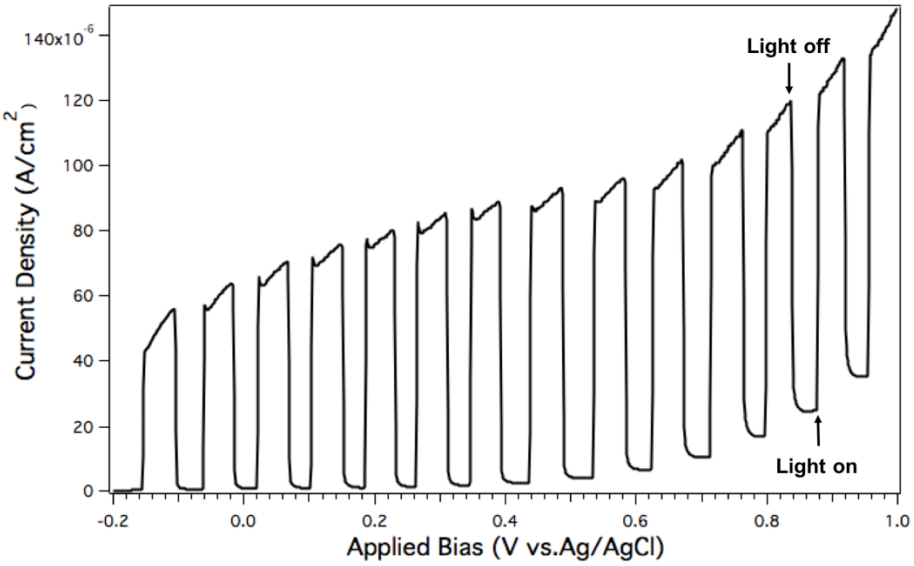

Figure 3.9 Photocurrent vs. Applied bias (relative to Ag/ AgCl electrode) curve of AZTS nanoparticles coated on FTO glass

3.4 Conclusion

In summary, semiconductor nanoparticles of AZTS have been successfully synthesized through a solvo-thermal process. The hot-injection reaction allowed scalable production of AZTS nanoparticles with uniform composition. Based on the analysis of the intermediate products formed at different reaction stages, a formation mechanism for the AZTS nanoparticle formation is proposed and the similarities, as well as differences between CZTS and AZTS nanoparticle synthesis are compared in this work. It is expected that the solution-phase formation pathways of the AZTS revealed in this work will help with the future silver-based nanoparticle synthesis and device fabrication research. In terms of electronic properties, the AZTS nanoparticle film was found to have a band gap of 2.15 eV and the capability of generating a 100μA/cm^2 photocurrent at a bias of 0.8 V vs. Ag/AgCl in K_2SO_4 solution, showing its potential as a light absorber material

for photocurrent generation. Its application as a precursor for AZTSe absorber films is also under investigation and solution-processed AZTSe thin film solar cells are expected in the near future.

3.5 Supplemental Information

Figure 3.11 shows the STEM-EDS mapping of nanoparticles formed after 10 min reaction. The particles were small with non-uniform elemental distribution. Especially for Ag and Zn. Both inner- and intra-particle inhomogeneity were found among the particles in the view. After 60 min reaction, as shown in figure 3.12, most of the particles contained all of the four elements and no significant inhomogeneity inside the particles were found, except for the tiny particles at the bottom. The small particle still showed slightly Zn rich phase compared with others. After 180 min, particles with different sizes were examined and all four elements were found to be uniformly distributed among all the particles.

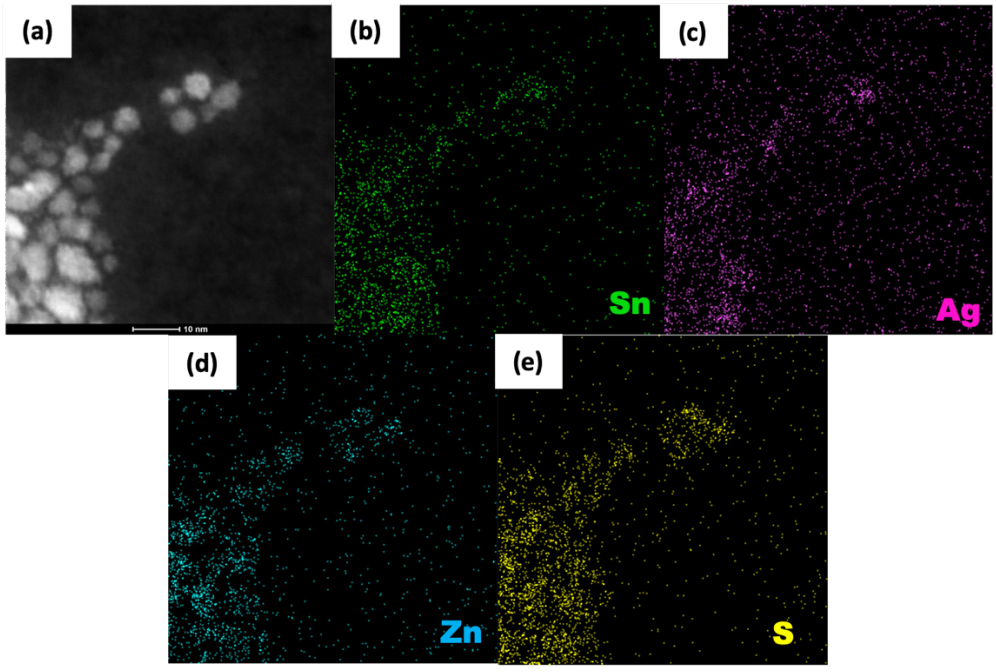

Figure 3.10 (a) HAADF image of 10 min nanoparticles and corresponding EDS mapping of (b) Sn, (c) Ag, (d) Zn and (e) S

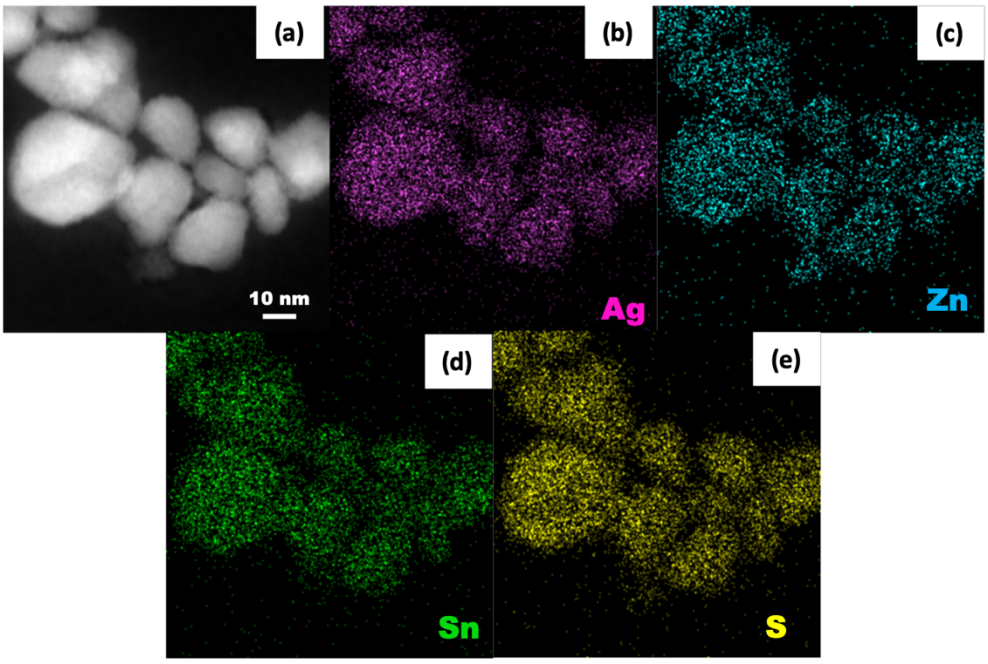

Figure 3.11 HAADF image of 60 min nanoparticles and corresponding EDS mapping of (b) Ag, (c) Zn, (d) Sn and (e) S; ZnS or Zn rich particles still exist as small particles

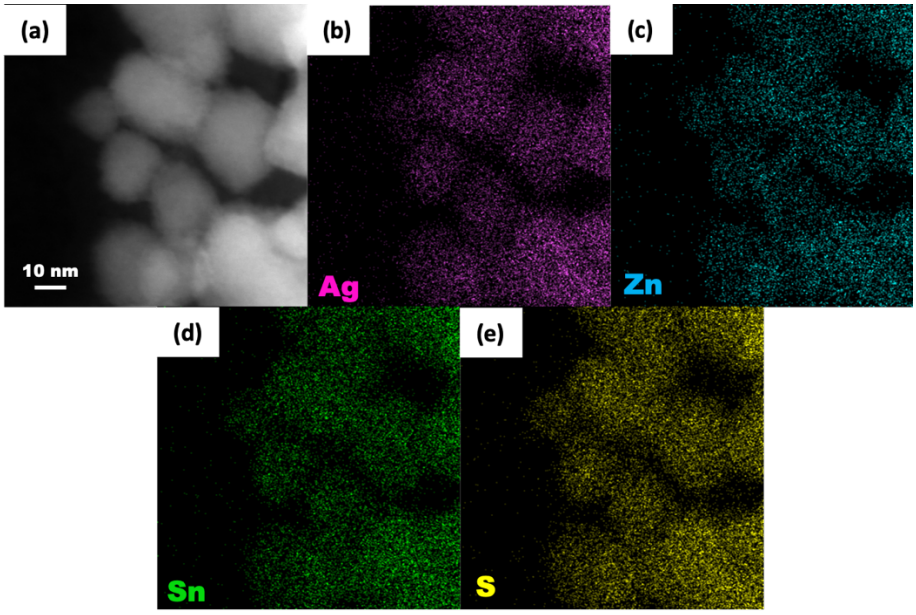

Figure 3.12 HAADF image of 180 min nanoparticles and corresponding EDS mapping of (b) Ag, (c) Zn, (d) Sn and (e) S. Uniform elemental distribution in all particles

From the STEM image area, the cation atomic ratio in nanoparticles are listed in the Table below:

Table 3-1 Atomic cation ratio of nanoparticles at different reaction stages

	10 min	60 min	180 min
Ag/Sn	0.34	2.04	1.99
Zn/Sn	0.90	1.07	1.20
Ag/(Zn+Sn)	0.18	0.98	0.90

4. INVESTIGATION INTO THE SELENIZATION CONDITIONS FOR SILVER ZINC TIN SELENIDE THIN FILMS FROM NANOPARTICLE-INK

4.1 Introduction and background

After CZTS solar cells achieved a maximum power conversion efficiency (PCE) of 12.6%, no further improvement has been demonstrated due to its intrinsic defects [19]. It has been established that the high densities of Cu_{Zn} or Zn_{Cu} anti-site defects limit the PCE of CZTS solar cells. These defects create trap states and dramatically decrease the open circuit voltage (V_{oc}) of devices [42], [92]-[94]. To eliminate these intrinsic defects, Ag turn out to be a promising candidate to replace Cu, having no overlap valence state with Zn^{2+} and more than 30% larger than Zn^{2+} [58], [95]. As one of the successful example, Gershon *et al*. developed photovoltaic devices based on an n-type $Ag_2ZnSnSe_4$ (AZTSe) absorber layer by co-evaporation and achieved higher than 5% PCE [96], suggesting the potential of this material as photovoltaic absorber.

AZTSe thin films have been typically obtained by vacuum deposition[65], [95], [97]; hence, a more cost-effective method is needed to enable large-scale fabrication of solar cells. In this chapter, how to convert colloidal nanocrystals into thin films with densely-packed large grains in selenium (Se) vapor (so-called selenization) at elevated temperature will be discussed. The phase purity and composition uniformity of this large grain layer, which is related to the selenization process, is essential for the optoelectronic properties of the final device [60], [98]. Therefore, the phase transformation, microstructure evolution, and composition change of large/fine grains have been widely explored in CZTS selenization process [59]-[62], [64], [99], [100]. By in-situ x-ray diffraction experiments, it was demonstrated that, during selenization of CZTS nanoparticles, Cu_{2-}

$_x$Se formed first, followed by Cu_2SnSe_3 and Zn incorporated last [61]. However, after adding Ag into the system, the selenization becomes different, which a fast grain growth rate and large grain size [35], [54]. Although solution-processed AZTSe or high-proportion silver alloyed ACZTSe thin films have been studied in some pieces of work[101], no work has been reported regarding how to fabricate AZTSe thin films with minimized pin-holes, which is essential for AZTSe as light absorb layers in highly performance photovoltaic devices [35], [102], [103].

In this chapter, the presented work is aiming to understand the selenization of AZTSe system as a comparison to CZTS. Key parameters in CZTS selenization, such as annealing temperature, KCN etching effect and Se vapor pressure, will be discussed with the utilization of rapid thermal processer (RTP). RTP gives precise and separate control of the temperature in the sample zone and selenium zone, which enables the control of Se condensation on top of the sample. A selenization mechanism is proposed based on the phenomenon we observed and the facts that have been summarized from CZTS case. Additionally, the interface engineering for AZTS with Cu deposition is studied to achieve better morphology, as well as adhesion between AZTS film and substrates. Ultimately, a strategy to obtain AZTS film consisting of continuous grains with uniform composition and fewer pin-holes is established, which can be beneficial for the future production of AZTS thin films.

4.2 Experiment

4.2.1 Materials

Silver acetylacetonate (98%, Sigma-Aldrich), zinc acetylacetonate hydrate (99.995% trace metal basis, Sigma-Aldrich) and tin (IV) bis-(acetylacetonate) dichloride (98%, Sigma-Aldrich) were

used as cation precursors. Sulfur (flakes, ≥99.99% trace metals basis) was used as an anion source.

Oleylamine (OLA, >98% Sigma-Aldrich) was degassed by three freeze-pump-thaw cycles and stored under N_2 atmosphere before usage. Methanol (99.9%, Fisher), 2-isopropanol (>99.9%, Fisher) and hexane (99% pure, mixture of isomers, Fisher) were used as-received for nanoparticle washing. Copper (Cu) pellets (99.99%, ¼'' Dia. x ¼'' Length, Kurt Lesker) were placed in a tungsten boat for thermal evaporation.

4.2.2 Nanoparticle synthesis

1.9 mmol silver acetylacetonate was dissolved in 4 mL OLA (Ag-OLA) in a round bottom flask. 1.05 mmol zinc acetylacetonate hydrate and 1mmol tin (IV) bis-(acetylacetonate) dichloride were dissolved together in 4 mL OLA (ZT-OLA) in another round bottom flask. 6 mmol of sulfur flakes were dissolved in 6 mL OLA (s-OLA) in a round bottom flask. All the dissolution was done under inert atmosphere and stirred at 65 ℃ on a heating mantle. The cation solutions were dissolved/ dispersed within 5 min and the sulfur dissolution took about 1 hr. 12 mL OLA was added into a 3-neck flask and connected to a Schlenk line. The OLA was purged with Ar at 35 ℃ and 135 ℃ 3 times for both temperatures. The OLA was heated to 250 ℃. Once the temperature reached this set point, 4.5 ml of s-OLA was injected into the 3-neck flask. After 20 s, 3 mL of Ag-OLA and 3 mL of ZT-OLA were injected into the 3-neck flask simultaneously. The reactant was kept at 250 ℃ with 300 rpm stirring. After 15 min, the reactant was removed from the heating mantle and cooled with blowing nitrogen outside the flask until 50 ℃. The nanoparticles were poured out and washed with alcohols using the procedure reported in previous work [21].

4.2.3 Film fabrication

The obtained nanoparticles were dispersed in hexanethiol at a mass concentration of 300 mg/ mL. The nanoparticle film coating and selenization in tube furnace was conducted based on the methods reported by Miskin and Hages *et. al*. [21], [60]. The graphite chamber, it was purged with Ar for 15 min before heating up. Heating rate in the RTP was set to 10 ℃ for all the selenization. A constant Ar flow was allowed (0.3 lpm) from the selenium side to the nanoparticle film side during selenization. When the selenization is finished, all the heating lamps are turned off immediately and 5 lpm Ar flow is used to get rid of the residual Se in the graphite box until the temperature dropped below 50 ℃. For the film with Cu coating, 10 nm Cu was thermally evaporated on the surface of the nanoparticle film with a deposition rate of ~ 0.5 Å/s (chamber pressure was kept less than 10^{-6} Torr during the deposition).

4.2.4 Characterization

The grazing incidence x-ray diffraction (GIXRD) patterns were collected in a Rigaku SmartLab Diffractometer using Cu Kα (1.54 Å) with an incident angle of 0.5°. The scanning electron microscope (SEM) images were obtained from FEI Quanta 3D. Raman spectrum were acquired by HORIBA Jobin Yvon LabRam HR800 with an excitation laser wavelength of 633 nm.

4.3 Result and discussion

4.3.1 Temperature for selenization

To explore how temperature affects the selenization process, sulfide nanoparticle films were selenized at 425℃, 450℃ and 500℃ in a tube furnace for 20 min. The phases present from GIXRD analysis are shown in Figure 4.1a) in comparison with a simulated AZTSe diffraction pattern using crystal structure data from Gong *et al.* [56]. From the XRD of 425℃ selenized sample, the most

significant peak is at 14.8º, corresponding to the (001) plane of $SnSe_2$ (ICSD #43857). The (112) peak from AZTSe is present but weak, due to the low crystallinity of AZTSe. When the nanoparticle film was annealed in Se at 450℃, AZTSe is the primary phase in the film and most of the peaks from AZTSe were present along with (001) and (102) peaks from $SnSe_2$. When the selenization temperature was increased to 500 ℃, the AZTSe film was textured with (112) orientation comparing with the simulated standard and with a small residual peak at ~15º, representing a small amount of $SnSe_2$ left in the film. The microstructures and phases observed by SEM/ EDS are the same as in XRD patterns. There are two different particle morphologies in the film selenized at 425 ℃ (Figure 4.1b): rod-like particles of $SnSe_2$, and large, flat particles of AZTSe. In the case of selenization at 450 ℃, the film was composed of more uniform AZTSe grains compared with the case of 425 ℃. However, $SnSe_2$ plates were observed embedded edge-on in the AZTSe film. When the temperature was increased to 500℃, the AZTSe grains within the film are even more uniform and flat in contrast to the low temperature selenizations, and $SnSe_2$ plates were no longer present. In addition, comparing with the standard AZTSe and AZTS patterns, the positions of the major peaks do not show a shift towards AZTS (high angle direction) in XRD, suggesting a full depletion of sulfur during selenization. This is in contrast to selenization of solution-processed CZTSe: it is common that selenization in tube furnaces produces alloys of sulfide and selenide [21], [27], [104], [105].

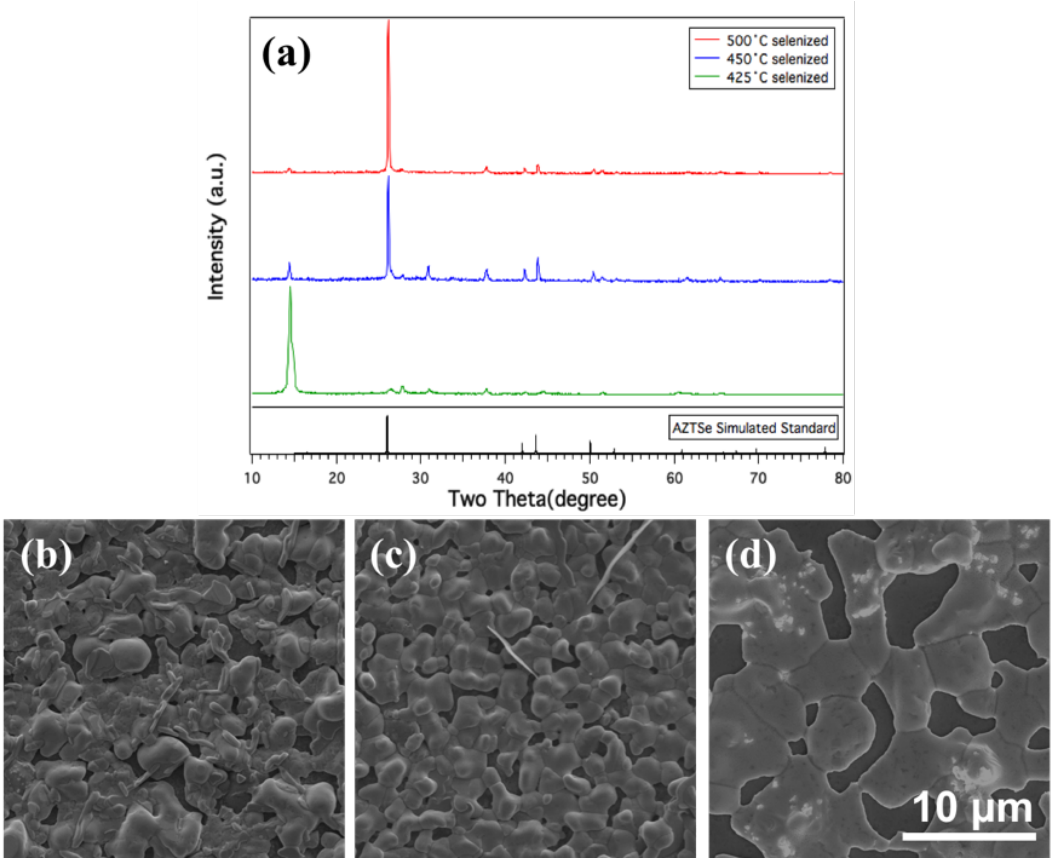

Figure 4.1 (a) XRD comparison of sulfide nanoparticle films selenized at 425°C, 450°C and 500°C as a comparison to standard AZTS; top view SEM images of nanoparticle film selenized at (b) 425°C (c) 450°C (d) and 500°C

From the temperature study above, it can be concluded that high temperature selenization suppresses the formation of $SnSe_2$ secondary phase. However, when using 500°C selenization, AZTSe films are less dense compared with low temperature selenization, likely due to a combination of vapor phase loss and dewetting.

In an attempt to create AZTSe films without $SnSe_2$, rapid thermal processing was utilized to achieve 475 °C within 2min. Figure 4.2 shows the XRD pattern of sulfide nanoparticles grown at a heating rate of 10 °C/s. When the selenization temperature was set to 475 °C, no $SnSe_2$ or any secondary phase(s) were detected by XRD, and no significant texture was found in the as formed

AZTSe grains. All the details in XRD pattern matched exactly with the simulated standard of AZTSe.

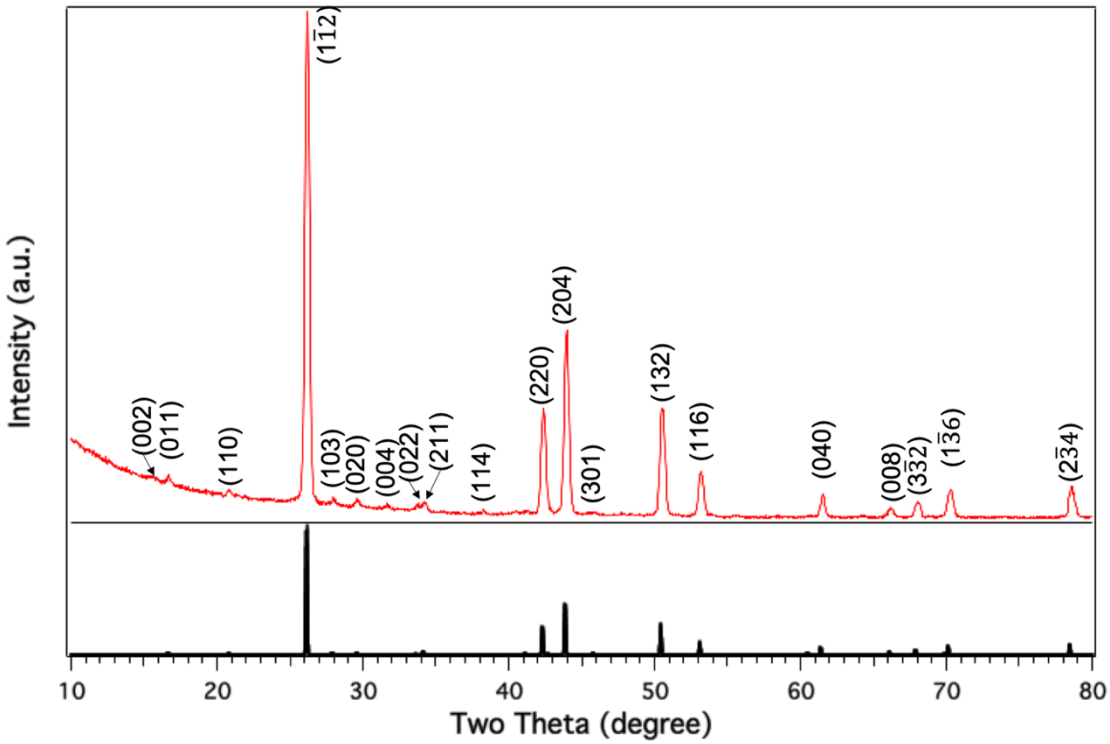

Figure 4.2 XRD of AZTSe film selenized in tube furnace at 475°C as a comparison to simulated AZTSe standard

4.3.2 Microstructure evolution during selenization

To explore the microstructure evolution during selenization, the RTP annealing was interrupted at 1 min, 3 min, 5 min and 10 min to determine the film morphology at different selenization stages, as shown in Figure 4.3. Instead of forming continuous small grains covering the whole surface, as in the CZTSSe case, AZTSe grains formed isolated on the surface after 1 min selenization. After 3min, the grains grew larger compared with 1 min and better film coverage was achieved. The best film coverage was obtained when the selenization time is 5 min, although no significant grain growth was observed. With further selenization, the film started to dewet the FTO surface and

more substrate was exposed. As a result, 5 min was used as the selenization time for the best film coverage in the following sections (if not described separately).

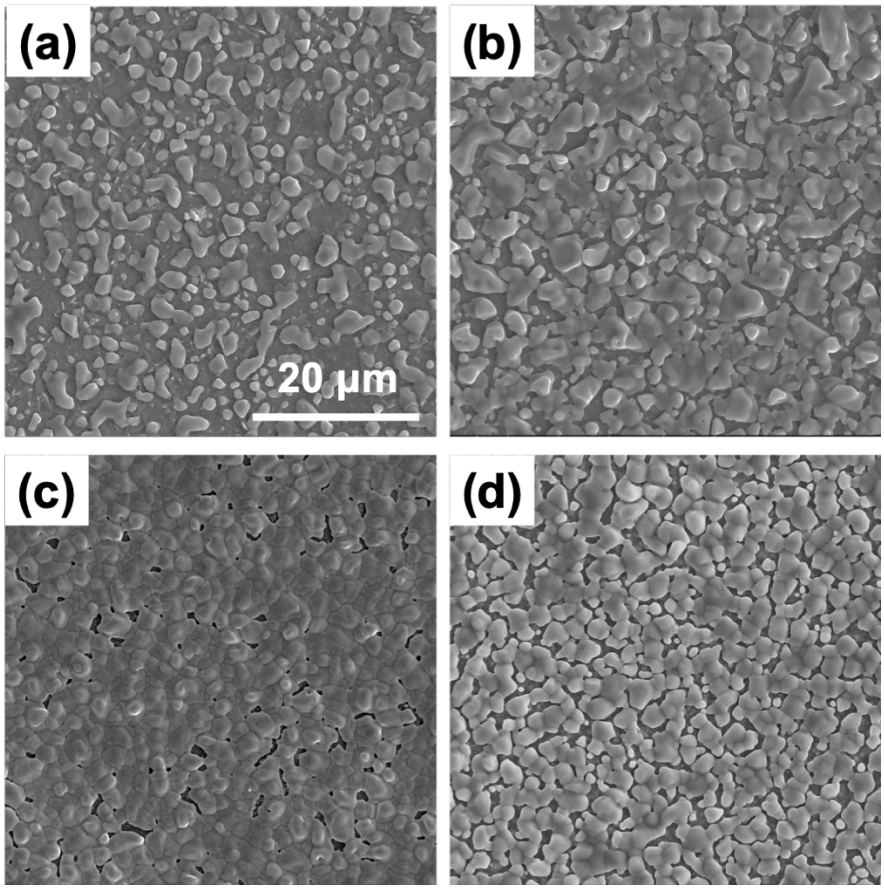

Figure 4.3 SEM plan-view of AZTSSe films selenized for (a) 1 min, (b) 3 min, (c) 5 min and (d) 10 min.

EDS mapping was done for 1 min selenization film as shown in Figure 4.4. The particles formed were Ag and Se rich, the distribution of these two elements overlapped perfectly. While Zn did not really incorporate into the grains, it was found in the film uniformly everywhere. Sulfur was presented in both large grains and nanoparticles, but it had a higher concentration in the nanoparticles than in the large grains, suggesting an S-depleting process during selenization. The distribution of Sn was difficult to determine due to the high concentration of Sn in the FTO substrate.

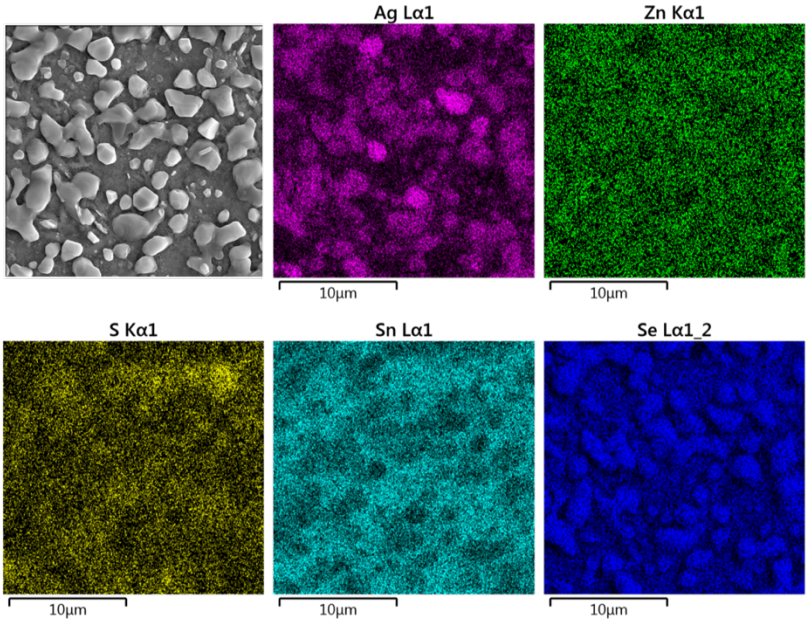

Figure 4.4 EDS mapping of AZTSe film after 1 min selenization from plan-view

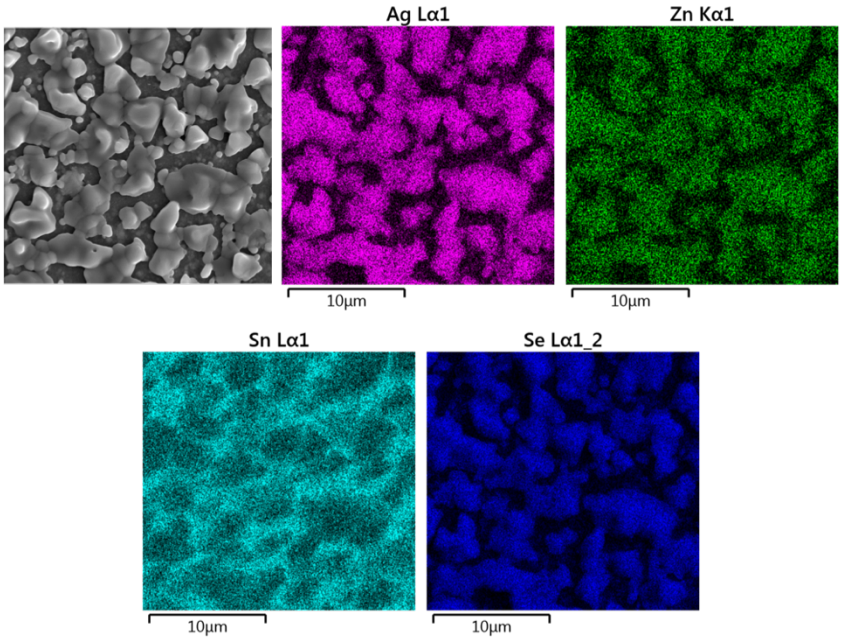

Figure 4.5 EDS mapping of AZTSe film after 3 min selenization from plan-view

After 3min selenization (as shown in Figure 4.5), no S signal was picked up by EDS detector. Differently from the 1 min selenization, the Zn signal highly overlapped with Ag and Se after 3 min, suggesting Zn started to incorporate into the large grains after Ag did. This was very similar to the CZTSSe case, while the sequence of Sn incorporation still needs to be determined with a more detailed study that can separate the fluorescence signals from substrate and the film.

4.3.3 KCN etching

Although the film obtained was phase pure based on XRD, it was still Ag rich from the nanoparticles. Gershon *et al.* have pointed it out that, when Ag/Sn ratio was about 2, the AZTSe films had the best photovoltaic performance. Herein, KCN soaking was utilized to remove extra silver in the nanoparticle film.

KCN has been widely used to remove the secondary phase(s) in metal chalcogenide thin films, especially for Cu related species [70], [106], [107]. However, what are the effects of KCN soaking on Ag-based kesterite thin films are unknown. In this case, a piece of nanoparticle film was cut into five pieces; four of them were soaked in KCN (1M) for 15 s, 60 s, 180 s and 300 s, separately. SEM images and EDS measurement were done on these films to see the morphology and composition change with KCN etching as shown in Figure 4.6 and 4.7.

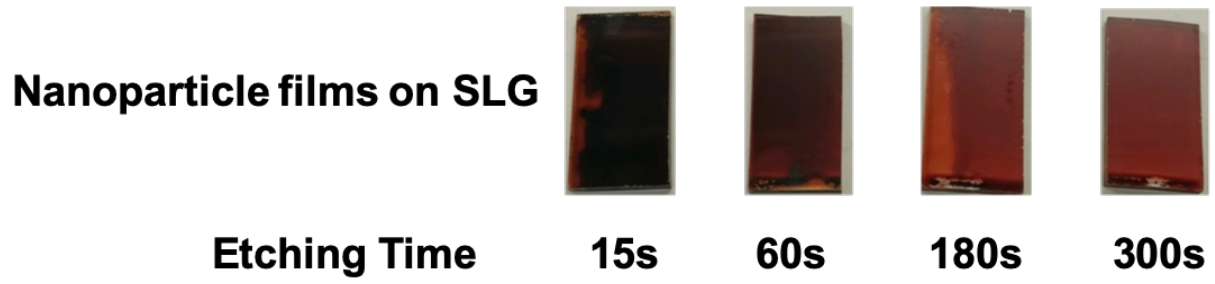

Figure 4.6 Photos of nanoparticle films after soaking in KCN solution for different time period

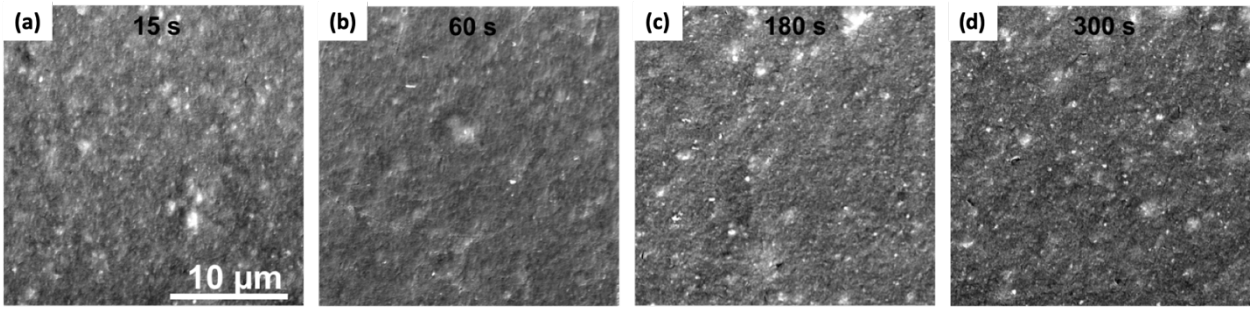

Figure 4.7 SEM images of nanoparticle films after soaking in KCN solution for different time period

From the photos of soaked films, it could clearly be seen that the color of the film became lighter with longer KCN etching. Although the SEM images showed similar morphologies, the compositions of the films did change significantly, especially for silver, as shown in Table 4-1.

Table 4-1 KCN etching effect on film composition

	Ag/Sn	Zn/Sn	S/Sn	K/Sn
No etching	2.5	1.0	4.1	Not detected
Etching for 15 s	2.4	1.1	4.0	0.06
Etching for 60 s	1.9	1.2	4.0	0.08
Etching for 180 s	1.6	1.3	4.0	0.12
Etching for 300 s	1.6	1.3	4.0	0.13

The starting Ag/Sn ratio in the nanoparticle film was 2.5. After etching for 1 min, the ratio went to 1.9. Further etching removed more silver, and Ag/Sn was decreased to as low as 1.6, Although from 3 min to 6 min, no more Ag was removed by KCN etching. With the decrease of the Ag/Sn ratio, the Zn/Sn ratio increased, demonstrating a small portion of Sn was removed along with Ag during soaking. Since etching for 60 s gave the best stoichiometric ratio of all these cations, the 60 s KCN-etched film was selenized as a comparison to the non-soaking film as shown in figure 4.8.

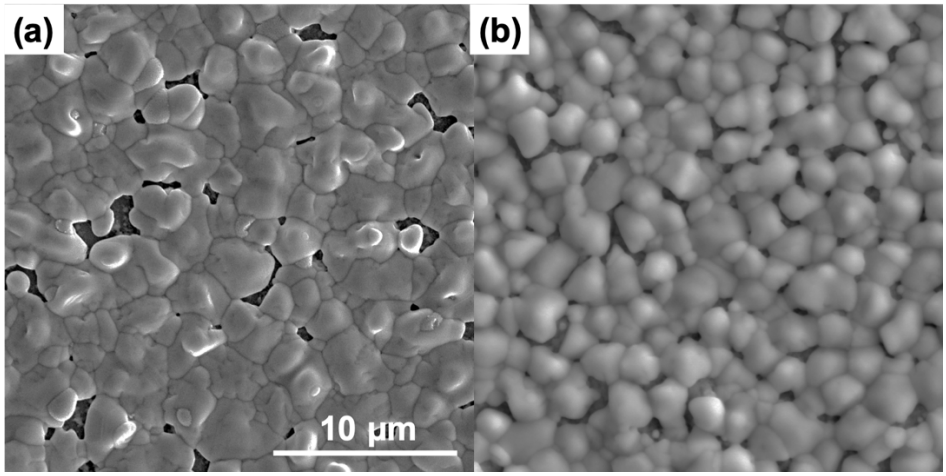

Figure 4.8 AZTSe films (a) without and (b) with KCN etching after selenization at 475°C for 5 min

Despite the compositional change, the phase of the final film remained as pure AZTSe after 1 min of KCN etching as shown in Figure 4.9. The morphology of the film changed after KCN etching. The grains in the film without etching showed more irregular shapes and some Ag accumulation was confirmed by EDS. After KCN etching, the grain shape became more regular with fewer pin-holes in the film. Also, the TRPL (Figure 4.10) were measured to determine the minority charge carrier life time in both cases. With KCN etching and removal of Ag rich phase, the life time carriers was improved significantly.

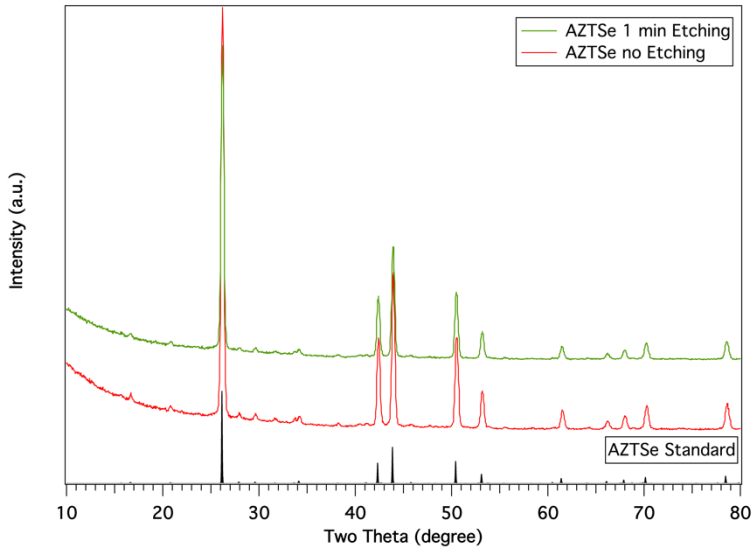

Figure 4.9 XRD of AZTSe with and without KCN etching

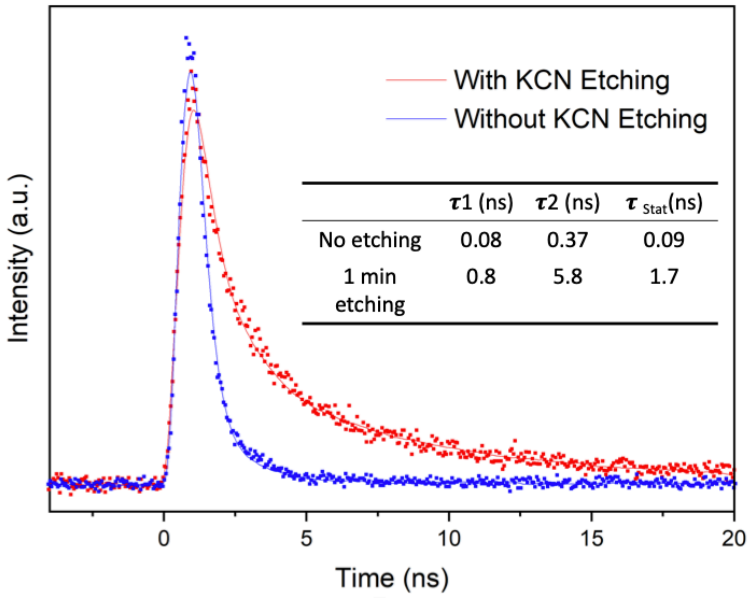

Figure 4.10 TRPL of AZTSe films with/ without KCN etching

4.3.4 Surface engineering by Cu coating

Although a pure phase AZTSe film can be achieved in RTP, the films consisted of grains that were not densely packed, which always result in shunting within the light absorber layer in photovoltaic devices. In contrast, in this type of selenization process for CZTSe, the resulting films are finer and denser. This implies that the nucleation rate of CZTSe is significantly higher than for AZTSe nanoparticles at the beginning of selenization. In an effort to increase the nucleation rate, while maintaining the overall composition close to AZTSe, we developed a transient CZTS step in the beginning of selenization using an evaporated Cu film (10nm) on the AZTS nanoparticle surface. The microstructures of AZTSe with/ without Cu coating after selenization are compared in figure 4.11.

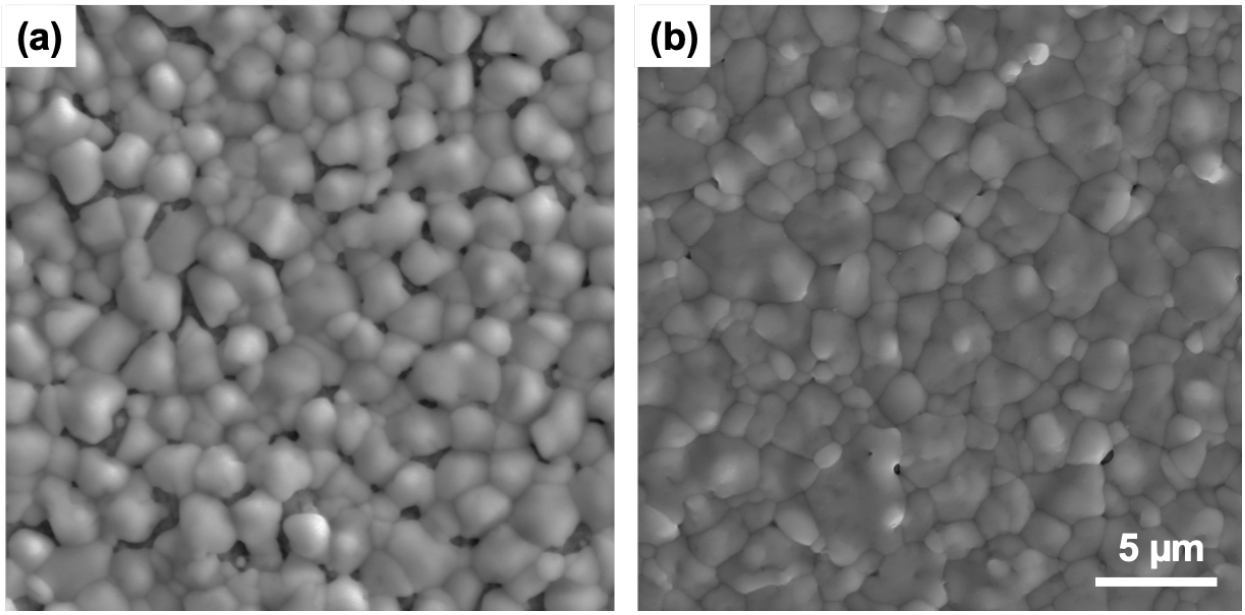

Figure 4.11 SEM plan-view of AZTSe films (a) without and (b) with Cu coating

To explore how Cu affects nucleation, selenization was interrupted after the temperature reaches desired temperature to characterize the extent of coverage and reaction microstructure with and without Cu coating. It can be seen from the XRD (Fig. 4.12) that, after 1 min seleniztion, the bare

film without Cu coating contained AZTSe large grains, while for the nanoparticle films covered with Cu, the grains were an alloy of CZTSe and AZTSe. In addition, there were only a few isolated nucleation sites formed for the film without Cu coating; while for the film with 10 nm Cu coating, the number of nucleation sites forming after 1 min increased by a factor of 10. Since in previous studies, $Cu_{2-x}Se$ precipitation preceded the formation of CZTSe, it is expected that the Cu will be dissolved in Se above 221 ℃, reaching the maximum solubility at 380℃, and $Cu_{2-x}Se$ will precipitate on the surface as nucleation sites as the solubility of Cu in selenium decreases after 380 ℃ [61]. The Ag, Zn and Sn dissolved in the Se liquid precipitated as AZTSe into $Cu_{2-x}Se$ and the final film consisted of AZTSe large grains with small amount of Cu in it (< 5% of Cu/(Cu+Ag) from bulk EDS, which agreed well with estimated Ag/Cu ratio based on relative thickness. However, without the assistance of Cu, no such nucleation sites were formed. The microstructures of AZTSe with/ without Cu coating after selenization (475 ℃ selenization for 5 min in RTP) are compared in Figure 4.12. Without Cu, large grains formed and continued to grow isolated even after long time selenization, creating porous films. With Cu, the grain density was higher at the beginning. With further selenization, the initial grains could easily touch each other and form a continuous film.

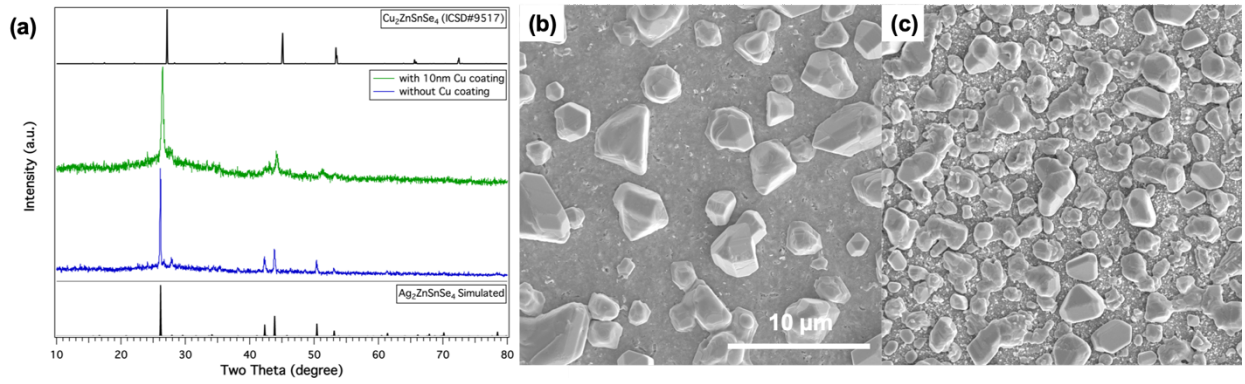

Figure 4.12 (a) XRD of nanoparticle films with and without Cu coating after 1 min selenization; SEM plan-view of the same films (b) without Cu coating (c) with 10 nm Cu coating

The photoluminescence of the Cu coated film was measured, as shown in Figure 4.13. The main peak is located at 1.22 eV, corresponding to the band gap of the material. This value is slightly smaller than the reported AZTSe film because of the Cu incorporation, especially on the surface. Regarding the defect states, all the emissions measured in the PL were from shallow defects. The FWHM of the PL peak is about 65 nm, which is much narrower than the peak from CZTSSe (~110 nm), suggesting fewer defect states in this material.

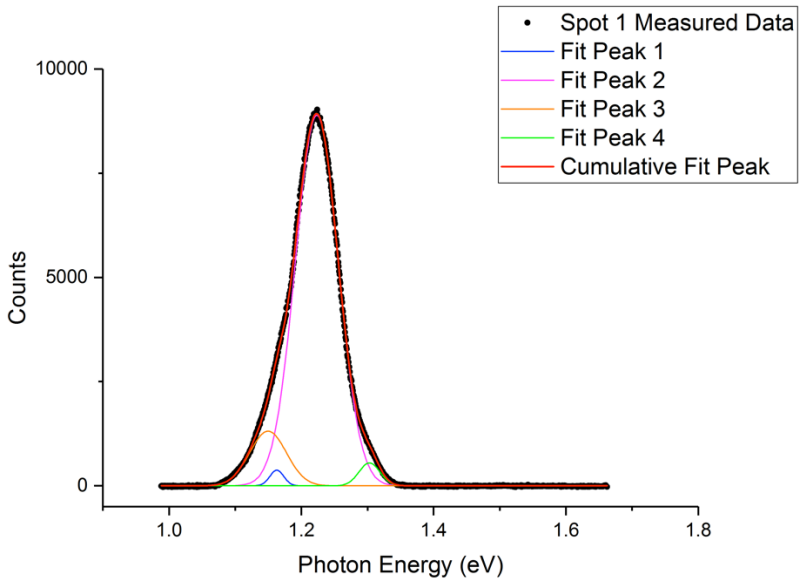

Figure 4.13 PL fitting of AZTSe film with surface engineering

The film was further characterized by XPS to analyze the oxidation states of different elements, as shown in Figure 4.14. For Ag, although no reference is available for AZTSe, no plasma-induced loss feature peak was observed, suggesting the Ag is on a +1 state. Cu $2p_{3/2}$ and $2p_{1/2}$ are relatively weak, due to the small amount, and located at 932.3 eV and 952.2 eV, separated by about 19.9 eV, which is characteristic for Cu^{+} [108], [109]. Although Cu was deposited as elemental Cu, all Cu was converted into a Cu^{+} state after selenization. The Zn $2p_{3/2}$ peak is located at 2021.9 eV,

suggesting that Zn was in a +2 state. Sn $3d_{5/2}$ and $3d_{3/2}$ peaks are located at 486.3 eV and 494.8 eV, respectively, corresponding to a +4 oxidation state. However, a small shoulder peak is observed about 496.5 eV, which may come from the +2 oxidation state [110]. This suggests the possibility of Sn_{Zn} anti-site defects, which generate deep trap states (0.6 eV below conduction band) in light absorber material and significantly reduce the open circuit voltage of the photovoltaic device. The XPS peaks demonstrate a +2 state for both S and Se. The S signal is noisy and weak compared with Se, showing relatively complete S depletion during selenization compared with CZTSSe case [109].

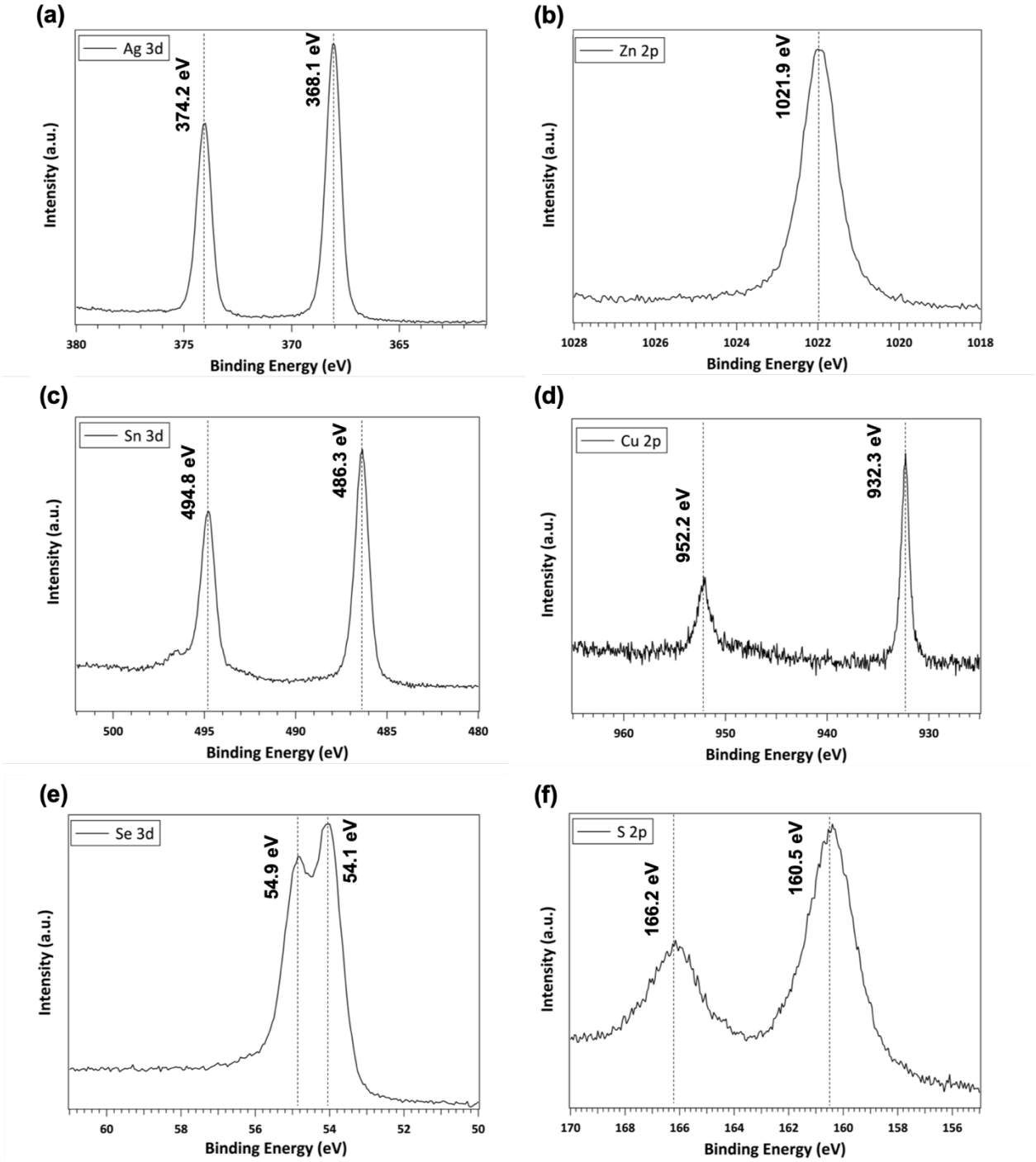

Figure 4.14 High resolution XPS spectra of (a) Ag, (b) Zn, (c) Sn, (d) Cu, (e) S and (f) Se for surface engineered AZTSe film

4.4 Conclusion

In this chapter, sulfide nanoparticles were converted into selenide thin films by annealing in selenium vapor at elevated temperature. Pure phase AZTSe films have been achieved. It was confirmed that the selenization temperature is crucial for getting rid of $SnSe_2$ secondary phase, which rules out the traditional tube furnace selenization due to the long heating ramp. The selenization time was only 5 min, much shorter than that for CZTSSe. This will make the roll-to-toll process more accessible since the length of the selenization furnace can be much shorter with short selenization time. KCN etching was used to remove extra Ag to avoid Ag rich phase in final film, which significantly enhances the carrier lifetime in the final film.

Also, a strategy to improve the film morphology is proposed here to reduce the pinhole density of AZTSe films. A 10 nm-thick Cu layer was utilized to serve as nucleation sites at the surface of the nanoparticle film at the early stage selenization. Due to higher solubility of Cu in liquid selenium, more small grains were observed for the nanoparticle film with Cu coating compared with non-coated one when selenization was interrupted after 1min. The elemental Cu coat was converted into Cu^+ after selenization, although a small portion of Sn may have been at +2 states instead of +4. The resulting film had strong photoluminescence yield, with narrow FWHM compared with CZTSSe, demonstrating a less defective structure, which is very promising as a light absorber material for future photovoltaic application.

4.5 Additional information

4.5.1 KCN etching of Ag

A KCN solution was used to remove Ag in the nanoparticle film; however, it remains unknown what kind of Ag was removed by KCN soaking. Also, after the same KCN soaking time, the composition of the films may vary for films that underwent different heat treatment after coating. Here, the sulfide nanoparticle films were coated and annealed at different temperatures. After 1 min KCN solution soaking, the composition of them were as listed in the Table 4-2. It shows that when the film was coated and annealed in the air, the etching effect on Ag/Sn was much more significant than in the glovebox, which had oxygen level controlled below 0.1 ppm. Also, higher temperature annealed samples had more Ag loss after KCN etching. It is possible that during annealing, Ag was oxidized in air and these oxides were subsequently removed by KCN etching. Higher temperatures resulted in more oxidation and led to more Ag removal. For the glovebox annealed sample, Ag was still removed until Ag/Sn=2.1, perhaps due to the residual oxygen in the nanoparticle film induced in early nanoparticle synthesis procedure. More detailed study is needed for the mechanism of the Ag etching in KCN solution.

Table 4-2 Atomic composition of films coated and annealed in different environment

	Coat and anneal in air			Coat and anneal in glovebox		
annealing temperature	300°C	400°C	500°C	300°C	400°C	500°C
Ag/Sn	2.1	1.9	1.2	2.6	2.4	2.1
Zn/Sn	1.1	1.1	0.8	1.0	0.9	1.0

It has been noticed that the oxidation happens even at room temperature. If the sulfide nanoparticle films were stored in air for a long time (a few weeks), the KCN soaking could remove the whole

film. As a result, the nanoparticle film had to be stored in an oxygen-free environment and selenized in a timely manner once it was coated.

4.5.2 Ultraviolet photoelectron spectrum (UPS) of AZTSe after surface engineering

The UPS of the as selenized AZTSe with Cu coating was conducted to determine the absolute band position as well as the Fermi level of this material as shown in Figure 4.15.

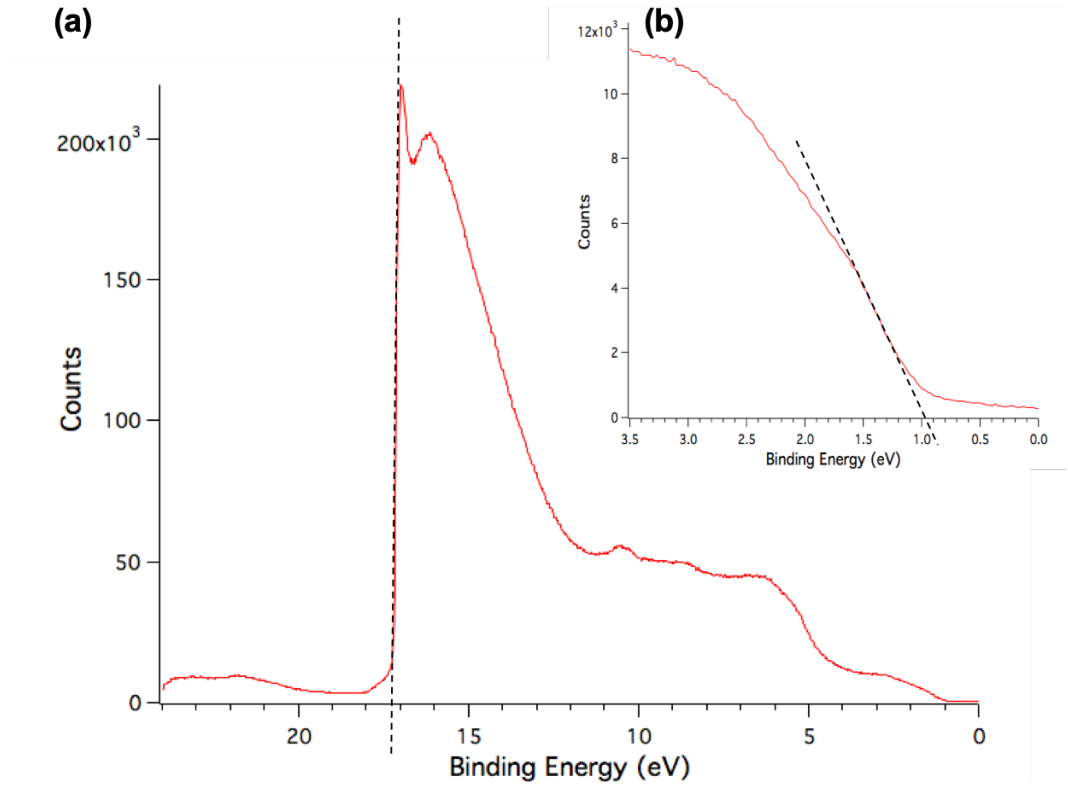

Figure 4.15 UPS of AZTSe film with surface engineering

The band position and fermi level can be calculated from:

$$\Phi = h\upsilon - (E_{cuoff} - E_{fermi}) \quad 4.1$$

$$\text{HOMO (VB)} = -[\Phi + (E_{VB} - E_{fermi})] \quad 4.2$$

in which Φ is the work function or Fermi level of the material, hυ is the incident x-ray energy, which is 21.22 eV in this case; $E_{cuoff} - E_{fermi}$ is the intercept we extracted from the Figure 4.15(a) and $E_{VB} - E_{fermi}$ is the interception obtained from the inserted figure in 4.15(b).

The work function or the distance between Fermi level and vacuum level is:

$$\Phi = 21.22\text{eV} - 17.13\text{eV} = 4.09\ \text{eV} \tag{4.3}$$

The absolute distance between valence band to vacuum level in this material is

$$\text{HOMO (VB)} = -[4.09\text{eV} + 0.99\text{eV}] = -5.08\ \text{eV} \tag{4.4}$$

Since the band gap of the film was 1.22 eV as measureed by PL as demonstrate previously, the Fermi level is about 0.2 eV away from the conduction band, suggesting donor-based defect states, or this material is an n-type semiconductor.

4.5.3 Compositional characterization for AZTSe thin film

A photovoltaic device was fabricated based on an architecture from bottom to top as: FTO/ AZTSe/ MoO_3 (50 nm)/ ITO (220 nm)/ Ni/Al. The cross-section of the film was using a cut in focused ion beam and observed under STEM. EDS mapping was conducted in the area, as shown in Figure 4.16.

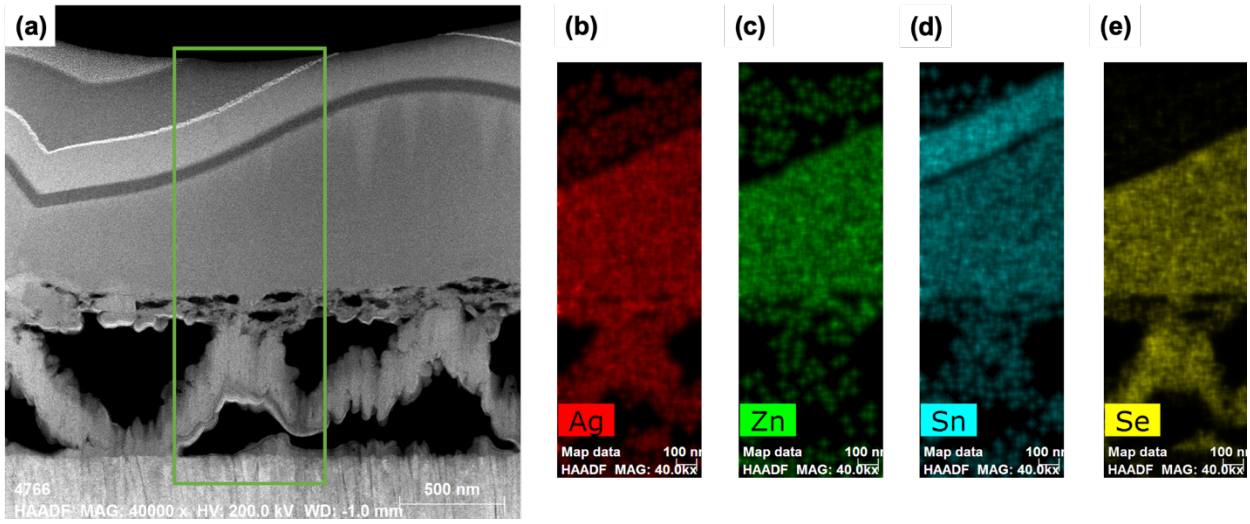

Figure 4.16 EDS-mapping of the cross-section of AZTSe device (a) HAADF image and elemental distribution in the labelled area (b) Ag, (c) Zn; (d) Sn and (e) Se.

From the cross-section image, the AZTSe film is very different from CZTSSe for the morphology of the "fine grain layer". After selenization of CZTSSe, the fine grain layer normally consisted of closely-packed fine particles, while the layer underneath AZTSe grains was very porous. This was perhaps due to the fast selenization of this material. When the materials were dissolved in liquid selenium and formed large grains on the top very rapidly, voids remained in the layers below. This layer had very limited contact points with both the absorber layer and the back contact, which affected the transport of electrons and holes significantly. The composition of the large grain and the porous layers are listed in Table 5-3. The large grains were slightly Ag poor (Ag/Sn=1.9) and Zn rich (Zn/Sn=1.1), which agreed with the composition measured after KCN soaking mentioned previously and is the preferred stoichiometric ratio for high performance AZTSe absorber [97]. The porous layer had high sulfur concentration. Since the selenization was so fast for AZTSe, residual sulfur from the nanoparticles remained. A small amount of oxygen was left in this layer as well, which probably came from the nanoparticle synthesis and film annealing. No carbon from nanoparticle ligands was detected in either layer of this part.

Table 4-3 Composition of the large grains and porous layer based on cross-section EDS

at. %	Ag	Zn	Sn	Se	S	C	O
Large grain	23.8	14.0	12.7	43.6	5.9	0	0
Porous layer	12.9	0.4	1.3	36.3	40.1	0	0.6

4.5.4 Device performance

The photovoltaic performance of AZTSe solar cells is shown in Figure 4.17. The whole film had photovoltaic response. However, the efficiencies are different across the same film. The highest performance was 0.35% PCE with 0.1cm^2 total area under AM 1.5 illumination. From the J-V curve, serious shunting behavior was observed. Further optimization, including the choice of back contact, p-type buffer layer (choice of material selection, deposition methods and thickness of this layer), as well as the film roughness, is needed for higher efficiency photovoltaic devices.

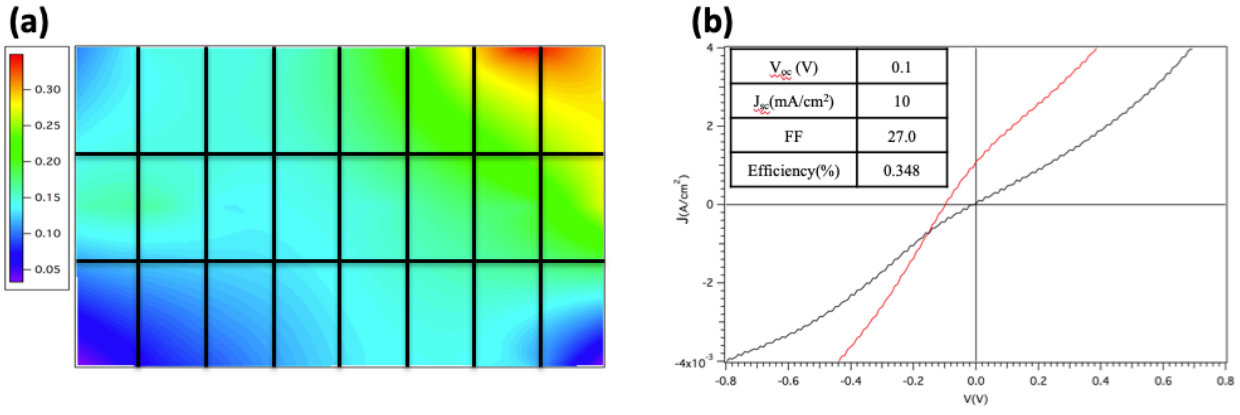

Figure 4.17 Photovoltaic performance of the solar cells using AZTSe as light absorber layer (a) Efficiency distribution across the whole film; The films was separated into 24 small cells with 0.1 cm2 total area for each cell (b) I-V curve of the cell with highest efficiency.

5. SOLUTION PROCESSING OF CADMIUM ZINC SULFIDE THIN FILM AS THE N-TYPE LAYER IN CIGSE/CZTSSE SOLAR CELLS

5.1 Introduction and Background

Cadmium sulfide (CdS), the II-VI binary semiconductor, is one of the most commonly used n-type materials in photovoltaic devices. In 1954, CdS had already been used along with Cu_xS to form the heterojunction as the very first thin film solar cell. Since 1990s, CdS is widely used as the buffer layer in high performance metal chalcogenide thin film solar cells, *e.g.* copper indium gallium selenide ($Cu(In,Ga)Se_2$ or CIGSe), copper zinc tin sulfo-selenide ($Cu_2ZnSn(S,Se)_4$ or CZTSSe) and cadmium telluride (CdTe) thin film solar cells [111].

Compared with other n-type materials, CdS stands out because of its stability, low cost, good band alignment, as well as compatibility with the light absorbers in solar cells. Naturally insufficient in sulfur, CdS crystals have free electrons as the charge carriers with a direct band gap. The band gap width fluctuates between 2.40-2.46 eV depending on different thickness and deposition methods [112]. Generally, there are two different crystal structures of CdS, *i.e.* a face-centered cubic or zinc blende structure ($F\bar{4}3m$, ICSD #81925), and a hexagonal or wurtzite structure (P63mc, ICSD #154186). Although the wurtzite phase is supposed to have a slightly lower formation energy compared with the zinc blende phase by first principle calculation [113], both structures of CdS have similar energy band positions and can be used as the n-type material in thin film photovoltaics.

Among various deposition methods for CdS, including sputtering[114], thermal evaporation[115], close space sublimation (CSS)[116] and solution-phase based deposition, chemical bath deposited (CBD) CdS generally has higher efficiency compared with other deposition methods, especially

in CIGSe or CZTSSe solar cells. For CBD CdS, the p-type absorber layer is soaked in ammonia water solution at elevated temperature (~65°C). A cadmium salt solution ($CdSO_4$, $CdCl_2$ or $Cd(OAc)_2$ et al.) along with thiourea solution was added to start the deposition. The ammonium acts as the buffer solution since Cd^{2+} can combine with them to form complexes, which will reduce the concentration of Cd^{2+} in the solution. Consequently, it will hinder the precipitation of $Cd(OH)_2$. At the same time, thiourea reacts with hydroxyl to release S^{2-}, which reacts with Cd^{2+} to form CdS on the surface of the metal chalcogenide film. The reaction is described as below [117]:

$$Cd^{2+} + 4NH_3 \leftrightarrow Cd(NH_4)_4{}^{2+} \quad 5.1$$

$$(NH)_2CS + OH^- \leftrightarrow SH^- + H_2O + H_2CN_2 \quad 5.2$$

$$SH^- + OH^- \leftrightarrow S^{2-} + H_2O \quad 5.3$$

$$Cd^{2+} + S^{2-} \rightarrow CdS \downarrow \quad 5.4$$

Other than serving as an n-type semiconductor to form p-n junction with the p-type absorber, it is also believed that the deposition process itself is beneficial to the solar cell performance for further aspects:

a. The solution deposition process prevents the surface damage from sputtering.

b. For metal chalcogenide thin films, soaking in the ammonium hydroxide water solution helps to remove the insulating oxide layer top of CIGSe or CZTSSe.

c. In CIGSe or CZTSSe, this reaction solution can slightly dissolve Cu^+ and thus forms an inter-diffusion layer at the p-n junction, benefiting the band alignment [115], [118].

d. The as-obtained film is annealed in air to get rid of moisture in the film after the bath. During the CBD method, a small amount of $Cd(OH)_2$ precipitates along with CdS. This annealing process promotes the decomposition of this compound and formation of CdO, which decreases the overall resistance of this layer [119].

However, due to the normal architecture of the solar cells, when CdS is on top of the main light absorber layer, the band gap of CdS becomes a limitation for further improvement regarding efficiencies of metal chalcogenide thin film solar cells. A considerable portion of the light that has a wavelength shorter than 550 nm will be absorbed by the CdS layer instead of the light absorber layer, which will contribute to the final energy conversion. That is also the reason that we can always observe a current loss at left shoulder of EQE spectrum at 550 nm [21], [107].

To solve this problem, researchers were working on incorporation of Zn into CdS and utilize CdZnS alloy as the n-type layer instead. ZnS shares the same two common crystal structures as CdS. Different from CdS, most bulk ZnS appears in the cubic phase rather than hexagonal. Because of the expansion from both the conduction band bottom and valence band top compared with CdS [120], the band width is ~3.78 eV for the cubic structure and ~3.58 eV for the hexagonal structure [121]. Neither of them has significant photon absorption in the visible light range.

Intuitively, taking advantage of the CBD methods, Tosun *et al.* Zn^{2+} salts are added to the bath along with Cd^{2+} salts to form the alloy. However, because CdS has lower solubility in an aqueous environment compared with ZnS, CdS tends to precipitate first and followed by ZnS [122]. As a result, there is an increased Zn^{2+} concentration gradient along the thickness of the film from the

substrate to the top. No uniform CdZnS alloy can be obtained; thus, the absorption of blue light still exists in such films.

Instead of the CBD method, the molecular precursor route offers another deposition possibility for CdS as well as CdZnS thin film fabrication. Through spin coating of a molecular precursor, different kinds of metal chalcogenide thin films with uniform composition can be achieved in different amine-thiol systems, such as CIGS, CZTSSe, SnS_2 and ZnS [27]-[29], [123], [124]. In this chapter, amine-thiol based solution processing method was used to deposit CdS or CdZnS thin films as the n-type layer in CIGS or CZTSSe photovoltaic devices. The phase, morphology, and I-V performance of the films deposited from molecular precursor spin-coating will be compared with the traditional chemical bath deposited CdS.

5.2 Chemical bath deposited CdS

5.2.1 Experiment

5.2.1.1 Materials

Cadmium sulfate ($3CdSO_4 \bullet 8H_2O$, 99.996% Alfa Aesar) is dissolved in ultrapure deionzed water (resistivity >18.2 Mohm•cm, dispensed from Synergy® water purification system from Millipore) at the concentration of 0.015M was used as Cd^{2+} source (Solution 1). Similarly, thiourea (>99%, Sigma-Aldrich) was dissolved ultrapure deionized water at the concentration of 0.75M as the sulfur source (Solution 2). Ammonium hydroxide (NH_4OH, 29.4%, JT Baker) was used as buffer solution.

5.2.1.2 Reaction procedure

A 500 ml water jacketed beaker was connected to a water heater, pre-set to 65°C. When the temperature was stabilized at 65°C, 150 mL of ultrapure water, 22 mL of Solution 1 and 28.57 mL of NH_4OH were poured into the beaker. The freshly selenized CZTSSe samples, which were soaked in ultrapure water for 5 min previously, were merged into the solution mixture immediately. The magnetic stirring bar at 100 r/min. After 1 min elapsed time, Solution 2 was poured into the beaker. Eight CZTSSe films were added into the bath. They were taken out of the bath at 4 different time stages, 11 min, 12 min, 13 min and 15 min. When the films were out of the bath, they were rinsed with ultrapure water and blow-dry by nitrogen gun. These eight films were put into an oven (preset at 120°C) to evaporate all the moisture. After 5 min in the oven, samples were transferred into high vacuum chamber for ZnO/ITO deposition as soon as possible. Devices were finished by ZnO/ITO for the window layers and then Ni/Al for the front contacts.

5.2.2 Characterization of CZTSSe capped with CdS

From Figure 5.1 , it is clear that, with different deposition time, the film color changes from purple, purple-blue, blue to green with longer CdS, which can be used as a future reference for CBD CdS The cross-sections of these films are shown in Figure 5.2 to illustrate the CdS layer in between CZTSSe large grains and ZnO. It can be seen that the CBD method gives a relatively uniform coating of CdS nanoparticles on top of the CZTSSe grains, although a thicker CdS accumulation layer can be found in some concave surfaces, such as at grain boundaries. From the cross-section SEM images, for CdS deposited by 11-13 min, there is no significant difference regarding the thickness of CdS layer. This is probably due to the very limited observation area in SEM and slow deposition rate at the beginning of the reaction. However, from Figure 5.2, the average thickness

of CdS on CZTSSe should be different, determined from the reflected color difference. When the deposition time was 15 min, the thickness of the CdS increased significantly to 80 nm.

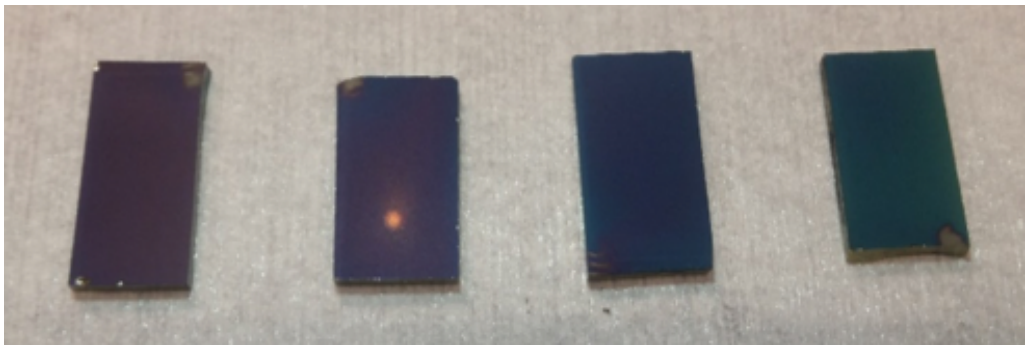

Figure 5.1 Post deposition of CdS on CZTSSe with color difference.

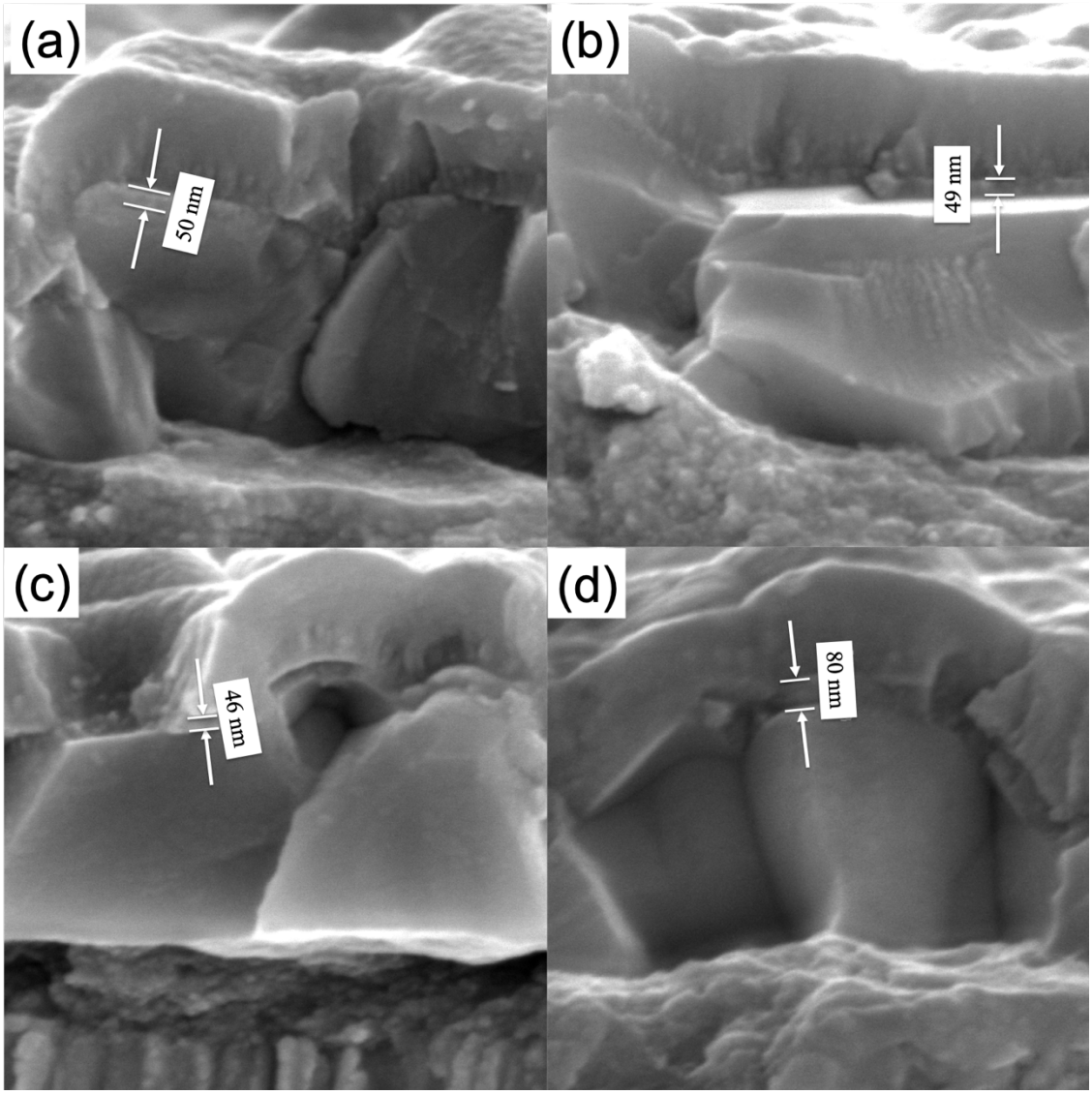

Figure 5.2 SEM iamges of cross-section of CZTSSe devices with CdS deposited for different time periods: (a) 11 min, (b) 12 min, (c) 13 min and (d)15 min.

All of these films were fabricated into solar cells and the photovoltaic performances were measured for all the cells. The efficiency and other parameter distributions of 48 cells are plotted as a function of CdS deposition time in Figure 5.3.

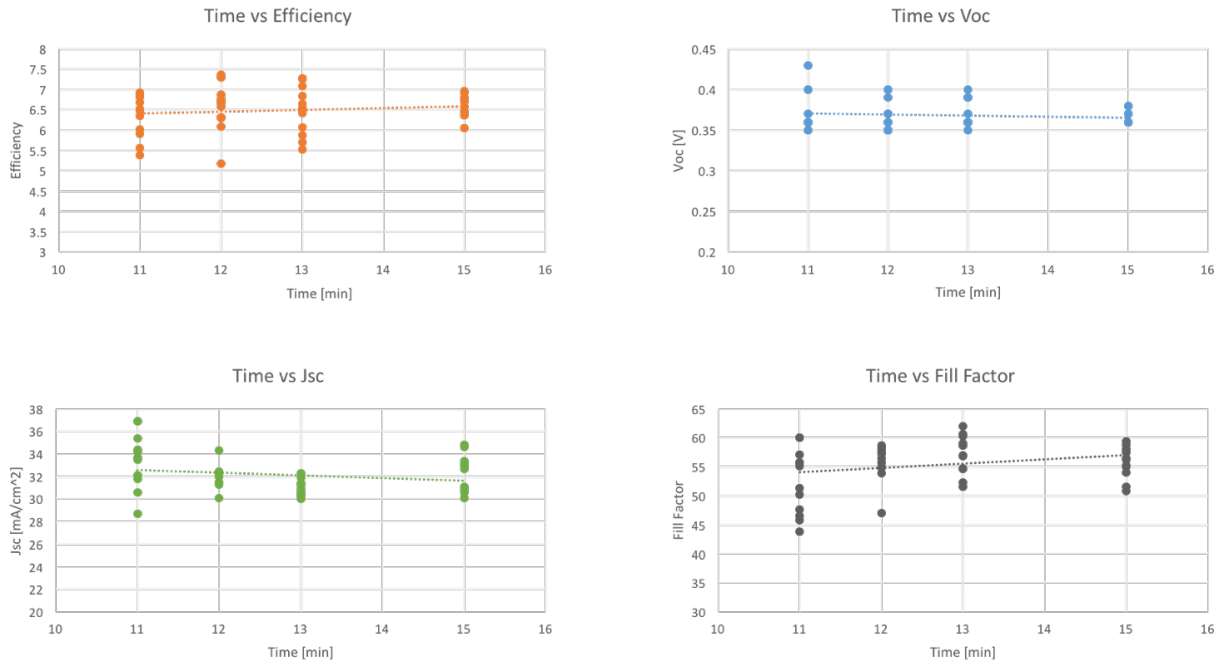

Figure 5.3 Device performance vs. CdS deposition time

From the performance of the solar cells, with different thickness of CdS, the performance of the solar cells is relatively stable. These was no significant influence of the CdS thickness in the range of 45-80 nm, which offers a wide target range for the amine-thiol processed CdS or CdZnS thin films.

5.3 Molecular precursor for CdS and CdZnS thin film

5.3.1 Experiment

5.3.1.1 Materials

Cadmium oxide (CdO, >99.99%, trace metals basis, Sigma Aldrich) and zinc oxide (ZnO, puriss. P.a., ACS reagent, >99.0%, Sigma Aldrich) was used as the cation source. Ethanethiol (C_2H_5SH, 97%, 100mL, Sigma Aldrich) and hexylamine ($CH_3(CH_2)_5NH_2$, 99%, 100mL, Sigma Aldrich) were used as the solvent.

5.3.1.2 Method

Cadmium oxide and zinc oxide was dissolved in a mixture of ethanethiol and hexylamine at the concentration of $[Cd^{2+}+Zn^{2+}]$=0.05 M or 0.1 M. For the Cd^{2+}solution. Two Different methods of adding hexylamine and ethanethiol were used in the dissolution: either hexylamine prepared along with CdO first, and then ethanethiol added drop by drop followed by votexing until it is fully dissolved; or ethanethiol prepared with CdO first and then hexylamine added drop by drop as shown in Figure 5.4.

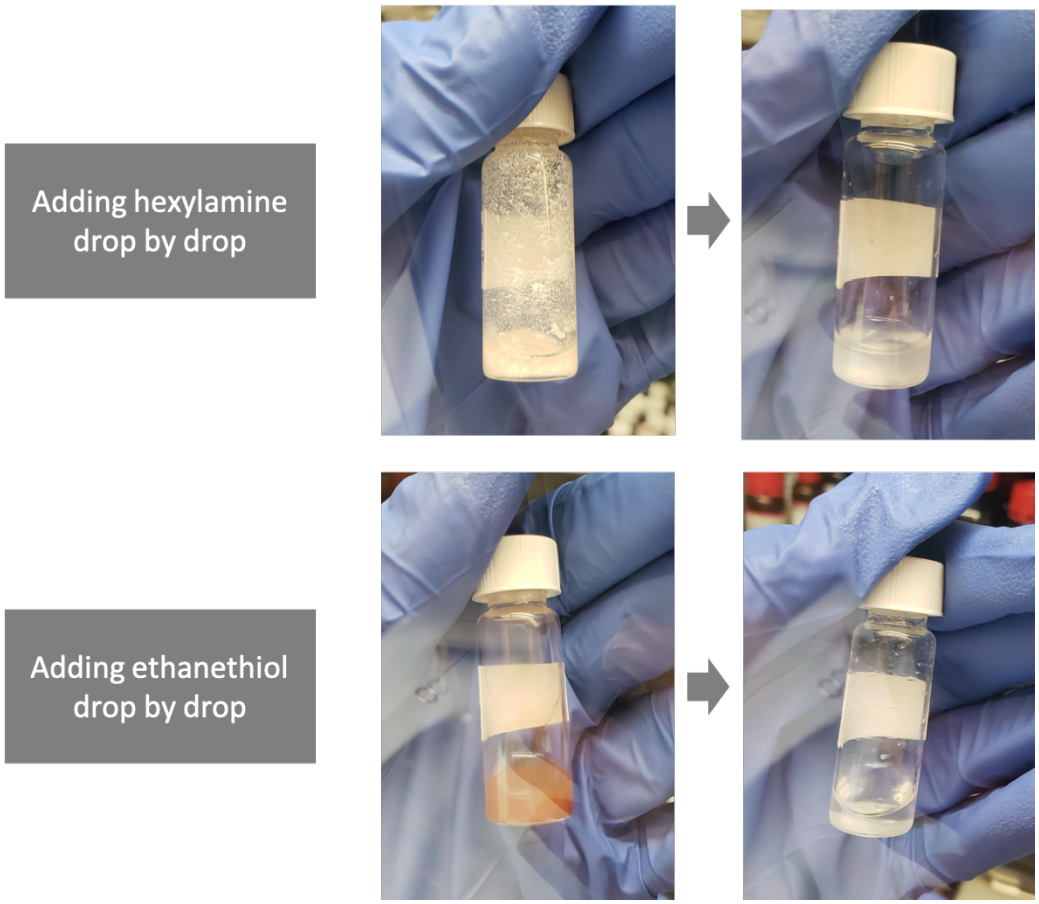

Figure 5.4 Different dissolution phenomenon by adding solvent in different sequences

From Figure 5.4, it can be seen that when hexylamine was added drop by drop, it first formed white complexes and then, with more hexylamine, the complexes were dissolved. In contrast, when

ethanethiol was added drop by drop, no white complexes were found. Instead, the amount of the dark red powder, which corresponded to CdO, decreased with more ethanethiol added. We suspect that when the dissolution happened, CdO formed metal-organic complex(es) with ethanethiol first as shown in figure 5.5[125], and these complex(es) were able to be dissolved in hexylamine. That also explains why the white complex(es) only showed up when hexylamine was not sufficient, while when ethanethiol was not sufficient, CdO stayed as CdO powders. For the dissolving experiment, every 1 mmol of CdO needed about 3 mmol of ethanethiol (in sufficient hexylamine) or 2 mmol of hexylamine (in sufficient ethanethiol) to be fully dissolved. Detailed study on the dissolution mechanism still requires more quantitative investigation through mass-spectrum (MS) or nuclear magnetic resonance (NMR).

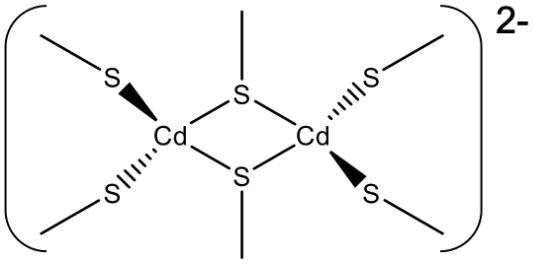

Figure 5.5 Proposed complex structure for cadmium thiolate

Since ethanethiol has a very low boiling point (35 °C) and it evaporateed fast at room temperature. A minimum amount of ethanethiol with enough hexylamine was used as solvent for the following characterization and application. For spin coating, 300 µl of solution was dropped on Molybdenum (Mo, 800 nm) coated soda-lime glass, or fluorine doped tin oxide (FTO, for UV-vis measurement) glass (2.3 mm, surface resistivity ~13 ohm/sq, Sigma Aldrich), or CIGSe/ CZTSSe thin films right after selenization as the n-type layer. The spin rate was set to 500 rpm for the first 5 seconds and 1500 rpm for the next 40 seconds. The first 5 seconds were used to make sure the solution wet the whole surface and formed a liquid thin film, and the next 40 seconds were used to further reduce

the thickness of the film and also dry the film during high-speed spinning. The as-prepared thin film was annealed at hotplate at 350°C for 5min to obtain the final film.

For thermogravimetric analysis (TGA), 100 µl of Cd^{2+} solution was drop cast on Mo glass and dried at room temperature until there was no liquid phase residual. The complex(es) formed was scrapped off by razor blade into a TGA crucible. SDT Q600 was used for TGA measurement. The heating ramp in TGA was 10°C/min and the whole process was under inert gas flow to avoid any oxidation of the complex(es).

For transmission electron microscopy (TEM), solution was diluted in ethanol for 10 times and drop cast on a SiN TEM grid. When there was no liquid phase visible, the TEM grid was transferred onto a glass slide and bake on a hot plate at 350°C for 5min. FEI Tecnai 200 was used for the TEM observation. All the liquid-evolved preparation procedures mentioned above, as well as the chemical weighing, were done in a glovebox with both oxygen and moisture levels lower than 0.1ppm.

5.3.1.3 Characterization of the molecular precursor and the resulting thin films

The TGA plot and the first derivative of weight percentage for the as-formed complex(s) are shown in Figure 5.6. Before 250 °C, there is about 10% weight loss, which came from the evaporation of residual solvent. The major mass loss happened at about 270~280 °C. Since there should be no liquid phase left in the complex, this ~40% weight loss most likely corresponded to the cadmium complex decomposition and byproduct evaporation. This is also consistent with the previous dissolution study. Assuming one Cd atom was bonded with three S atoms on average, to form the complexes as $[Cd_2(SCH_3)_6]^{2-}$, two S as well as the carbon species were lost during decomposition

while one S stayed with Cd to form CdS. The weight loss, in this case, would be about 40% as well. However, the metal thiolates chemistry is relatively complicated and all these suspicions need to be confirmed by more thorough and accurate analysis methods.

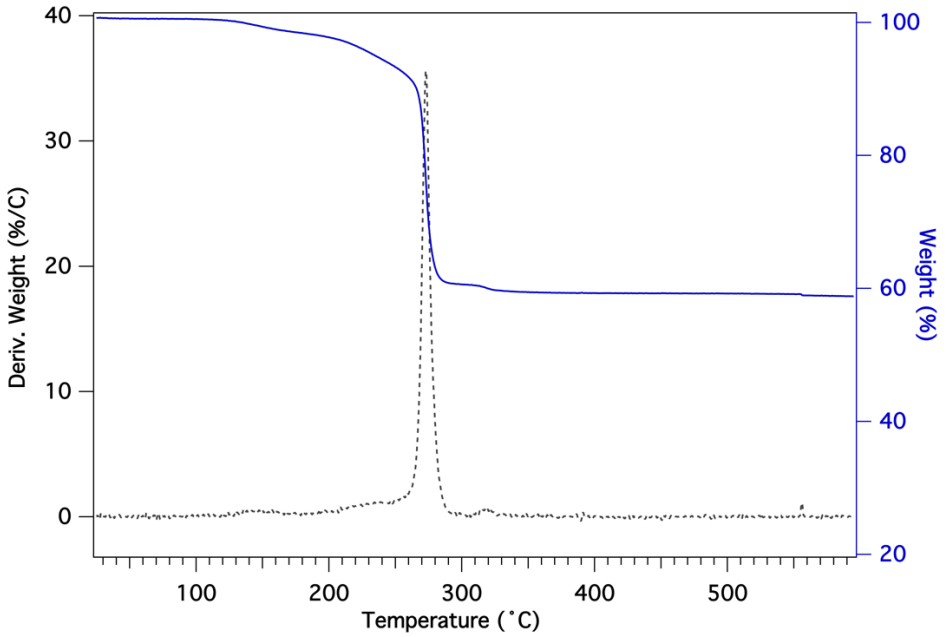

Figure 5.6 TGA curve for the as formed complex from CdO dissolved in hexylamine with minimum ethanethiol at 0.1M

From the TEM image in Figure 5.7, it can be clearly seen that nanoparticles with ~5 nm diameter were formed after the molecular precursor was baked at elevated temperature. When zoomed in (as shown in Figure 5.7b), these nanoparticles appeared well-crystalized and mostly agglomerated with each other. This size is smaller than the generally reported CdS size deposited by chemical bath deposition, which is normally about 10 nm [126].

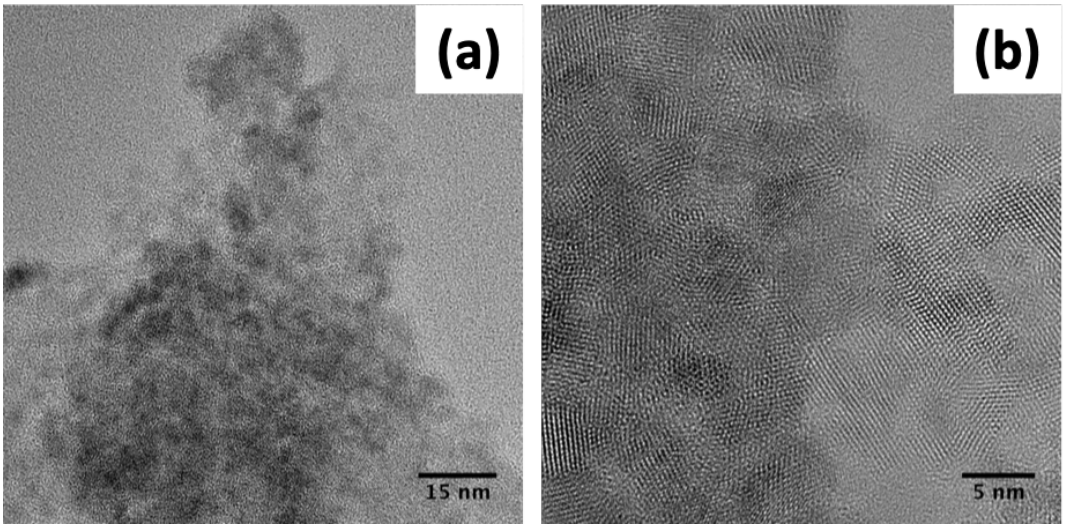

Figure 5.7 (a) TEM image and (b) HRTEM image of the diluted molecular precursor baked on TEM grid

Figure 5.8 shows the XRD patterns of films made from $Cd_xZn_{1-x}S$ films spin-coated with different Cd:Zn ratios. The films tended to have lower crystallinity with higher Zn content. Comparing the XRD patterns with the standards, the as-deposited films were mostly cubic phase, although it is very difficult to tell if there is any wurtzite phase, since the peaks were so weak at high Zn concentration. Also, from low to high Zn concentration, the peaks in XRD patterns slightly shifted to the high angle direction, corresponding to smaller lattice parameters. However, the amplitude of peak shifting is not as large as expected. Based on Vegard's law, if the composition is the same as the starting precursor ratios, the (111) peak of $Cd_{0.6}Zn_{0.4}S$ should be at 27.5° instead of 27.1° as shown in Figure 5.8. This demonstrates that not all the Zn was incorporated evolved into the alloy lattice. There might be two possibilities for this, either Zn evaporateed during film annealing, or it stayed in the amorphous phase. SEM-EDS was conducted on the $Cd_{0.6}Zn_{0.4}S$ film, and it turn out the Cd to Zn ratio was about 3:2, however, about 50% atomic percent of the film consisted of carbon, which implies some Zn may stayed with the carbon species and not incorporated into crystal.

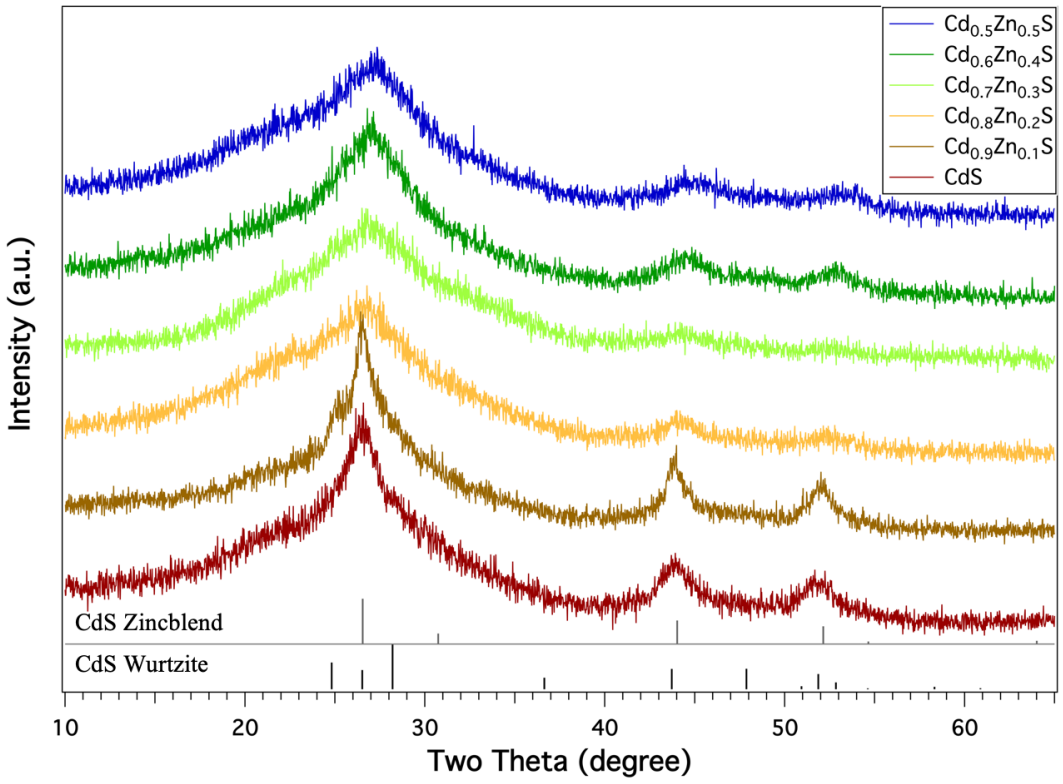

Figure 5.8 XRD of spin-coated film with different starting Cd:Zn ratio

It can be seen from the cross-section images of spin-coated $Cd_xZn_{1-x}S$ films as shown Figure 5.9, that when only CdO was used as the precursor, a dense, flat film with about 100 nm thickness was formed. When more and more ZnO was added to make the alloy, the film was getting more and more porous. When there was only ZnO was used as cation source, the resulting film was much thicker (300 nm) and a layered structure dominated in the film, which made it porous. This result was in consistent with the XRD results, since it also demonstrated a better crystallinity at high Cd concentration.

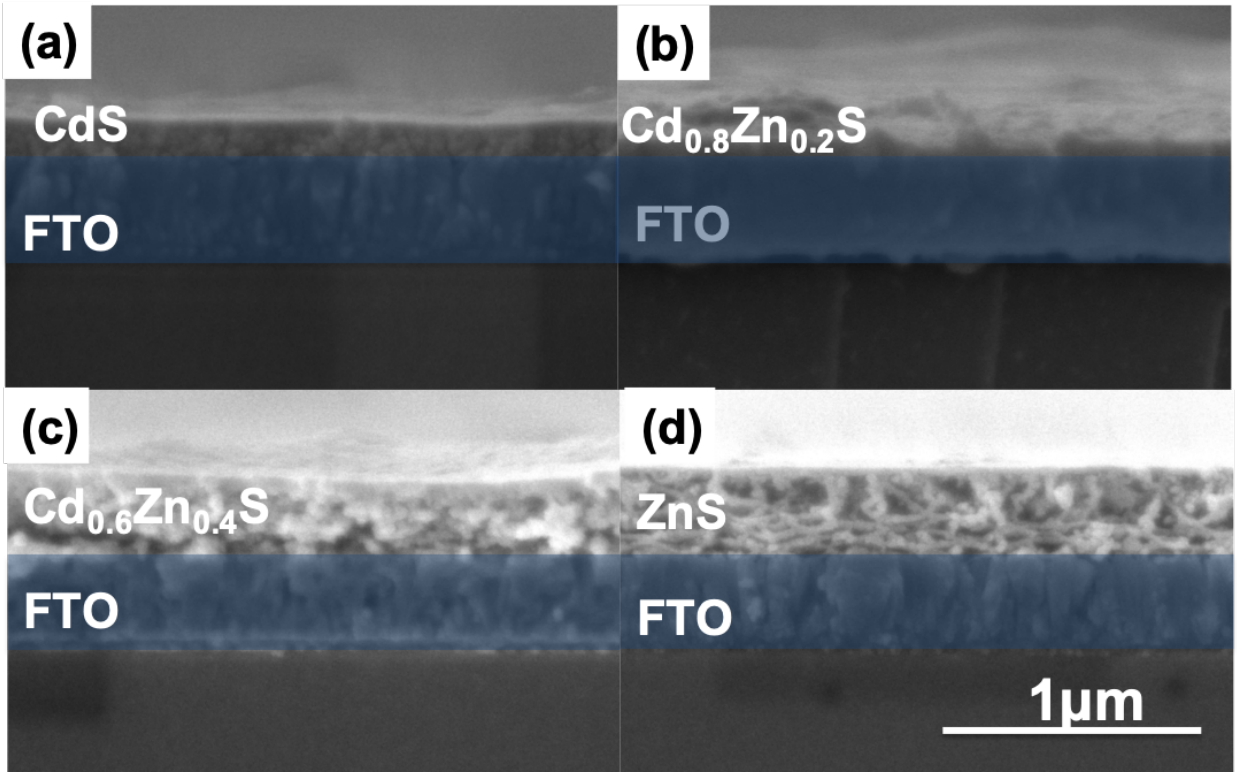

Figure 5.9 Cross-section SEM images of spin-coated (a) CdS, (b) $Cd_{0.8}Zn_{0.2}S$, (c) $Cd_{0.6}Zn_{0.4}S$ and (d) ZnS. Two layers were accumulated for achieve a significant thickness.

From the band gap measurement in UV-vis (Figure 5.9), it can be seen that band gap width increased with Zn concentration. For CdS and ZnS, the band gap widths are the same as previously reported values [127], [128]. However, for the alloys, the band gap widths were slightly narrower, due to the incomplete Zn incorporation during annealing, as we demonstrated before.

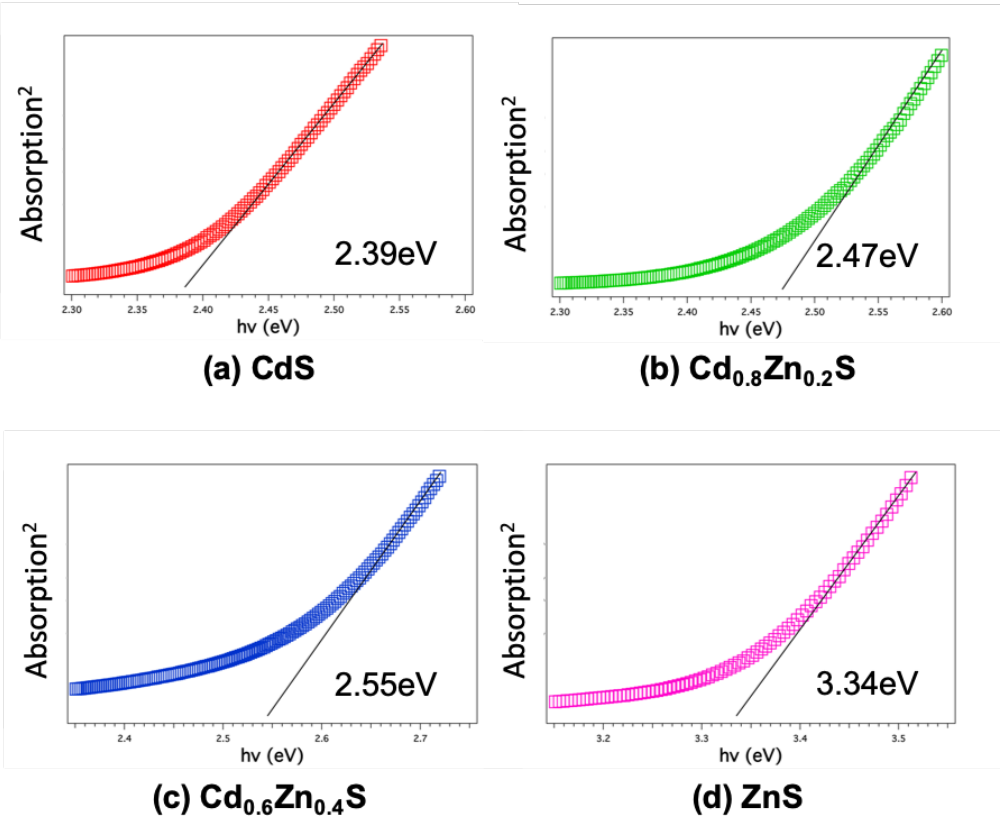

Figure 5.10 UV-vis of spin-coated $Cd_xZn_{1-x}S$ films with differnet Cd/Zn ratio

For photovoltaic application, pure Cd^{2+} solution was applied on CIGSe or CZTSSe thin films with only one layer of spin-coating, which gave about <100 nm thick CdS thin film. These films need to be soaked in water for 5 min before the CdO molecular precursor was spin-coated on the top. By soaking in water, the residual Se after selenization were removed. Otherwise, the hexylamine-ethanethiol solvent could partially dissolve the selenium and left a different wetting behavior than other areas on the film as shown in Figure 5.11. Because of the dissolution of Se, the CdS might be partially converted into CdSSe after annealing, which would make the CdS(Se) grains significantly bigger or more visible under SEM than for the pure CdS. The resulting morphology of CdS(Se) film made the CIGSe layer partially exposed outside, and shunted the device as shown

from the J-V curve in Figure 5.12. The light curve bending towards the x-axis also demonstrated the serious shunting of the solar cell.

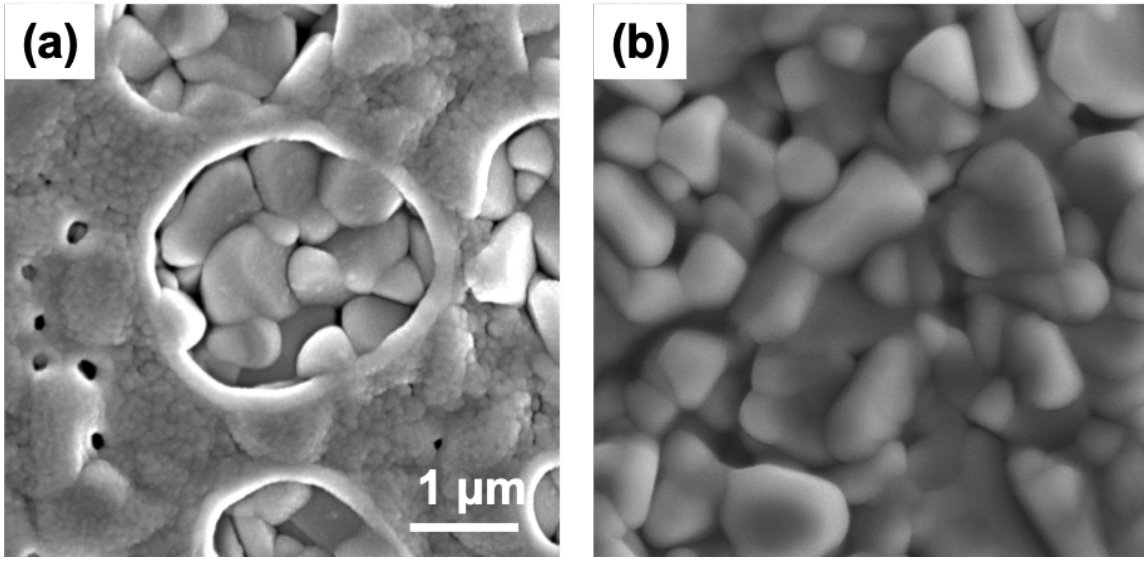

Figure 5.11 SEM plan-view of CdS spin-coated on CIGSe films (a) without soaking and (b) with soaking

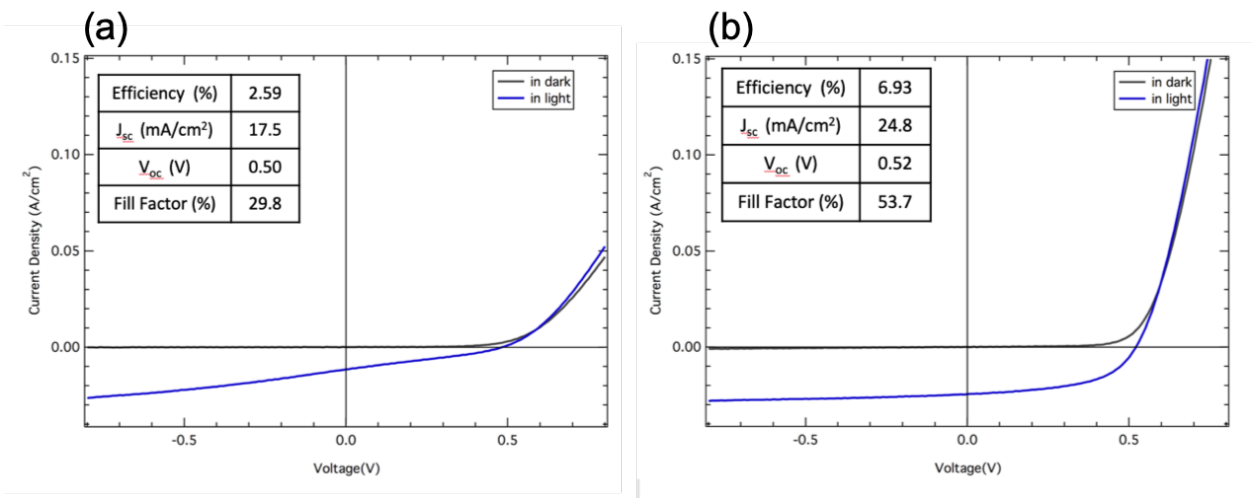

Figure 5.12 I-V curves of CIGSe devices using spin-coated CdS as n-type layer (a) without soaking and (b) with soaking after selenization

After soaking in water to remove residual Se, the efficiency of the solar cells was improved significantly, especially from the short circuit current density and fill factor. However, despite the

full coverage of CdS, there was still be a huge gap between the CBD deposited CdS and spin-coated CdS regarding the photovoltaic performance [107]. To figure out the reason from the composition view, a cross-section sample of a full device with spin-coated CdS was prepared for STEM to determine if there was any spin-coating induced composition fluctuation or structural discontinuity at the interface between CIGSe and CdS.

From the cross-section image in Figure 5.13(a), the resulting CdS film was only about 40 nm thick. The thickness may need to be increased slightly to improve the shunting behavior by optimizing the solution concentration or spin rate. It also can be clearly seen that, although from top view CIGSe are covered with CdS, the CdS and CIGSe layers were not attached to each other closely everywhere. This may significantly limit the current density as a photovoltaic device, since electrons and holes can only be transferred through limited junction points at the interface. Other than the discontinuity between p-type layer and n-type layer, it was also noticeable that the Cd distribution was not uniformly distributed in the CdS layer due to the porous structure of this layer. Also, a significant amount of Cu and In diffused into the CdS layer; they are mostly accumulated at the voids in the CdS layer. It has been shown that, at the interface between CdS and CIGSe, the creation of Cu-deficient layer on top of CIGSe layer may improve the band alignment and enhance the open circuit voltage of CIGSe photovoltaics [129], [130]. However, how to quantitatively control the Cu removed from CIGSe layer or how to prevent Cd and In interdiffusion would be a challenge. Another problem is Se diffusion. Although most Se can be washed away during soaking, the CdS layer still has Se, which may come from the dissolution or diffusion from CIGSe. When CdS is alloyed with Se, the band gap of this layer is reduced, which may further reduce the light absorbed in CIGSe layer.

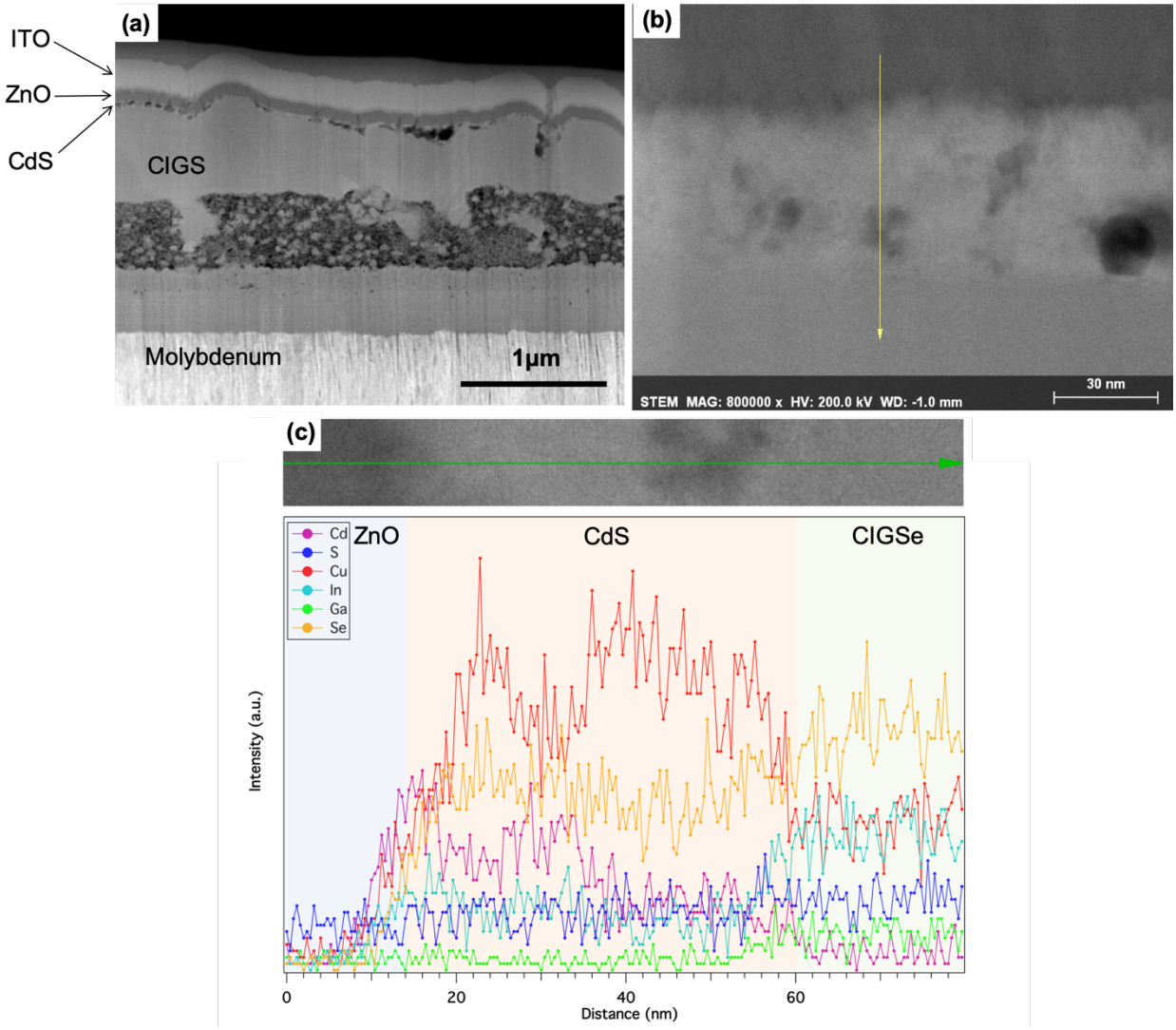

Figure 5.13 (a) Cross-section of CIGSe solar cell using spin-coated CdS as n-type layer; (b) zoom-in image of CdS layer and indication of the line scan location; (c) EDS-line scan of elemental distribution along the arrow

5.4 Conclusion

This chapter examined CdS or $Cd_xZn_{1-x}S$ deposited from either chemical bath deposition or spin-coating of molecular precursor. For chemical bath deposited CdS, the thickness as well as photovoltaic performance of CdS thin films as a function of deposition time have been discussed.

It turns out that, after 11-13 min of deposition, the CdS deposited on an absorber layer is about 50 nm. When deposition time increased to 15 min, the CdS thickness increased to about 80 nm. However, the device photovoltaic performance was not affected significantly. It is possible that, for thicker CdS, resistance is increased and limits the current; however if the CdS is too thin, then the cell may be partly shunted. Thus, there is a balance regarding the thickness of CdS layer. When the surface of the p-type layer is rough, it will be more difficult to determine the optimal CdS layer thickness.

For the molecular precursor route, CdO and ZnO were used as cation sources and ethanethiol was used as a sulfur source as well as solvent along with hexylamine. $Cd_xZn_{1-x}S$ films with different Cd/Zn ratio were deposited successfully. The crystallinity of the films decreaseed with increased Zn concentration, which may result from the different formation energy of CdS and ZnS through the solution phase during annealing. The CdS film coated from the molecular precursor was used as an n-type layer in CIGSe solar cells and achieved 6.9% efficiency. From the cross-section slice of the device, it can be concluded that better film attachment is needed to improve the solar cell performance. The spin-coating and following annealing induced interdiffusion between CdS and CIGSe, which may be another issue to limit the further application of this method.

6. CONCLUSION AND SUGGESTED FUTURE WORK

6.1 Conclusions

In this work, nanoparticle-ink based solution processing for Ag-related kesterite material as the light absorber for thin film photovoltaics has been developed. The microstructure evolution and phase transformation for both the nanoparticle formation and nanoparticle-to-film transition have been studied to understand the mechanism of nucleation, grain growth, and film formation for the future large-scale fabrication of Ag-based kesterite thin films.

CZTSSe was used as the reference material. Ag was added into the system at different concentrations. Ag-alloyed CZTS nanoparticles were synthesized from 10% to 50% [Ag]/[Ag+Cu] ratios. It is suggested that Ag can induce inter- and inner particle inhomogeneity, especially for Ag-rich and Zn-rich particles. More than 30% Ag-alloying can result significant secondary phase formation in the nanoparticles, mainly ZnS. However, after selenization, uniform films are formed due to the re-crystallization and grain growth in selenium, and the Ag put in as a precursor can fully incorporate into the final film. Different stoichiometric ratios of cations, specifically for [Cu+Ag]/[Sn], were used as starting precursor ratio; however, the selenization process itself was able to absorb the depleted extra material and form ACZTSSe grains with the preferred composition. Ag was proven to help with large, flat grain formation, depletion of sulfur, and minimizing the thickness of fine grain layer., However, the optoelectronic properties were not improved with higher Ag concentration, since Ag can result in donor defects and reduce the carrier density in p-type CZTSSe.

To get rid of Cu completely, AZTS nanoparticles were needed. The nanoparticles were synthesized through a solvo-thermal process. The pathway, as well as the size change, for the nanoparticle formation has been revealed. The reaction started with nucleation of binary/ ternary phases. Through the dissolving/ diffusion of the secondary phases, as well as grain growth, the highly crystalized AZTS nanoparticles were formed with uniform elemental distribution.

A strategy to form pure AZTSe films was achieved by selenizing sulfide nanoparticles in selenium vapor at elevated temperature. The selenization conditions were carefully controlled, which includes: 1) selenization temperature was higher than 475°C, and the heating ramp was as fast as possible to avoid the formation of $SnSe_2$; 2) High Se temperature was required to provide enough Se condensation for continuous film formation; 3) KCN soaking was necessary to remove the Ag-rich phase in order to enhance the optoelectronic properties of the film. The very initial film was used as the absorber layer for photovoltaic device and achieved 0.35% efficiency on a total area of $0.1cm^2$ under AM 1.5 illumination.

As the buffer layer in metal chalcogenide thin films, CdZnS was formed by spin-coating of amine-thiol-based molecular precursor. Through deposition of a molecular precursor, CdZnS with different Cd/Zn ratios was obtained. Zn alloying not only increased the band gap, but also change the morphology of the film. With increased Zn concentration, the film porosity increases. The pure CdS film was deposited on CIGSe absorber layers and achieved more than 6.9% efficiency. From the cross-section, it was seen that significants amount of Cu and Se were diffused into the CdS layer. It is believed that the amine-thiol solvent system is very aggressive and may dissolve some

Cu or Se during spin-coating, which limits the further improvement of the efficiency of molecular precursor processed CdS devices.

6.2 Suggested future work

6.2.1 Buffer layer for AZTSe-based thin film solar cells

As we demonstrated before, AZTSe has great potential as a light absorber material in thin film solar cells with promising defect properties. In the initial cell, MoO_3 was used as the buffer layer. However, there is a ~2 eV mismatch between the valence bands of AZTSe and MoO_3.

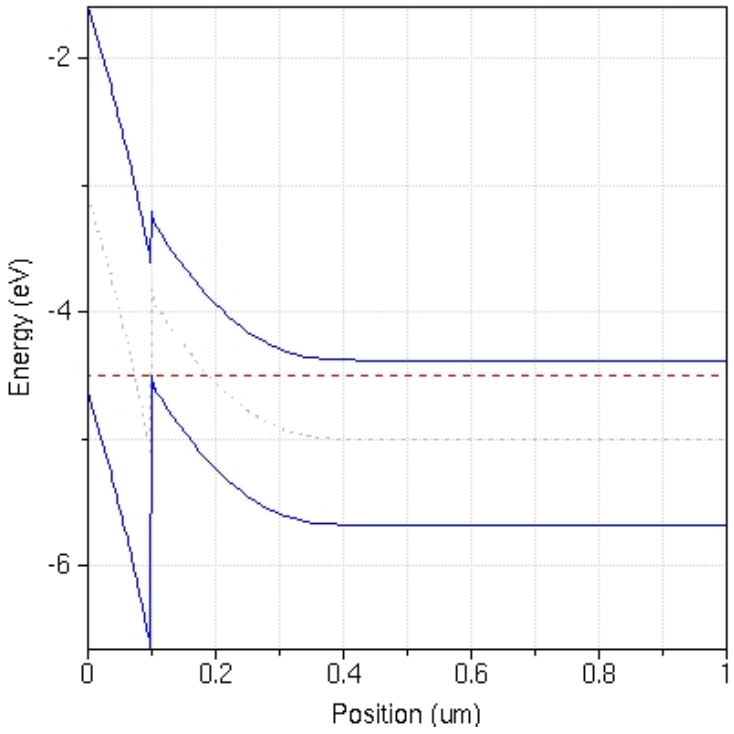

Figure 6.1 ADEPT simulation of band alignment between MoO_3 and AZTSe

As an n-type absorber, holes transfer from AZTSe layer to MoO_3 layer, while the mismatch will eliminate the hole flow significantly. For MoO_3, different heat treatments in different environment can change the band gap by introducing oxygen vacancies or oxygen interstitials. Thus, better band

alignment can be expected by optimized MoO_3 annealing. Another way to solve this problem is to alter the buffer layer with other p-type materials, such as ZnTe or Cu_2O.

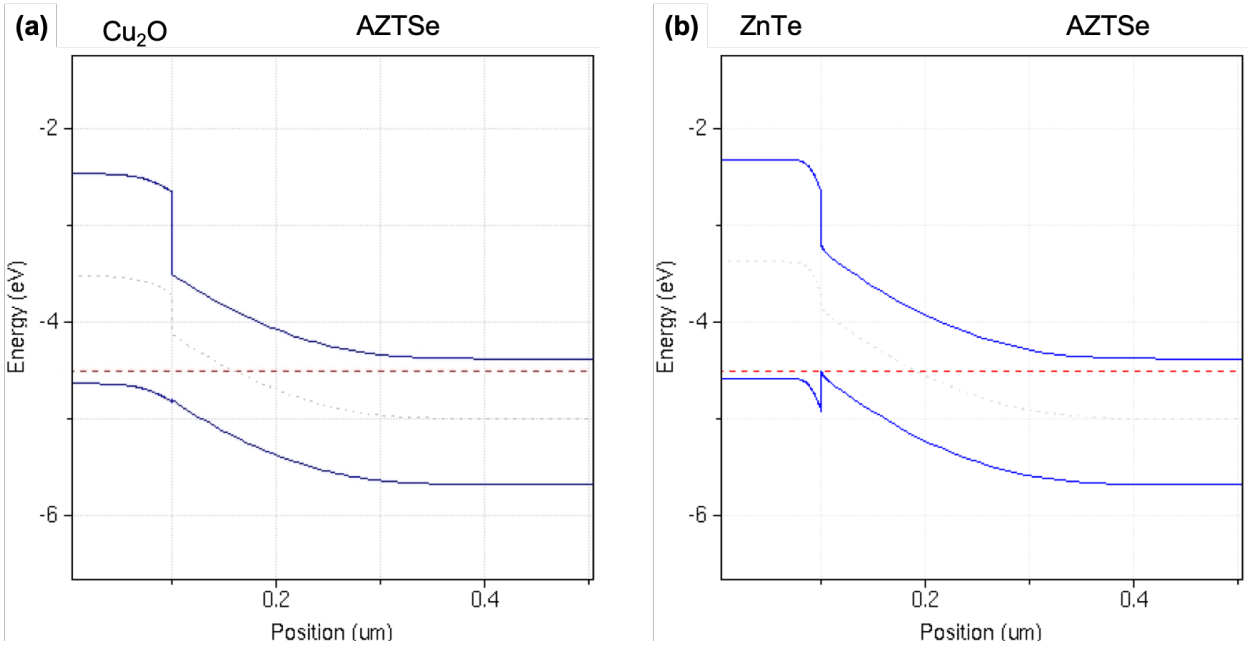

Figure 6.2 Band alignment simulated from ADEPT for (a) Cu_2O and AZTSe; (b) ZnTe and AZTSe

The low carrier density in AZTSe would also be a potential problem, which might be solved by doping to provide more of the donor's defects.

6.2.2 Fast grain growth in AZTSe

It has shown before that the selenization of AZTSe is much faster than that of CZTSSe. The rapid grain growth not only results in a porous fine grain layer underneath, but also may lead to defects and inhomogeneity in the large grains. The mechanism of the large grain size formation remains unknown.

Since oxygen played an important role in the final composition and morphology, more detailed study is needed regarding how oxygen is bound into the nanoparticles and why Ag can be removed

by KCN etching. For future applications, a more oxygen-free or controlled oxygen exposure will be preferred to increase the reproducibility of the films.

6.2.3 Molecular precursor for CdZnS

Although the PCE of molecular precursor deposited CdS has lower efficiency compared with the CBD method, there is still room for improvement of this method: 1) By dissolving pure metal instead of oxides, the carbon species are expected to be removed after annealing; 2) Other benign solvents can be used to dissolve the Cd/Zn complex to avoid the etching of absorber layer; 3) Low boiling point solvents will be preferred to eliminate the material inter-xadiffusion induced by post-coating annealing.

REFERENCES

[1] "BP Energy Outlook 2019 edition," pp. 1–73, Feb. 2019.

[2] U. E. I. A., "Electric Power Annual 2017," pp. 1–239, Dec. 2018.

[3] EIA, "Renewable energy production and consumption by source," May 2019.

[4] EIA, "Monthly Energy Review: Energy Consumption by Sector," May 2019.

[5] T. Song, A. Kanevce, and J. R. Sites, "Choice of substrate material for epitaxial CdTe solar cells," *2015 IEEE 42nd Photovoltaic Specialist Conference (PVSC)*, pp. 1–4, Jun. 2015.

[6] O. Breitenstein, J. P. Rakotoniaina, M. H. Al Rifai, and M. Werner, "Shunt types in crystalline silicon solar cells," *Prog. Photovolt: Res. Appl.*, vol. 12, no. 7, pp. 529–538, 2004.

[7] B. G. Gribov and K. V. Zinovev, "Preparation of High-Purity Silicon for Solar Cells," *Inorganic Materials*, vol. 39, pp. 653–662, Jul. 2003.

[8] K. A. W. Horowitz, R. Fu, T. Silverman, M. Woodhouse, X. Sun, and M. A. Alam, "An Analysis of the Cost and Performance of Photovoltaic Systems as a Function of Module Area," Apr. 2017.

[9] M. A. Green, "Estimates of Te and in prices from direct mining of known ores," *Prog. Photovolt: Res. Appl.*, vol. 17, no. 5, pp. 347–359, Aug. 2009.

[10] C. S. Anderson, "2016 Minerals Yearbook: Indium," May 2019.

[11] X. Li, D. Zhuang, N. Zhang, M. Zhao, X. Yu, P. Liu, Y. Wei, and G. Ren, "Achieving 11.95% efficient Cu 2ZnSnSe 4solar cells fabricated by sputtering a Cu–Zn–Sn–Se quaternary compound target with a selenization process," *J. Mater. Chem. A*, vol. 7, no. 16, pp. 9948–9957, 2019.

[12] J. Kim, G. Y. Kim, D.-H. Son, K.-J. Yang, D.-H. Kim, J.-K. Kang, and W. Jo, "High photo-conversion efficiency $Cu_2ZnSn(S,Se)_4$ thin-film solar cells prepared by compound-precursors and metal-precursors," pp. 1–8, May 2018.

[13] W.-C. Hsu, I. Repins, C. Beall, C. DeHart, G. Teeter, B. To, Y. Yang, and R. Noufi, "The effect of Zn excess on kesterite solar cells," *Solar Energy Materials and Solar Cells*, vol. 113, no. c, pp. 160–164, Jun. 2013.

[14] H. Araki, A. Mikaduki, Y. Kubo, T. Sato, K. Jimbo, W. S. Maw, H. Katagiri, M. Yamazaki, K. Oishi, and A. Takeuchi, "Preparation of Cu_2ZnSnS_4 thin films by sulfurization of stacked metallic layers," *Thin Solid Films*, vol. 517, no. 4, pp. 1457–1460, Dec. 2008.

[15] A. Ennaoui, M. Lux-Steiner, A. Weber, D. Abou-Ras, I. Kötschau, H. W. Schock, R. Schurr, A. Hölzing, S. Jost, R. Hock, T. Voß, J. Schulze, and A. Kirbs, "Cu_2ZnSnS_4 thin film solar cells from electroplated precursors: Novel low-cost perspective," *Thin Solid Films*, vol. 517, no. 7, pp. 2511–2514, Feb. 2009.

[16] T. R. Rana, N. M. Shinde, and J. Kim, "Novel chemical route for chemical bath deposition of Cu_2ZnSnS_4 (CZTS) thin films with stacked precursor thin films," *Materials Letters*, vol. 162, no. C, pp. 40–43, Jan. 2016.

[17] G. Larramona, S. Bourdais, A. Jacob, C. Choné, T. Muto, Y. Cuccaro, B. Delatouche, C. Moisan, D. Péré, and G. Dennler, "Efficient Cu_2ZnSnS_4 solar cells spray coated from a hydro-alcoholic colloid synthesized by instantaneous reaction," *RSC Adv.*, vol. 4, no. 28, pp. 14655–14662, 2014.

[18] B. Shin, O. Gunawan, Y. Zhu, N. A. Bojarczuk, S. J. Chey, and S. Guha, "Thin film solar cell with 8.4% power conversion efficiency using an earth-abundant Cu_2ZnSnS_4 absorber," *Prog. Photovolt: Res. Appl.*, vol. 21, no. 1, pp. 72–76, Nov. 2011.

[19] W. Wang, M. T. Winkler, O. Gunawan, T. Gokmen, T. K. Todorov, Y. Zhu, and D. B. Mitzi, "Device Characteristics of CZTSSe Thin-Film Solar Cells with 12.6% Efficiency," *Adv. Energy Mater.*, vol. 4, no. 7, pp. 1301465–5, Nov. 2013.

[20] H. Xin, J. K. Katahara, I. L. Braly, and H. W. Hillhouse, "8% Efficient $Cu_2ZnSn(S,Se)_4$ Solar Cells from Redox Equilibrated Simple Precursors in DMSO," *Adv. Energy Mater.*, vol. 4, no. 11, pp. 1301823–5, Apr. 2014.

[21] C. K. Miskin, W.-C. Yang, C. J. Hages, N. J. Carter, C. S. Joglekar, E. A. Stach, and R. Agrawal, "9.0% efficient $Cu_2ZnSn(S,Se)_4$ solar cells from selenized nanoparticle inks," *Prog. Photovolt: Res. Appl.*, vol. 23, no. 5, pp. 654–659, Feb. 2014.

[22] C. J. Hibberd, E. Chassaing, W. Liu, D. B. Mitzi, D. Lincot, and A. N. Tiwari, "Non-vacuum methods for formation of Cu(In, Ga)(Se, $S)_2$ thin film photovoltaic absorbers," *Prog. Photovolt: Res. Appl.*, vol. 18, no. 6, pp. 434–452, Aug. 2010.

[23] H. Zhou, W.-C. Hsu, H.-S. Duan, B. Bob, W. Yang, T.-B. Song, C.-J. Hsu, and Y. Yang, "CZTS nanocrystals: a promising approach for next generation thin film photovoltaics," *Energy Environ. Sci.*, vol. 6, no. 10, pp. 2822–17, 2013.

[24] G. Brammertz, M. Buffière, S. Oueslati, H. ElAnzeery, K. Ben Messaoud, S. Sahayaraj, C. Köble, M. Meuris, and J. Poortmans, "Characterization of defects in 9.7% efficient $Cu_2ZnSnSe_4$-CdS-ZnO solar cells," *Appl. Phys. Lett.*, vol. 103, no. 16, pp. 163904–5, Oct. 2013.

[25] T. K. Todorov, K. B. Reuter, and D. B. Mitzi, "High-Efficiency Solar Cell with Earth-Abundant Liquid-Processed Absorber," *Adv. Mater.*, vol. 22, no. 20, pp. E156–E159, May 2010.

[26] B. C. Walker and R. Agrawal, “Contamination-free solutions of selenium in amines for nanoparticle synthesis,” *Chem. Commun.*, vol. 50, no. 61, pp. 8331–4, 2014.

[27] R. Zhang, S. M. Szczepaniak, N. J. Carter, C. A. Handwerker, and R. Agrawal, “A Versatile Solution Route to Efficient Cu 2ZnSn(S,Se) 4Thin-Film Solar Cells,” *Chem. Mater.*, vol. 27, no. 6, pp. 2114–2120, Mar. 2015.

[28] R. Zhang, S. Cho, D. G. Lim, X. Hu, E. A. Stach, C. A. Handwerker, and R. Agrawal, “Metal–metal chalcogenide molecular precursors to binary, ternary, and quaternary metal chalcogenide thin films for electronic devices,” *Chem. Commun.*, vol. 52, no. 28, pp. 5007–5010, Mar. 2016.

[29] C. L. McCarthy and R. L. Brutchey, “Solution processing of chalcogenide materials using thiol–amine ‘alkahest’ solvent systems,” *Chem. Commun.*, vol. 53, no. 36, pp. 4888–4902, 2017.

[30] P. Zhang, Q. Yu, X. Min, L. Guo, J. Shi, X. Zhao, D. Li, Y. Luo, H. Wu, Q. Meng, and S. Wu, “Fabrication of $Cu_2ZnSn(S,Se)_4$ photovoltaic devices with 10% efficiency by optimizing the annealing temperature of precursor films,” *RSC Adv.*, vol. 8, no. 8, pp. 4119–4124, 2018.

[31] J. Fu, J. Fu, Q. Tian, H. Wang, F. Zhao, J. Kong, X. Zhao, and S. Wu, “Tuning the Se Content in $Cu_2ZnSn(S,Se)_4$ Absorber to Achieve 9.7% Solar Cell Efficiency from a Thiol/Amine-Based Solution Process,” *ACS Appl. Energy Mater.*, vol. 1, no. 2, pp. 594–601, Feb. 2018.

[32] W. Ki and H. W. Hillhouse, “Earth-Abundant Element Photovoltaics Directly from Soluble Precursors with High Yield Using a Non-Toxic Solvent,” *Adv. Energy Mater.*, vol. 1, no. 5, pp. 732–735, Aug. 2011.

[33] Q. Guo, H. W. Hillhouse, and R. Agrawal, “Synthesis of Cu_2ZnSnS_4 Nanocrystal Ink and Its Use for Solar Cells,” *J. Am. Chem. Soc.*, vol. 131, no. 33, pp. 11672–11673, Aug. 2009.

[34] Q. Guo, G. M. Ford, W.-C. Yang, B. C. Walker, E. A. Stach, H. W. Hillhouse, and R. Agrawal, “Fabrication of 7.2% Efficient CZTSSe Solar Cells Using CZTS Nanocrystals,” *J. Am. Chem. Soc.*, vol. 132, no. 49, pp. 17384–17386, Dec. 2010.

[35] C. J. Hages, M. J. Koeper, and R. Agrawal, “Optoelectronic and material properties of nanocrystal-based CZTSe absorbers with Ag-alloying,” *Solar Energy Materials and Solar Cells*, vol. 145, no. 3, pp. 342–348, Feb. 2016.

[36] C. J. Hages, S. Levcenco, C. K. Miskin, J. H. Alsmeier, D. Abou-Ras, R. G. Wilks, M. Bär, T. Unold, and R. Agrawal, “Improved performance of Ge-alloyed CZTGeSSe thin-film solar cells through control of elemental losses,” *Prog. Photovolt: Res. Appl.*, vol. 23, no. 3, pp. 376–384, Dec. 2013.

[37] H. Du, F. Yan, M. Young, B. To, C.-S. Jiang, P. Dippo, D. Kuciauskas, Z. Chi, E. A. Lund, C. Hancock, W. M. Hlaing OO, M. A. Scarpulla, and G. Teeter, "Investigation of combinatorial coevaporated thin film Cu_2ZnSnS_4: Temperature effect, crystalline phases, morphology, and photoluminescence," vol. 115, no. 17, pp. 173502–12, May 2014.

[38] H. Katagiri, K. Saitoh, T. Washio, H. Shinohara, T. Kurumadani, and K. Rui, "Development of thin film solar cell based on Cu_2ZnSnS_4 thin films," *Solar Energy Materials and Solar Cells*, vol. 65, pp. 141–148, 2001.

[39] Y. S. Lee, T. Gershon, O. Gunawan, T. K. Todorov, T. Gokmen, Y. Virgus, and S. Guha, "$Cu_2ZnSnSe_4$ Thin-Film Solar Cells by Thermal Co-evaporation with 11.6% Efficiency and Improved Minority Carrier Diffusion Length," *Adv. Energy Mater.*, vol. 5, no. 7, pp. 1401372–4, Dec. 2014.

[40] H. Xin, S. M. Vorpahl, A. D. Collord, I. L. Braly, A. R. Uhl, B. W. Krueger, D. S. Ginger, and H. W. Hillhouse, "Lithium-doping inverts the nanoscale electric field at the grain boundaries in $Cu_2ZnSn(S,Se)_4$ and increases photovoltaic efficiency.," *Phys. Chem. Chem. Phys.*, vol. 17, no. 37, pp. 23859–23866, Oct. 2015.

[41] S. Bourdais, C. Choné, B. Delatouche, A. Jacob, G. Larramona, C. Moisan, A. Lafond, F. Donatini, G. Rey, S. Siebentritt, A. Walsh, and G. Dennler, "Is the Cu/Zn Disorder the Main Culprit for the Voltage Deficit in Kesterite Solar Cells?" *Adv. Energy Mater.*, vol. 6, no. 12, pp. 1502276–21, Mar. 2016.

[42] T. Gokmen, O. Gunawan, T. K. Todorov, and D. B. Mitzi, "Band tailing and efficiency limitation in kesterite solar cells," *Appl. Phys. Lett.*, vol. 103, no. 10, pp. 103506–6, Sep. 2013.

[43] S. Chen, A. Walsh, X.-G. Gong, and S.-H. Wei, "Classification of Lattice Defects in the Kesterite Cu_2ZnSnS_4 and $Cu_2ZnSnSe_4$ Earth-Abundant Solar Cell Absorbers," *Adv. Mater.*, vol. 25, no. 11, pp. 1522–1539, Feb. 2013.

[44] S. Chen, X. G. Gong, A. Walsh, and S.-H. Wei, "Intrinsic point defects and complexes in the quaternary kesterite semiconductor Cu_2ZnSnS_4," *Phys. Rev. B*, vol. 81, no. 24, pp. 245204–10, Jun. 2010.

[45] Y. S. Yee, B. Magyari-Köpe, Y. Nishi, S. F. Bent, and B. M. Clemens, "Deep recombination centers in $Cu_2ZnSnSe_4$ revealed by screened-exchange hybrid density functional theory," *Phys. Rev. B*, vol. 92, no. 19, pp. 195201–13, Nov. 2015.

[46] H. Hempel, R. Eichberger, I. Repins, and T. Unold, "The effect of Cu-Zn disorder on charge carrier mobility and lifetime in $Cu_2ZnSnSe_4$," *Thin Solid Films*, vol. 666, pp. 40–43, Nov. 2018.

[47] J. J. S. Scragg, J. K. Larsen, M. Kumar, C. Persson, J. Sendler, S. Siebentritt, and C. Platzer-Björkman, "Cu-Zn disorder and band gap fluctuations in Cu 2ZnSn(S,Se) 4: Theoretical and experimental investigations," *Phys. Status Solidi B*, vol. 253, no. 2, pp. 247–254, Sep. 2015.

[48] P. Zawadzki, A. Zakutayev, and S. Lany, “Entropy-Driven Clustering in Tetrahedrally Bonded Multinary Materials,” *Phys. Rev. Applied*, vol. 3, no. 3, pp. 034007–7, Mar. 2015.

[49] Q. Guo, G. M. Ford, W.-C. Yang, C. J. Hages, H. W. Hillhouse, and R. Agrawal, “Enhancing the performance of CZTSSe solar cells with Ge alloying,” *Solar Energy Materials and Solar Cells*, vol. 105, no. C, pp. 132–136, Oct. 2012.

[50] G. M. Ford, Q. Guo, R. Agrawal, and H. W. Hillhouse, “Earth Abundant Element $Cu_2Zn(Sn_{1-x}Ge_x)S_4$ Nanocrystals for Tunable Band Gap Solar Cells: 6.8% Efficient Device Fabrication,” *Chem. Mater.*, vol. 23, no. 10, pp. 2626–2629, May 2011.

[51] G. S. Gautam, T. P. Senftle, and E. A. Carter, “Understanding the Effects of Cd and Ag Doping in Cu_2ZnSnS_4 Solar Cells,” *Chem. Mater.*, vol. 30, no. 14, pp. 4543–4555, Jun. 2018.

[52] Z. Su, J. M. R. Tan, X. Li, X. Zeng, S. K. Batabyal, and L. H. Wong, “Cation Substitution of Solution-Processed Cu_2ZnSnS_4 Thin Film Solar Cell with over 9% Efficiency,” *Adv. Energy Mater.*, vol. 5, no. 19, pp. 1500682–7, Jul. 2015.

[53] Y.-F. Qi, D.-X. Kou, W.-H. Zhou, Z.-J. Zhou, Q.-W. Tian, Y.-N. Meng, X.-S. Liu, Z.-L. Du, and S.-X. Wu, “Engineering of interface band bending and defects elimination via a Ag-graded active layer for efficient $(Cu,Ag)_2ZnSn(S,Se)_4$ solar cells,” *Energy Environ. Sci.*, vol. 10, pp. 2401–2410, Nov. 2017.

[54] T. Gershon, Y. S. Lee, P. Antunez, R. Mankad, S. Singh, D. Bishop, O. Gunawan, M. Hopstaken, and R. Haight, “Photovoltaic Materials and Devices Based on the Alloyed Kesterite Absorber $(Ag_xCu_{1-x})_2ZnSnSe_4$,” *Adv. Energy Mater.*, vol. 6, no. 10, pp. 1502468–7, Mar. 2016.

[55] Y. Qi, Q. Tian, Y. Meng, D. Kou, Z. Zhou, W. Zhou, and S. Wu, “Elemental Precursor Solution Processed $(Cu_{1-x}Ag_x)_2ZnSn(S,Se)_4$ Photovoltaic Devices with over 10% Efficiency,” *ACS Appl. Mater. Interfaces*, vol. 9, pp. 21243–21250, Jun. 2017.

[56] W. Gong, T. Tabata, K. Takei, M. Morihama, T. Maeda, and T. Wada, “Crystallographic and optical properties of $(Cu, Ag)_2ZnSnS_4$ and $(Cu, Ag)_2ZnSnSe_4$ solid solutions,” *Phys. Status Solidi C*, vol. 12, no. 6, pp. 700–703, Apr. 2015.

[57] W.-C. Yang, C. K. Miskin, C. J. Hages, E. C. Hanley, C. A. Handwerker, E. A. Stach, and R. Agrawal, “Kesterite $Cu_2ZnSn(S,Se)_4$ Absorbers Converted from Metastable, Wurtzite-Derived Cu_2ZnSnS_4 Nanoparticles ,” *Chem. Mater.*, pp. 1–5, Jun. 2014.

[58] Z.-K. Yuan, S. Chen, H. Xiang, X.-G. Gong, A. Walsh, J.-S. Park, I. Repins, and S.-H. Wei, “Engineering Solar Cell Absorbers by Exploring the Band Alignment and Defect Disparity: The Case of Cu- and Ag-Based Kesterite Compounds,” *Adv. Funct. Mater.*, vol. 25, no. 43, pp. 6733–6743, Oct. 2015.

[59] R. Mainz, B. C. Walker, S. S. Schmidt, O. Zander, A. Weber, H. Rodriguez-Alvarez, J. Just, M. Klaus, R. Agrawal, and T. Unold, "Real-time observation of $Cu_2ZnSn(S,Se)_4$ solar cell absorber layer formation from nanoparticle precursors," *Phys. Chem. Chem. Phys.*, vol. 15, no. 41, p. 18281, 2013.

[60] C. J. Hages, M. J. Koeper, C. K. Miskin, K. W. Brew, and R. Agrawal, "Controlled Grain Growth for High Performance Nanoparticle-Based Kesterite Solar Cells," *Chem. Mater.*, vol. 28, no. 21, pp. 7703–7714, Nov. 2016.

[61] N. J. Carter, R. Mainz, B. C. Walker, C. J. Hages, J. Just, M. Klaus, S. S. Schmidt, A. Weber, W.-C. D. Yang, O. Zander, E. A. Stach, T. Unold, and R. Agrawal, "The Role of Interparticle Heterogeneities in the Selenization Pathway of Cu-Zn-Sn-S nanoparticle Thin Films: a Real-Time Study," *Journal of Materials Chemistry C*, vol. 3, no. 27, pp. 7128–7134, Jul. 2015.

[62] B. A. Williams, M. A. Smeaton, N. D. Trejo, L. F. Francis, and E. S. Aydil, "Effect of Nanocrystal Size and Carbon on Grain Growth during Annealing of Copper Zinc Tin Sulfide Nanocrystal Coatings," *Chem. Mater.*, vol. 29, no. 4, pp. 1676–1683, Feb. 2017.

[63] T. R. Martin, J. K. Katahara, C. N. Bucherl, B. W. Krueger, H. W. Hillhouse, and C. K. Luscombe, "Nanoparticle Ligands and Pyrolized Graphitic Carbon in CZTSSe Photovoltaic Devices," *Chem. Mater.*, vol. 28, no. 1, pp. 135–145, Jan. 2016.

[64] B. D. Chernomordik, P. M. Ketkar, A. K. Hunter, A. E. Béland, D. D. Deng, and E. S. Aydil, "Microstructure Evolution During Selenization of Cu_2ZnSnS_4 Colloidal Nanocrystal Coatings," *Chem. Mater.*, vol. 28, no. 5, pp. 1266–1276, Mar. 2016.

[65] W. Gong, T. Tabata, K. Takei, M. Morihama, T. Maeda, and T. Wada, "Crystallographic and optical properties of $(Cu, Ag)_2ZnSnS_4$ and $(Cu, Ag)_2ZnSnSe_4$ solid solutions," *Phys. Status Solidi C*, vol. 12, pp. 700–703, Apr. 2015.

[66] M. Dimitrievska, F. Boero, A. P. Litvinchuk, S. Delsante, G. Borzone, A. Pérez-Rodríguez, and V. Izquierdo-Roca, "Structural Polymorphism in 'Kesterite' Cu_2ZnSnS_4: Raman Spectroscopy and First-Principles Calculations Analysis," *Inorg. Chem.*, vol. 56, no. 6, pp. 3467–3474, Mar. 2017.

[67] J. J. S. Scragg, L. Choubrac, A. Lafond, T. Ericson, and C. Platzer-Björkman, "A low-temperature order-disorder transition in Cu_2ZnSnS_4 thin films," *Appl. Phys. Lett.*, vol. 104, no. 4, pp. 041911–5, Jan. 2014.

[68] W. Li, X. Liu, H. Cui, S. Huang, and X. Hao, "The role of Ag in $(Ag,Cu)_2ZnSnS_4$ thin film for solar cell application," *Journal of Alloys and Compounds*, vol. 625, no. C, pp. 277–283, Mar. 2015.

[69] W.-C. Yang, C. K. Miskin, N. J. Carter, R. Agrawal, and E. A. Stach, "Compositional Inhomogeneity of Multinary Semiconductor Nanoparticles: A Case Study of Cu_2ZnSnS_4," *Chem. Mater.*, vol. 26, no. 24, pp. 6955–6962, Dec. 2014.

[70] T. Tanaka, T. Sueishi, K. Saito, Q. Guo, M. Nishio, K. M. Yu, and W. Walukiewicz, "Existence and removal of Cu_2Se second phase in coevaporated $Cu_2ZnSnSe_4$ thin films," vol. 111, no. 5, pp. 053522–5, Mar. 2012.

[71] A. Fairbrother, E. García-Hemme, V. Izquierdo-Roca, X. Fontané, F. A. Pulgarín-Agudelo, O. Vigil-Galán, A. Pérez-Rodríguez, and E. Saucedo, "Development of a Selective Chemical Etch To Improve the Conversion Efficiency of Zn-Rich Cu_2ZnSnS_4 Solar Cells," *J. Am. Chem. Soc.*, vol. 134, no. 19, pp. 8018–8021, Apr. 2012.

[72] A. Fairbrother, X. Fontané, V. Izquierdo-Roca, M. Espíndola-Rodríguez, S. López-Marino, M. Placidi, L. Calvo-Barrio, A. Pérez-Rodríguez, and E. Saucedo, "On the formation mechanisms of Zn-rich Cu2ZnSnS4 films prepared by sulfurization of metallic stacks," *Solar Energy Materials and Solar Cells*, vol. 112, no. C, pp. 97–105, May 2013.

[73] W. Shockley and H. J. Queisser, "Detailed Balance Limit of Efficiency of p-n Junction Solar Cells," vol. 32, no. 3, pp. 510–519, Mar. 1961.

[74] T. Sasamura, T. Osaki, T. Kameyama, T. Shibayama, A. Kudo, S. Kuwabata, and T. Torimoto, "Solution-phase Synthesis of Stannite-type Ag_2ZnSnS_4 Nanoparticles for Application to Photoelectrode Materials," *Chem. Lett.*, vol. 41, no. 9, pp. 1009–1011, Sep. 2012.

[75] I. Tsuji, Y. Shimodaira, H. Kato, H. Kobayashi, and A. Kudo, "Novel Stannite-type Complex Sulfide Photocatalysts A^I_2-Zn-A^{IV}-S_4(A^I= Cu and Ag; A^{IV}= Sn and Ge) for Hydrogen Evolution under Visible-Light Irradiation," *Chem. Mater.*, vol. 22, no. 4, pp. 1402–1409, Feb. 2010.

[76] K. Li, B. Chai, T. Peng, J. Mao, and L. Zan, "Synthesis of multicomponent sulfide Ag_2ZnSnS_4 as an efficient photocatalyst for H 2production under visible light irradiation," *RSC Adv.*, vol. 3, no. 1, pp. 253–258, 2013.

[77] K.-W. Cheng and S.-W. Hong, "Influences of Silver and Zinc Contents in the Stannite Ag_2ZnSnS_4 Photoelectrodes on Their Photoelectrochemical Performances in the Saltwater Solution," *ACS Appl. Mater. Interfaces*, vol. 10, no. 10, pp. 22130–22142, Jun. 2018.

[78] C. Ma, H. Guo, K. Zhang, Y. Li, N. Yuan, and J. Ding, "The preparation of Ag_2ZnSnS_4 homojunction solar cells," *Materials Letters*, vol. 207, pp. 209–212, Nov. 2017.

[79] C. Ma, H. Guo, K. Zhang, N. Yuan, and J. Ding, "Fabrication of p-type kesterite Ag_2ZnSnS_4 thin films with a high hole mobility," *Materials Letters*, vol. 186, pp. 390–393, Jan. 2017.

[80] T. Sasamura, T. Osaki, T. Kameyama, T. Shibayama, A. Kudo, S. Kuwabata, and T. Torimoto, "Solution-phase Synthesis of Stannite-type Ag_2ZnSnS_4 Nanoparticles for Application to Photoelectrode Materials," *Chem. Lett.*, vol. 41, no. 9, pp. 1009–1011, Sep. 2012.

[81] P.-C. Huang, H.-I. Wang, S. Brahma, S.-C. Wang, and J.-L. Huang, "Synthesis and characteristics of layered SnS_2 nanostructures via hot injection method," *Journal of Crystal Growth*, vol. 468, pp. 162–168, Jun. 2017.

[82] J. M. R. Tan, Y. H. Lee, S. Pedireddy, T. Baikie, X. Y. Ling, and L. H. Wong, "Understanding the Synthetic Pathway of a Single-Phase Quarternary Semiconductor Using Surface-Enhanced Raman Scattering: A Case of Wurtzite Cu_2ZnSnS_4 Nanoparticles," *J. Am. Chem. Soc.*, vol. 136, no. 18, pp. 6684–6692, Apr. 2014.

[83] J. van Embden, L. Bourgeois, E. Della Gaspera, L. Waddington, Y. Yin, N. V. Medhekar, J. J. Jasieniak, and A. S. R. Chesman, "The formation mechanism of Janus nanostructures in one-pot reactions: the case of Ag–Ag_8GeS_6," *Journal of Materials Chemistry A: Materials for energy and sustainability*, vol. 4, pp. 7060–7070, Apr. 2016.

[84] H.-C. Liao, M.-H. Jao, J.-J. Shyue, Y.-F. Chen, and W.-F. Su, "Facile synthesis of wurtzite copper–zinc–tin sulfide nanocrystals from plasmonic djurleite nuclei," *J. Mater. Chem. A*, vol. 1, no. 2, pp. 337–341, 2013.

[85] B. Hou, D. Benito-Alifonso, N. Kattan, D. Cherns, M. C. Galan, and D. J. Fermín, "Initial Stages in the Formation of $Cu_2ZnSn(S,Se)_4$ Nanoparticles," *Chem. Eur. J.*, vol. 19, no. 47, pp. 15847–15851, Oct. 2013.

[86] A. D. Collord and H. W. Hillhouse, "Composition Control and Formation Pathway of CZTS and CZTGS Nanocrystal Inks for Kesterite Solar Cells," *Chem. Mater.*, vol. 27, no. 5, pp. 1855–1862, Feb. 2015.

[87] L. EBOOKS, "CRC Handbook of Chemistry and Physics," pp. 1–2661, Apr. 2004.

[88] J. W. Thomson, K. Nagashima, P. M. Macdonald, and G. A. Ozin, "From Sulfur−Amine Solutions to Metal Sulfide Nanocrystals: Peering into the Oleylamine−Sulfur Black Box," *J. Am. Chem. Soc.*, vol. 133, no. 13, pp. 5036–5041, Apr. 2011.

[89] Z. Li, A. L. K. Lui, K. H. Lam, L. Xi, and Y. M. Lam, "Phase-Selective Synthesis of Cu_2ZnSnS_4 Nanocrystals using Different Sulfur Precursors," *Inorg. Chem.*, vol. 53, no. 20, pp. 10874–10880, Sep. 2014.

[90] Y. Zou, X. Su, and J. Jiang, "Phase-Controlled Synthesis of Cu_2ZnSnS_4 Nanocrystals: The Role of Reactivity between Zn and S," *J. Am. Chem. Soc.*, vol. 135, no. 49, pp. 18377–18384, Nov. 2013.

[91] R. B. Balow, C. K. Miskin, M. M. Abu-Omar, and R. Agrawal, "Synthesis and Characterization of $Cu_3(Sb_{1-x}As_x)S_4$ Semiconducting Nanocrystal Alloys with Tunable Properties for Optoelectronic Device Applications," *Chem. Mater.*, vol. 29, no. 2, pp. 573–578, Jan. 2017.

[92] B. G. Mendis, M. D. Shannon, M. C. Goodman, J. D. Major, R. Claridge, D. P. Halliday, and K. Durose, "Direct observation of Cu, Zn cation disorder in Cu_2ZnSnS_4 solar cell absorber material using aberration corrected scanning transmission electron microscopy," *Prog. Photovolt: Res. Appl.*, vol. 22, no. 1, pp. 24–34, Sep. 2012.

[93] D. Han, Y. Y. Sun, J. Bang, Y. Y. Zhang, H.-B. Sun, X.-B. Li, and S. B. Zhang, "Deep electron traps and origin of p-type conductivity in the earth-abundant solar-cell material Cu_2ZnSnS_4," *Phys. Rev. B*, vol. 87, no. 15, pp. 155206–155201, Apr. 2013.

[94] X. G. Gong, A. Walsh, S.-H. Wei, and S. Chen, "Intrinsic point defects and complexes in the quaternary kesterite semiconductor Cu_2ZnSnS_4," *Phys. Rev. B*, vol. 81, no. 24, pp. 245204–10, Jun. 2010.

[95] E. Chagarov, K. Sardashti, A. C. Kummel, Y. S. Lee, R. Haight, and T. S. Gershon, "$Ag_2ZnSn(S,Se)_4$: A highly promising absorber for thin film photovoltaics," *The Journal of Chemical Physics*, vol. 144, no. 10, pp. 104704–12, Mar. 2016.

[96] T. Gershon, K. Sardashti, O. Gunawan, R. Mankad, S. Singh, Y. S. Lee, J. A. Ott, A. Kummel, and R. Haight, "Photovoltaic Device with over 5% Efficiency Based on an n-Type $Ag_2ZnSnSe_4$ Absorber," *Adv. Energy Mater.*, vol. 6, no. 22, p. 1601182, Aug. 2016.

[97] T. Gershon, K. Sardashti, Y. S. Lee, O. Gunawan, S. Singh, D. Bishop, A. C. Kummel, and R. Haight, "Compositional effects in $Ag_2ZnSnSe_4$ thin films and photovoltaic devices," *Acta Materialia*, vol. 126, pp. 383–388, Mar. 2017.

[98] J. Just, D. Lützenkirchen-Hecht, R. Frahm, S. Schorr, and T. Unold, "Determination of secondary phases in kesterite Cu_2ZnSnS_4 thin films by x-ray absorption near edge structure analysis," *Appl. Phys. Lett.*, vol. 99, no. 26, pp. 262105–4, Dec. 2011.

[99] Z.-Y. Xiao, B. Yao, Y.-F. Li, Z.-H. Ding, Z.-M. Gao, H.-F. Zhao, L.-G. Zhang, Z.-Z. Zhang, Y.-R. Sui, and G. Wang, "Influencing Mechanism of the Selenization Temperature and Time on the Power Conversion Efficiency of $Cu_2ZnSn(S,Se)_4$-Based Solar Cells," *ACS Appl. Mater. Interfaces*, vol. 8, no. 27, pp. 17334–17342, Jul. 2016.

[100] J. A. Clark, A. R. Uhl, T. R. Martin, and H. W. Hillhouse, "Evolution of Morphology and Composition during Annealing and Selenization in Solution-Processed $Cu_2ZnSn(S,Se)_4$," *Chem. Mater.*, vol. 29, no. 21, pp. 9328–9339, Nov. 2017.

[101] Y. Jiang, B. Yao, J. Jia, Z. Ding, R. Deng, D. Liu, Y. Sui, H. Wang, and Y. Li, "Structural, electrical, and optical properties of $Ag_2ZnSnSe_4$ for photodetection application," *Journal of Applied Physics*, vol. 125, no. 2, pp. 025703–10, Jan. 2019.

[102] Y. Zhao, X. Han, B. Xu, W. Li, J. Li, J. Li, M. Wang, C. Dong, P. Ju, and J. Li, "Enhancing Open-Circuit Voltage of Solution-Processed $Cu_2ZnSn(S,Se)_4$ Solar Cells With Ag Substitution," *IEEE J. Photovoltaics*, vol. 7, no. 3, pp. 874–881, Mar. 2017.

[103] Y. Jiang, B. Yao, J. Jia, Z. Ding, R. Deng, D. Liu, Y. Sui, H. Wang, and Y. Li, "Structural, electrical, and optical properties of $Ag_2ZnSnSe_4$ for photodetection application," vol. 125, no. 2, pp. 025703–10, Jan. 2019.

[104] F. Q. Zeng, Y. Q. Lai, Z. L. Han, B. K. Ng, Z. A. Zhang, H. L. Zhang, L. X. Jiang, and F. Y. Liu, "Fabrication of earth-abundant $Cu_2ZnSn(S,Se)_4$ light absorbers by a sol–gel and selenization route for thin film solar cells," *RSC Adv.*, vol. 6, no. 8, pp. 6562–6570, 2016.

[105] C. J. Hages, "Development and characterization of nanoparticle-based kesterite solar cells," 2017.

[106] Q. Guo, G. M. Ford, R. Agrawal, and H. W. Hillhouse, "Ink formulation and low-temperature incorporation of sodium to yield 12% efficient $Cu(In,Ga)(S,Se)_2$ solar cells from sulfide nanocrystal inks," *Prog. Photovolt: Res. Appl.*, vol. 21, no. 1, pp. 64–71, May 2012.

[107] S. M. McLeod, C. J. Hages, N. J. Carter, and R. Agrawal, "Synthesis and characterization of 15% efficient CIGSSe solar cells from nanoparticle inks," *Prog. Photovolt: Res. Appl.*, vol. 23, no. 11, pp. 1550–1556, Jan. 2015.

[108] M. P. Suryawanshi, S. W. Shin, U. V. Ghorpade, K. V. Gurav, G. L. Agawane, C. W. Hong, J. H. Yun, P. S. Patil, J. H. Kim, and A. V. Moholkar, "A chemical approach for synthesis of photoelectrochemically active Cu_2ZnSnS_4 (CZTS) thin films," *Solar Energy*, vol. 110, pp. 221–230, Sep. 2014.

[109] M. P. Suryawanshi, U. V. Ghorpade, U. P. Suryawanshi, M. He, J. Kim, M. G. Gang, P. S. Patil, A. V. Moholkar, J. H. Yun, and J. H. Kim, "Aqueous-Solution-Processed $Cu_2ZnSn(S,Se)_4$ Thin-Film Solar Cells via an Improved Successive Ion-Layer-Adsorption–Reaction Sequence," *ACS Omega*, vol. 2, no. 12, pp. 9211–9220, Dec. 2017.

[110] Y. Shiga, N. Umezawa, N. Srinivasan, S. Koyasu, E. Sakai, and M. Miyauchi, "A metal sulfide photocatalyst composed of ubiquitous elements for solar hydrogen production," *Chem. Commun.*, vol. 52, no. 47, pp. 7470–7473, 2016.

[111] J. Britt and C. Ferekides, "Thin-film CdS/CdTe solar cell with 15.8% efficiency," *Appl. Phys. Lett.*, vol. 62, no. 22, pp. 2851–2852, May 1993.

[112] J. P. Enriquez and X. Mathew, "Influence of the thickness on structural, optical and electrical properties of chemical bath deposited CdS thin films," *Solar Energy Materials and Solar Cells*, vol. 76, pp. 313–322, Feb. 2003.

[113] C.-Y. Yeh, Z. W. Lu, S. Froyen, and A. Zunger, "Zincblend-wurtzite Polytypism in Semiconductors," *Phys. Rev. B*, vol. 46, pp. 10086–10097, Oct. 1992.

[114] B.-S. Moon, J.-H. Lee, and H. Jung, "Comparative studies of the properties of CdS films deposited on different substrates by R.F. sputtering," *Thin Solid Films*, vol. 511, pp. 299–303, Jul. 2006.

[115] D. Abou-Ras, G. Kostorz, A. Romeo, D. Rudmann, and A. N. Tiwari, "Structural and chemical investigations of CBD- and PVD-CdS buffer layers and interfaces in Cu(In,Ga)Se_2-based thin film solar cells," *Thin Solid Films*, vol. 480, pp. 118–123, Jun. 2005.

[116] J. Schaffner, E. Feldmeier, A. Swirschuk, H. J. Schimper, A. Klein, and W. Jaegermann, "Influence of substrate temperature, growth rate and TCO substrate on the properties of CSS deposited CdS thin films," *Thin Solid Films*, vol. 519, no. 21, pp. 7556–7559, Aug. 2011.

[117] J. M. Doma and J. Herrero, "Chemical Bath Deposition of CdS Thin Film: An Approach to the Chemical Mechanism through Study of the Film Microstructure," *J. Electrochem. Soc*, vol. 144, pp. 4081–4091, Dec. 2004.

[118] L. Stolt, J. Hedström, J. Kessler, M. Ruckh, K. O. Velthaus, and H. W. Schock, "ZnO/CdS/$CuInSe_2$ thin-film solar cells with improved performance," *Appl. Phys. Lett.*, vol. 62, no. 6, pp. 597–599, Feb. 1993.

[119] H. Metin and R. Esen, "Annealing studies on CBD grown CdS thin films," *Journal of Crystal Growth*, vol. 258, no. 1, pp. 141–148, Oct. 2003.

[120] Y. Xu and A. A. Schoonen, "The absolute energy positions of conduction and valence bands of selected semiconducting minerals," *American Mineralogist*, vol. 85, pp. 543–556, Mar. 2000.

[121] O. Madelung, "Semiconductors: Data Handbook," in *II-VI compounds*, 2011, pp. 1–72.

[122] B. S. Tosun, C. Pettit, S. A. Campbell, and E. S. Aydil, "Structure and Composition of $Zn_xCd_{1-x}S$ Films Synthesized through Chemical Bath Deposition," *ACS Appl. Mater. Interfaces*, vol. 4, no. 7, pp. 3676–3684, Jun. 2012.

[123] X. Zhao, M. Lu, M. J. Koeper, and R. Agrawal, "Solution-processed sulfur depleted Cu(In, Ga)Se_2 solar cells synthesized from a monoamine–dithiol solvent mixture," *Journal of Materials Chemistry A: Materials for energy and sustainability*, vol. 4, pp. 7390–7397, May 2016.

[124] C. L. McCarthy, D. H. Webber, E. C. Schueller, and R. L. Brutchey, "Solution-Phase Conversion of Bulk Metal Oxides to Metal Chalcogenides Using a Simple Thiol-Amine Solvent Mixture," *Angew. Chem.*, vol. 127, no. 29, pp. 8498–8501, Jun. 2015.

[125] H.-J. Liu, J. T. Hupp, and M. A. Ratner, "Electronic Structure and Spectroscopy of Cadmium Thiolate Clusters," *J. Phys. Chem.*, vol. 100, no. 30, pp. 12204–12213, Jan. 1996.

[126] J. P. Enríquez and X. Mathew, "Influence of the thickness on structural, optical and electrical properties of chemical bath deposited CdS thin films," *Solar Energy Materials and Solar Cells*, vol. 76, no. 3, pp. 313–322, Mar. 2003.

[127] M. Moradi, R. Teimouri, M. Zahedifar, and M. Saadat, "Optimization of $Cd_{1-y}Zn_yS$ buffer layer in $Cu(In,Ga)Se_2$ based thin film solar cells," *Optik - International Journal for Light and Electron Optics*, vol. 127, no. 8, pp. 4072–4075, Apr. 2016.

[128] A. A. K. Bakly, Ben F Spencer, and P. O'Brien, "The deposition of thin films of cadmium zinc sulfide $Cd_{1-x}Zn_xS$ at 250 °C from spin-coated xanthato complexes: a potential route to window layers for photovoltaic cells," *Journal of Materials Science*, vol. 53, no. 6, pp. 4360–4370, Dec. 2017.

[129] A. Reinders and P. Reinhard, "Porassium-induced surface modification of $Cu(In,Ga)Se_2$ thin films for high-efficiency solar cells," *Nat. Mater.*, vol. 12, no. 12, p. 720, Jan. 2017.

[130] A. Chirilă, P. Reinhard, F. Pianezzi, P. Bloesch, A. R. Uhl, C. Fella, L. Kranz, D. Keller, C. Gretener, H. Hagendorfer, D. Jaeger, R. Erni, S. Nishiwaki, S. Buecheler, and A. N. Tiwari, "Potassium-induced surface modification of $Cu(In,Ga)Se_2$ thin films for high-efficiency solar cells," *Nat. Mater.*, vol. 12, pp. 1107–1111, Nov. 2013.

VITA

Xianyi Hu was born in Yingcheng, Hubei province in China. Raised up by her grandparents until 3 years old in countryside, she moved to Xiaogan, Hubei to live with her parents. She graduated from Xiaogan High School in 2008 and chose University of Science and Technology of China (USTC, Hefei, Anhui Province) due to its strong scientific and engineering emphasis. She was actively involved in undergraduate research under the supervision of Prof. Qianwang Chen on functional nanomaterial synthesis and its application. She earned her Bachelor of Science degree in Materials Science and Engineering from USTC in 2012.

In September 2012, Xianyi was accepted as Master student by Northwestern University. After she got the Master's degree in Materials Engineering from Northwestern University, she worked as a research assistant in collaboration with Dr. Tim Fister and Dr. Paul Fenter (Argonne National Laboratory) on the lithiation-delithiation induced structural/ compositional change of the electrode material in thin-film-based Li-ion batteries with the guidance from Prof. Michael Bedzyk. She came to Purdue University in August 2014 to pursue her PhD's degree in the same displine. She was working on solution processing for kesterite materials as light absorber for thin film photovoltaics, co-advised by Prof. Carol Handwerker and Prof. Rakesh Agrawal.

PUBLICATIONS

[1] X. Hu, S. Pritchett-Montavon, C. A. Handwerker and R. Agrawal, "Solution route to Ag_2ZnSnS_4 semiconducting nanoparticles and their optoelectronic properties" Submitted

[2] X. Hu, S. Pritchett-Montavon, M. J. Koeper, C. A. Handwerker and R. Agrawal, "Investigation of selenization conditions for $Ag_2ZnSnSe_4$ thin films for photovoltaic application" In preparration

[3] R. Zhang, S. Cho, D. G. Lim, X. Hu, E. A. Stach, C. A. Handwerker, and R. Agrawal, "Metal–metal chalcogenide molecular precursors to binary, ternary, and quaternary metal chalcogenide thin films for electronic devices," *Chem. Commun.*, vol. 52, no. 28, pp. 5007–5010, Mar. 2016